# *DEVELOPMENT OF CREEP-RESISTANT Al-Si-Mg-Cu CAST ALLOYS STRENGTHENED WITH NANO-SIZED DISPERSOIDS FOR DIESEL ENGINE APPLICATIONS*

Raul Irving Arriaga Benitez

Department of Mining and Materials Engineering

McGill University, Montreal

February 2025

---

*A thesis submitted to McGill University in partial fulfilment*

*of the requirements of the degree of Doctor of Philosophy*

# ABSTRACT

Large amount of thermally stable dispersoids formed from the addition of peritectic elements to develop creep resistant Al-Si-Mg-Cu cast alloys intended for Diesel Engine applications (trucks, construction, military, agriculture, mining and railroad) have the potential to offer a variety of advantages over electric motors (performance, reliability, and durability) and gasoline engines (durability, performance, fuel efficiency and environmental benefits). These alloys, classified as third generation of aluminum diesel engine alloys, have demonstrated better creep properties (300 °C and 20-30 MPa stress range) than their precursors. However, their durability may be affected by creep deformation mechanisms (dislocation creep, diffusional creep and grain boundary sliding). This doctoral thesis has the purpose to study the creep activation energies and microstructural features observed in creep samples strengthened with nano-sized dispersoids via the use of Mn, Cr, Zr and Mo to provide a tool to identify the rate controlling creep mechanisms in the alloys.

The synergistic effects of nano-sized α-Al(Mn,Cr,Fe)Si and Al-Si-Zr dispersoids on the creep behavior were investigated in the first Al alloy system, Al-7Si-0.3Mg-0.5Cu-0.15Mn-0.25Cr-0.15Zr (MG2-1), and compared with the Al base alloy, Al-7Si-0.3Mg-0.5Cu (MG1). The modified alloy shown an increase in the apparent activation energy for creep (234 kJ $mol^{-1}$) regarding unmodified alloy (184 kJ $mol^{-1}$) indicating a significant improvement in the creep resistance. Electron microscopy studies revelaed that the creep deformation mechanisms are related with recovery and Zener pinning of boundary migration in the MG2-1 alloy and local climb over dispersoids in the MG1 alloy. Thermodynamic calculations helped to identify the phases present validating their presence by SEM/TEM microstructural observations. Additionally, EDS analysis

shown that the Q'-Al-Mg-Cu-Si precipitates has the main role to act as nucleating site for the formation of α-dispersoids.

A review about the trend in the use of heavy-duty diesel engine vehicles in the automotive market was studied. It was mentioned that the development of diesel engine aluminum alloys is an effective way to contribute to the fuel efficiency, performance and reduction in the $CO_2$ emissions. However, the necessity to produce aluminum alloys that resist creep deformation at ~300 °C should be investigated. The review of studies in the field indicated that dispersion strengthening with thermally stable second phases uniformly distributed in large volume fractions is the most promising way to control creep deformation in aluminum alloys. Alternative ways such as additive manufacturing, Al matrix composites, thermal barrier coatings and nanostructured Al alloys are also seen as useful methods to contribute to the creep resistance, although their processes and thermal stability should be improved and optimized.

The influence of dispersoids and solutes on the recovery processes of creep deformation in an Al-Si-Mg-Cu (Mo, Mn) diesel engine alloy were investigated in the third, Al-7Si-0.3Mg-0.5Cu-0.3Mo-0.15Mn (MG3-1), and fourth, Al-7Si-0.3Mg-0.5Cu-0.3Mo-0.5Mo (MG4-1), Al alloy systems. It was demonstrated that the size, coherency and stability of α-Al(Fe,Mn,Mo)Si dispersoids were related to the Mn level in the alloys leading to the improvement of creep properties at elevated temperatures. The creep mechanisms were determined via microstructural analysis (SEM, TEM, HRTEM and EBSD) and FactSage calculations of phase selection. The analyses indicated that the rate-governing creep mechanism is attributed to dynamic recovery in both alloys systems. However, an increase in the Mn addition limited silicon diffusion due to the stability of α-Al(Fe,Mn,Mo)Si dispersoids and to the formation of coherent non-shearable nano dispersoids pinning and limiting subgrain migration. As a result, the dynamic recovery was

reduced and a low creep rate was obtained. The activation energies for creep were calculated to be 203 kJ $mol^{-1}$ (MG3-1) and 249 kJ $mol^{-1}$ (MG4-1) indicating an improved creep resistance due to increased Mn addition.

# RÉSUMÉ

Une grande quantité de dispersoïdes thermiquement stables formés par l'ajout d'éléments péritectiques pour développer des alliages moulés Al-Si-Mg-Cu résistants au fluage, destinés aux applications de moteurs Diesel (camions, construction, militaire, agriculture, exploitation minière et chemin de fer), offre un large éventail d'avantages par rapport aux moteurs électriques (performance, fiabilité et durabilité) et aux moteurs à essence (durabilité, performance, efficacité énergétique et avantages environnementaux). Ces alliages, classés comme la troisième génération d'alliages en aluminium pour moteurs Diesel, ont démontré de meilleures propriétés de fluage (300 °C et une plage de contrainte de 20-30 MPa) par rapport à leurs prédécesseurs. Cependant, leur durabilité peut être affectée par les mécanismes de déformation par fluage (fluage par dislocation, fluage diffusif et glissement des joints de grains). Cette thèse de doctorat a pour objectif d'étudier les énergies d'activation du fluage et les caractéristiques microstructurales observées dans des échantillons de fluage renforcés par des dispersoïdes de taille nanométrique grâce à l'utilisation de Mn, Cr, Zr et Mo, afin de fournir un outil permettant d'identifier les mécanismes de fluage limitant la vitesse dans ces alliages.

Les effets synergiques des dispersoïdes nanométriques α-Al(Mn,Cr,Fe)Si et Al-Si-Zr sur le comportement au fluage ont été étudiés dans le premier système d'alliage d'aluminium, Al-7Si-0.3Mg-0.5Cu-0.15Mn-0.25Cr-0.15Zr (MG2-1), et comparés à l'alliage de base Al, Al-7Si-0.3Mg-0.5Cu (MG1). L'alliage modifié a montré une augmentation de l'énergie d'activation apparente pour le fluage (234 kJ $mol^{-1}$) par rapport à l'alliage non modifié (184 kJ $mol^{-1}$), indiquant une amélioration significative de la résistance au fluage. Les études de microscopie électronique ont révélé que les mécanismes de déformation par fluage sont liés à la récupération et au blocage de

la migration des joints de grains par l'effet Zener dans l'alliage MG2-1, tandis que dans l'alliage MG1, ils sont associés au déplacement local autour des dispersoïdes. Les calculs thermodynamiques ont permis d'identifier les phases présentes, validées par des observations microstructurales en microscopie électronique à balayage (MEB) et en microscopie électronique en transmission (MET). De plus, l'analyse de spectroscopie de rayons X à dispersion d'énergie (EDS) a montré que les précipités Q'-Al-Mg-Cu-Si jouent un rôle clé en tant que site de nucléation pour la formation des dispersoïdes α.

Une reveu sur la tendance de l'utilisation des véhicules lourds à moteur diesel sur le marché automobile a été réalisée. Il a été mentionné que le développement d'alliages d'aluminium pour moteurs diesel est un moyen efficace de contribuer à l'efficacité énergétique, aux performances et à la réduction des émissions de $CO_2$. Cependant, la nécessité de produire des alliages d'aluminium capables de résister à la déformation par fluage à environ 300 °C doit être étudiée. L'examen des études dans ce domaine a indiqué que le renforcement par dispersion avec des phases secondaires thermiquement stables, uniformément réparties en grandes fractions volumiques, est la méthode la plus prometteuse pour contrôler la déformation par fluage dans les alliages d'aluminium. Des méthodes alternatives telles que la fabrication additive, les composites à matrice d'aluminium, les revêtements de barrière thermique et les alliages d'aluminium nanostructurés sont également considérées comme des approches utiles pour améliorer la résistance au fluage, bien que leurs procédés et leur stabilité thermique nécessitent encore des améliorations et une optimisation.

L'influence des dispersoïdes et des solutés sur les processus de récupération lors de la déformation par fluage dans un alliage pour moteur diesel Al-Si-Mg-Cu (Mo, Mn) a été étudiée dans les systèmes d'alliages d'aluminium de troisième génération, Al-7Si-0.3Mg-0.5Cu-0.3Mo-0.15Mn (MG3-1), et de quatrième génération, Al-7Si-0.3Mg-0.5Cu-0.3Mo-0.5Mo (MG4-1). Il a été

démontré que la taille, la cohérence et la stabilité des dispersoïdes α-Al(Fe,Mn,Mo)Si étaient liées au niveau de Mn dans les alliages, conduisant à l'amélioration des propriétés de fluage à des températures élevées. Les mécanismes de fluage ont été déterminés grâce à l'analyse microstructurale (MEB, MET, MET à haute résolution et Diffraction d'électrons Rétrodiffusés) et aux calculs de sélection de phases via FactSage. Les analyses ont indiqué que le mécanisme de fluage contrôlant la vitesse est attribué à la récupération dynamique dans les deux systèmes d'alliages. Cependant, une augmentation de l'ajout de Mn a limité la diffusion du silicium en raison de la stabilité des dispersoïdes α-Al(Fe,Mn,Mo)Si et de la formation de dispersoïdes nanométriques cohérents et non cisaillables, qui bloquent et limitent la migration des sous-grains. Par conséquent, la récupération dynamique a été réduite et un faible taux de fluage a été obtenu. Les énergies d'activation pour le fluage ont été calculées à 203 kJ $mol^{-1}$ pour l'alliage MG3-1 et à 249 kJ $mol^{-1}$ pour l'alliage MG4-1, indiquant une amélioration de la résistance au fluage due à l'augmentation de l'ajout de Mn.

# ACKNOWLEDGEMENTS

I am extremely grateful with everyone who help me to experience one of the best time in my life called Ph.D. I cannot begin to express my thanks to my supervisor, Professor Mihriban Pekguleryuz, for her expertise, leadership and moral values, both inside and outside of the working life. It is because of her that I was able to understand the term “Passion for Science”. Her guidance help me become a better person not only professionally but also personally.

I would like to extend my sincere thanks to all members of Light Metals Research Group, Mara Martínez, Yizhi Wang, Orhan Sari, MSc. Parham Valipoorsalimi, Dr. Konstantinos Korgiopoulos, Dr. Luis Villegas, and Pierre Vermette for their invaluable theoretical and practical contributions to this doctoral research. Special thanks to David Liu, Lise Guichaoua, Stéphanie Bessette, Alexandra Djuric and Sam Minter for their technical assistance.

I gratefully acknowledge Natural Sciences and Engineering Research Council of Canada (NSERC), Gerald Hatch Fellowship, Fonds Québécois de la Recherche sur la Nature et les Technologies – Programme de Bourses d'Excellence pour Étudiants Étrangers (FRQNT – PBEEE) and Consejo Nacional de Humanidades, Ciencias y Tecnologias–Secretaria de Energia (CONAHCyT–SENER) for their financial support to my doctoral research.

I would like to express my deepest gratitude to my lovely life partner, Lupita, my inspiring and supportive mother, Lucia, my intelligent brother, Juan, my caring aunt, Elvis, and all my big Mexican family for being a fundamental part in this goal. Finally, I will close this section by sharing a positive thinking that I learned during my Ph.D.: “Proceed as if Success is Inevitable”.

# TABLE OF CONTENTS

# LIST OF FIGURES

# LIST OF TABLES

# CONTRIBUTION OF AUTHORS

This thesis was written by Raul Irving Arriaga Benitez and reviewed by Prof. Mihriban Pekguleryuz. All the results presented in this thesis (chapter 3-5) have been published in scientific journals.

Chapter 3: Raul Irving Arriaga-Benitez, Mihriban Pekguleryuz, The synergistic effects of nano-sized α-Al(Mn, Cr, Fe)Si and Al–Si–Zr dispersoids on the creep behavior Al–Si–Mg–Cu (Mn, Cr, Zr) diesel engine alloy, Mater. Sci. Eng. A. 872 (2023), 144949. https://doi.org/10.1016/j.msea.2023.144949.

Chapter 4: Raul Irving Arriaga-Benitez, Mihriban Pekguleryuz, Recent progress in creep-resistant aluminum alloys for diesel engine applications: a review, Materials 2024, 17(13), 3076. https://doi.org/10.3390/ma17133076.

Chapter 5: Raul Irving Arriaga-Benitez, Mihriban Pekguleryuz, The influence of dispersoids and solutes on the recovery processes of creep deformation in an Al-Si-Mg-Cu (Mo, Mn) diesel engine alloy, J. Mater. Sci. 60, 2554–2579 (2025). https://doi.org/10.1007/s10853-024-10566-y.

# CHAPTER 1: INTRODUCTION

This chapter presents the motivations, interests and objectives that conducted to this study. Additionally, a thesis outline is given to help the readers to understand the content of this fascinating research project.

## 1.1 Background

The growing $CO_2$ emissions from transportation sector currently contribute 14% of global greenhouse gas (GHG) emissions making it the second-largest source of emissions worldwide wherein cars and vans are the biggest source of transportation emissions with a 48%, followed by heavy freight vehicles with a 16% [1]. The transport industry has identified that vehicle weight reduction by Al alloys is a key solution, resulting in vehicle mass savings. As such, this could represent a 51% reduction in the fuel economy, 44% increase in the vehicle performance and 50% reduction in the $CO_2$ emissions (see Table 2.1). Therefore, diesel engine studies involving the use of Al alloys started in 1996 with VAW (Germany), and Alcan-Pechiney (Canada, France), and continued in 2008 with McGill University in order to improve the durability, efficiency and performance of the Al alloys under the diesel engine working conditions [2–5]. The mechanism proposed indicated that a proper Al alloy should have a good combination of strength, ductility and creep resistance up to 300 °C, good castability and good choice of alloying elements to maintain cost effectiveness, availability and recyclability.

Recently, dispersion strengthening has gained more attention for its potential benefits in diesel engine components due to the strengthening effect of the dispersoids. However, the extent of dispersoids' effectiveness relied on the amount, size, morphology, interparticle spacing, coherency and thermal stability in the Al matrix [6–8]. As a result, the use of peritectic elements as a route to form equilibrium phases has led to the development of new generations of Al alloys resistant to the creep deformation [9]. These findings have inspired the investigation of the fundamental understanding of the creep deformation mechanisms in Al alloys intended for diesel engine applications.

## 1.2 The Objective

The objective of this study is to unravel such creep micro-mechanisms from the experimental determination of the apparent activation energy and associating and describing it with a method of theoretically calculating the activation energies of creep mechanism based on electron microscopy analyses. The method was applied to Al-7Si-0.3Mg-0.5Cu (MG1), Al-7Si-0.3Mg-0.5Cu-0.15Mn-0.25Cr-0.15Zr (MG2-1), Al-7Si-0.3Mg-0.5Cu-0.3Mo-0.15Mn (MG3-1) and Al-7Si-0.3Mg-0.5Cu-0.13Mo-0.5Mn (MG4-1) alloys. The alloys were cast, machined, heat treated to T7 condition, pre-soaked 100 hr at 300 °C and thermodynamically simulated in the non-equilibrium and equilibrium conditions and then tested under dislocation creep ranges of temperature and stress that are experienced in the Diesel engine operation.

## 1.3 Thesis Outline

This thesis is divided into five main parts. Chapter 2 gives an overview on the benefits in the use diesel engine, the fracture modes of aluminum alloys and defines the creep micro-mechanisms

involved at the diesel engine operating conditions. In addition, an explanation describing each strengthening mechanism as current strategy to combat these creep deformation mechanisms is given.

Chapter 3 presents a systematic study on two Al alloys (Al-7Si-0.3Mg-0.5Cu (MG1) and Al-7Si-0.3Mg-0.5Cu-0.15Mn-0.25Cr-0.15Zr (MG2-1)) with the purpose of understanding the effect of combined additions of Cr, Zr and Mn on the microstructure and creep properties. Electron microscopy analyses are reported and the influence of creep micro-mechanisms affecting the creep behavior are investigated and discussed.

Chapter 4 reviews the recent progress in creep-resistant aluminum alloys intended for diesel engine applications. The importance in the use of Al alloys in heavy-duty vehicles is highlighted. A description of the different generations of Al alloys is summarized, and new approaches to improve creep resistance is discussed.

Chapter 5 discusses the influence of Mn and Mo on the recovery processes of creep deformation in Al-7Si-0.3Mg-0.5Cu-0.3Mo-0.15Mn (MG3-1) and Al-7Si-0.3Mg-0.5Cu-0.13Mo-0.5Mn (MG4-1) alloys. Microstructural analyses involving SEM, TEM, HRTEM and EBSD techniques are described and the rate-governing creep mechanisms are discussed.

Chapter 6 discusses the overall conclusions and the contributions to original knowledge.

# CHAPTER 2. LITERATURE REVIEW

This chapter is divided into six sections. The first section describes the operating mode of the diesel engine and the benefits to use Al alloys in diesel engine components. The second part shows the facture modes during the diesel engine operation. The third part defines the concept of creep and the creep deformation mechanisms in aluminum alloys. The fourth section discusses the strengthening mechanisms such as alloying, heat treatment, particle features (particle size, volume fraction, homogeneous distribution, shape of particles) and interfacial bonding used in dispersion strengthening to improve creep in Al alloys. The fifth section notes that there are recent studies that were published during the course of this PhD which are separately reviewed in Chapter 4 of this thesis. The sixth section summarizes the strategy, and the methodology adopted in this PhD study.

## 2.1 Diesel Engine Operation

Compression ignition engine or diesel engine was invented by the engineer Rudolf Diesel with a patent application on February 27, 1892. Technically, diesel engine operates through of the burning of a fuel-air mixture within the cylinders where the heat of compression is used to initiate the ignition and burn the fuel [10]. During this process, the combustion takes place at variable pressure in a real diesel cycle. Differences such as higher compression ratios, use lean mixtures and its lack of need for throttling the intake charge allow the diesel engine to be more efficient than gasoline engines.

Diesel engines fall into two categories, two-stroke or four-stroke cycle engines. The four-stroke cycle engine is frequently used in motor vehicle systems in which the piston completes a travel along the cylinder in four different events, intake, compression, power, and exhaust, to convert the chemical energy of the fuel into useful mechanical energy (Fig. 2.1). In the intake stroke, the piston moves down when the intake valve opens up letting in air. In the compression stroke, the piston moves back up and compresses the air. In the power stroke, as the piston reaches the top, fuel is injected at just the right moment and ignited, forcing the piston back down. In the exhaust stroke, the piston moves back to the top, pushing out the exhaust created from the combustion out of the exhaust valve.

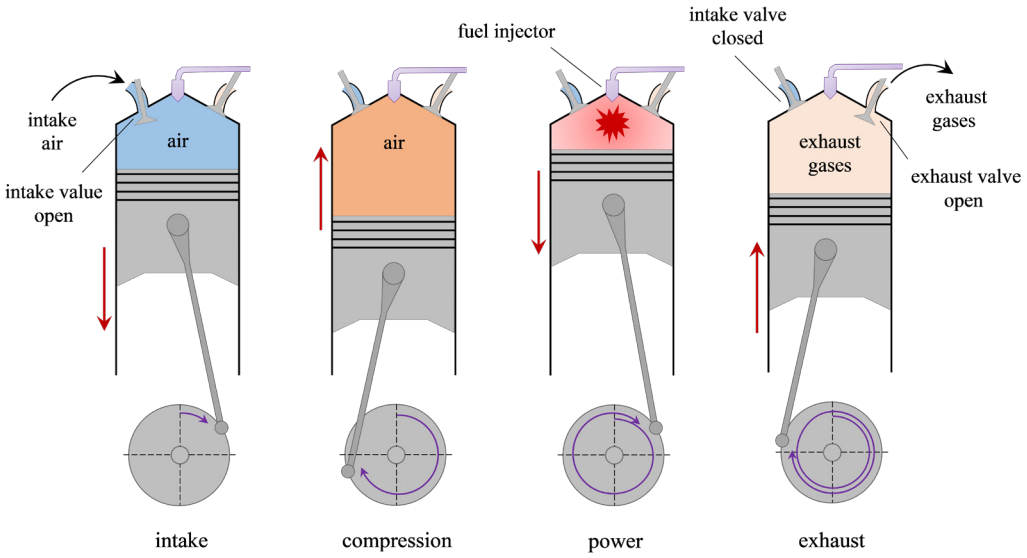


*Figure 2.1. Stages of the four-stroke cycle engines.*

### 2.1.1 Fuel Economy, Performance and Greenhouse Gas Emissions

During the last two decades, U.S, Europe and other countries and regions have introduced regulations to reduce the vehicle mass as a strategy to contribute to fuel economy, performance and greenhouse gas emissions [11]. Nowadays, diesel engine strategies aim towards the

development of heavy-duty vehicles due to their limitations in the battery technology and charging infrastructure [12]. In response to these challenges, the use of aluminum alloys in cylinder heads and engine blocks may represent a weight reduction about 40% – 55% [13]. The comparison of fuel economy, performance and greenhouse gas emissions among diesel engines fabricated by the same automotive company are shown in Table 2.1. The data show that diesel engines using all-Al alloys components exhibit better results than those with Al alloys and cast iron combined and all-cast iron components [14–16].

*Table 2.1. Comparison of fuel economy, performance and greenhouse gas emissions among the different versions of diesel engines fabricated by the same company using all-Al alloys, Al alloy and cast iron combined, and all-cast iron components.*

| Type of Diesel Engine |  Opel Zafira Tourer 1.6 CDTI |  Opel Astra 1.7-liter CDTI |  Opel Rekord D diesel version with 2.1 L |
|---|---|---|---|
| Year | 2013 − 2019 | 2007 − 2009 | 1972 − 1977 |
| Curb Weight | 1653 Kg | 1265 Kg | 1230 Kg |
| Diesel Engine Component | Cylinder head: Aluminum Alloy<br>Engine Block: Aluminum Alloy | Cylinder head: Aluminum alloy<br>Engine Block: Cast Iron | Cylinder head: Cast iron<br>Engine Block: Cast Iron |
| Fuel Economy | 4.1 L/100 km | 5.2 L/100 km | 8.0 L/100 km |
| Performance | 100 kW/l | 81 kW/l | 44 kW/l |
| $CO_2$ Emissions | 109 g/km | 140 g/km | 214 g/km |

The aluminum cylinder head market industry by application and region is shown in figure 2.2.a, b, respectively. Figure 2.2.a reveals that the tendency in the market for aluminum cylinder heads

in both passenger and commercial vehicles will remain stable in the next eight years due to their crucial role to enhance fuel efficiency, performance, reduced emissions and provide better heat dissipation. On the other hand, the regional analysis in the aluminum cylinder head market indicates that North America (United States, Canada and Mexico) will be the region with more production and consumption of aluminum cylinder heads owing to factors such as, the availability of raw materials, regulatory environments, and others [17].

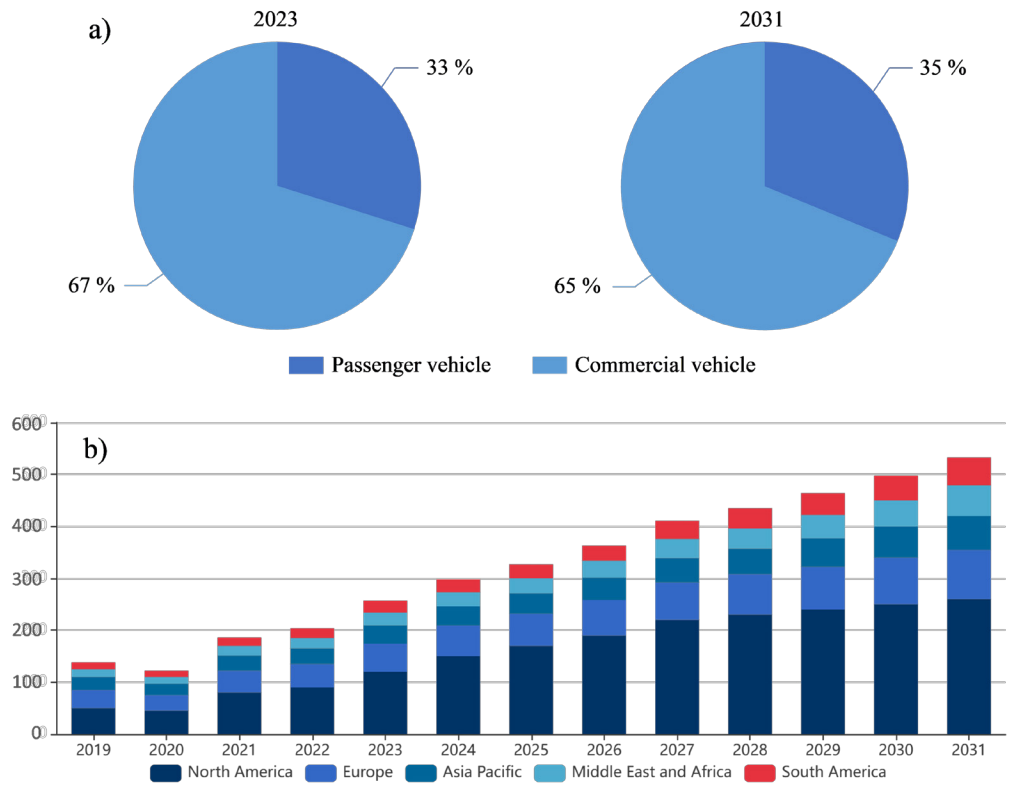


*Figure 2.2. Present and projection* percentage analysis *on aluminum cylinder head market share by a) application and b) region.*

Aluminum engine block market, on the other side, is expected to reach USD 3.5 billion by 2030, growing at an 8.0% CAGR (compound annual growth rate) from 2023 to 2030. This due to the performance generated in terms of noise and vibration dampening, leading to o a smoother and

quieter driving experience. In addition, the reduced weight in aluminum engine block also contributes to better handling and maneuverability with an excellent thermal conductivity to help prevent overheating. In terms of region, North America, Europe and Asia are expected to dominate the aluminum engine block market due to a high rate of vehicle production, favorable government policies and the presence of major automotive manufacturers in the region [18].

## 2.2 Fracture Modes in Diesel Engine Al Alloys

The cylinder head and engine block durability throughout the diesel engine operation depends on two main failure modes identified as mechanical fatigue or high cycle fatigue (HCF) and thermal fatigue or low cycle fatigue (LCF). However, thermal fatigue is the most severe of them due to temperature gradients and thermal stresses in the relatively slow varying thermal cycles resulting in a decreased material strength at elevated temperatures [19]. Both cylinder head and engine block experience process of thermal expansion under compressive stresses at high temperatures and process of contraction at low-load conditions when the temperature decreases. This results in large temperature variations that combined with the effects of creep cause local tensile stresses, which surpass the yield strength of the material producing plastic deformation [5].

In cylinder head, creep is developed at the inter-valve bridge area between the intake and exhaust valves. Expansion process originated through the combustion and contraction process identified through cylinder head stiffness due to water-cooled result in compressive thermal loads. Finally, thermal gradients along with cylinder pressure that changes throughout each engine operation cycle lead to tensile loads causing the greatest contribution of fatigue at this critical region [20].

In engine block, creep is originated at the top of the engine liner between adjacent bores. This zone is in direct contact with the combustion gases reaching to temperatures near 300 °C while the interior remains at the ambient temperature because of water-cooling (sometimes as low as −30°C) causing a restriction of thermal expansion and generating local compressive stress (creep deformation). The repetition of expansion and contraction cycles identified during engine heat-up and cold-down result in local tensile stresses causing fatigue cracks that can be nucleated during the engine cool-down period if the initial creep deformation is high, and the material does not have sufficient ductility to accommodate these stresses by local plastic deformations. Even when the material is ductile, the repetition of these alternating compressive and tensile stresses can cause crack initiation due to plastic damage accumulation and eventually lead to failure in diesel engines.

## 2.3 Creep in Aluminum Alloys

Creep can be defined as the plastic deformation that occurs below the yield strength of the material at elevated temperatures over time, and depends of applied stress, temperature and time. This phenomenon is due to thermally activated processes that occur in metals at elevated temperatures ($T > 0.4\ Tm$) such as diffusion and vacancy creation [21].

Figure 2.4 shows the different steps to obtain the creep resistance of an aluminum alloy. First, Creep resistance of the material is conducted by a creep test (Fig. 2.4.a). This test is performed under constant load and constant temperature in a creep testing machine over time. As a result, a creep curve of strain vs time is generated (Fig. 2.4.b). Beyond the elastic strain, three stages are distinguished in creep. Stage I, also called primary or transient creep, the plastic deformation causes strain hardening, which dominates over recovery. The density of dislocations increases, and dislocation glide is hindered. Stage II, also called secondary or steady state creep, will be reached

when the strain hardening is balanced by the recovery softening, resulting in a constant strain rate. Finally, in stage III, also called tertiary creep, strain rate increases with time due to the formation of internal voiding and cracking at grain boundaries [21].

Steady state creep rate is the most important design parameter for selecting suitable materials to be used in definite applications. $\dot{\varepsilon}_{ss} = A\sigma^{n_a} exp\left(-\frac{Q_a}{RT}\right)$ [eq. 1], where $A$ is the pre-exponential factor, $T$ is the absolute temperature in Kelvin, $n_a$ is the apparent stress exponent, $Q_a$ is the apparent creep activation energy and $R$ is the gas constant [22]. In automotive engine applications, minimum creep rate < 0.004 $s^{-1}$ is usually acceptable. Steady state creep rate can be described by the Arrhenius equation by the pre-exponential factor, the absolute temperature in Kelvin, the apparent stress exponent, apparent creep activation energy and the gas constant. Creep mechanism can be identified by determining the activation energy for creep from Arrhenius relationship of strain rate and reciprocal temperature (Fig. 2.4.c). We can graphically determine the apparent activation energy by manipulating the Arrhenius equation to put it into the form of a straight line. The apparent activation energy is obtained by plotting natural logarithm of steady state creep rate ($\dot{\varepsilon}_s$) versus $1/T$, where the slope is $(-Q_c/R)$ [22].

Calculated activation energy can be obtained experimentally from electron microscopy analyses. Here, the microstructural features along with the equations of creep deformation mechanisms (described on section 2.4.1) are used to determine the value of the activation energy. Subsequently, the calculated activation energy can be associated with the apparent activation energy (Fig.2.4.c) as a direct method to determine the true activation energy as well as identifying the rate controlling creep mechanism (Fig. 2.4.d) [8,23].

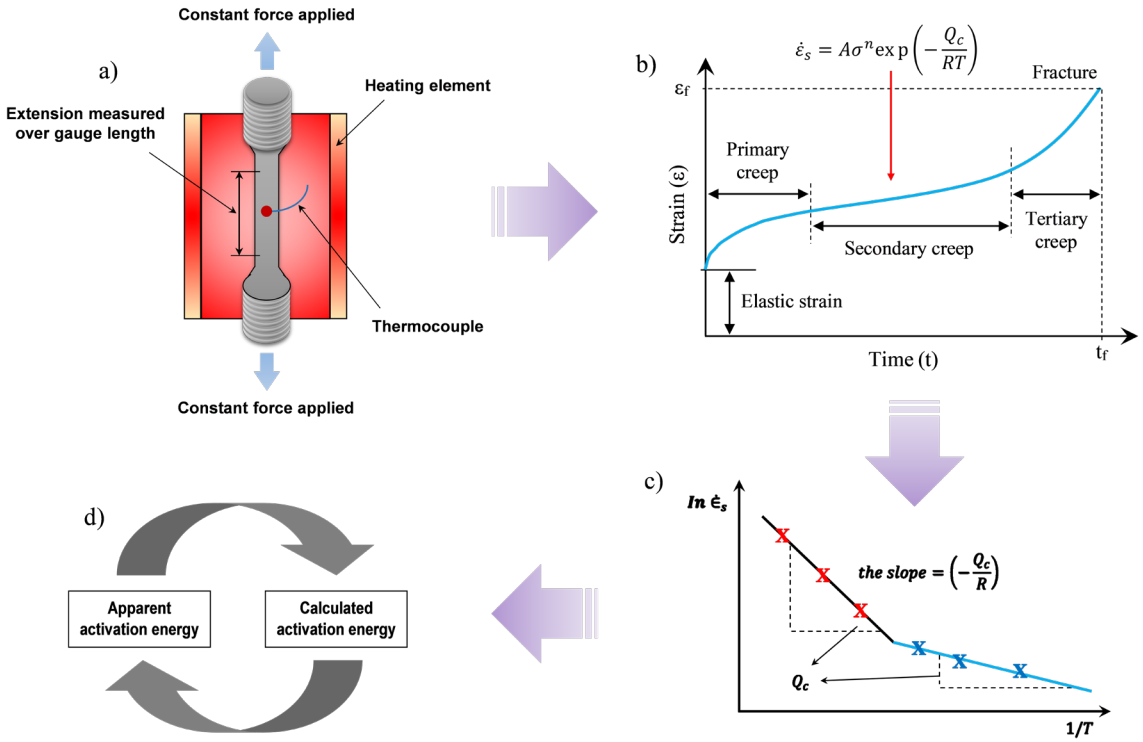


*Figure 2.3. Steps to determine the creep resistance in aluminum alloys: a) perform the tensile creep test; b) obtain the creep curve; c) determine the apparent activation energy; d) associate the apparent activation energy with calculated activation energy based on electron microscopy analyses.*

### 2.3.1 Creep Deformation Mechanisms

Creep can be classified as dislocation creep, diffusional creep and grain boundary sliding. However, at the diesel engine service conditions on powertrain components such as cylinder heads and engines blocks dislocation creep conditions or grain boundary migration/sliding are usually present. These mechanisms involve the interactions of dislocations with vacancies causing the movement of dislocations segments locally and can be identified by determining the activation energy for creep from Arrhenius relationship of strain rate and reciprocal temperature, as shown in Fig. 2.4.c. Depending on the mechanism the activation energy for dislocation creep can vary.

The description and activation energies for creep mechanisms are summarized below [23–25].

*Dislocation intersection:* Dislocations interaction involves interactions between two dislocations (Fig. 2.5). When the dislocations interact, a break or jog is formed on the dislocation line. The activation energy $q$ for this mechanism is composed of the activation energy for jog creation and the work done by stress $\tau$ to push the dislocation segment to the stress field of the other dislocation. It can be represented by $q = q_o - \tau b^2 l$ where $q_o = \alpha \mu b^3$, $q \sim q_{SD}$, where $b$ is the burgers vector, $l$ is length of dislocation that moves during intersection (spacing between dislocations), $\alpha$ is shear modulus and $q_{SD}$ is the activation energy for self-diffusion [24,26].

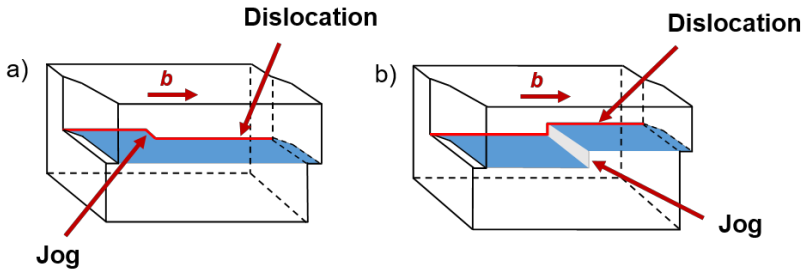


*Figure 2.4. Schematic of dislocation intersection: a) edge dislocation; b) screw dislocation.*

*Movement of dislocations with jogs:* Movement of dislocations with jogs involves screw dislocations containing a jog (Fig. 2.6). Here, the screw dislocation is trying to move. However, since the jogs are short segments of edge dislocations, the dislocation thus would be immobile. If a vacancy is emitted, the jog moves one plane up and it climbs to keep up with the rest of the dislocation producing creep strain. The activation energy, $q_d$, for this process is equal to the energy for vacancy formation, $q_f$, and the energy to move the vacancy away, $q_m$. The sum of these values is the activation energy for self-diffusion, $q_{SD}$. The activation energy can be represented by $q_d = q_f + q_m = q_{SD}$ [24].

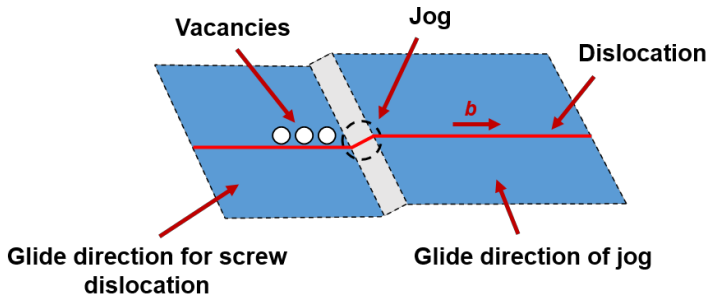


*Figure 2.5. Schematic of movement of dislocations with jogs.*

*Dislocation Climb:* Dislocation climb involves the vacancy–atom exchange mechanism (Fig. 2.7). Here, if a vacancy diffuses to the dislocation line in the crystal, an atom at the half-plane can be replaced by the vacancy (Fig. 2.7.b). As a result, the half plane at this location has moved upwards. This process causes the edge dislocation to move upwards (Fig. 2.7.c). Similarly, the edge of the dislocation, i.e. the end of the half-plane, can emit a vacancy. Consequently, the half-plane to move downwards. The activation energy, $q$, can be represented by $q = q_d + q_j = q_{SD}$, where $q_d$ is activation energy for movement of dislocation atmosphere and $q_j$ is the thermal energy to move the jogs [24].

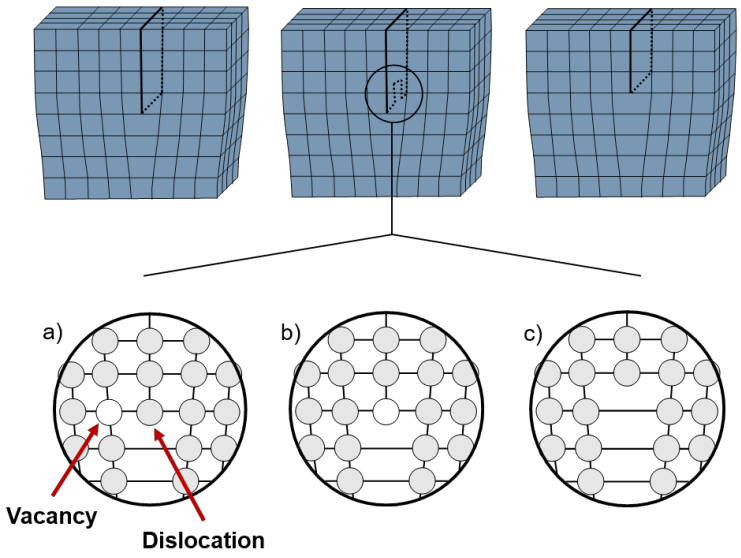

*Figure 2.6. Schematic of dislocation climb: a) vacancy and dislocation; b) vacancy diffuses to the dislocation line; c) edge dislocation has moved upwards.*

*Movement of Dislocation Atmospheres:* Movement of dislocation atmospheres involves solute atmospheres forming around dislocations to act as obstacles to dislocation motion (Fig. 2.8). However, the interaction with vacancies cause dislocation segments to escape their solute atmosphere and drag stress disappears for dislocation segments locally. As a result, dislocation segments move at strengths below the overall yield strength. The rate is proportional to the diffusion rate of the solute atoms wherein the activation energy is represented by $q_s =$ activation energy for solute diffusion [24].

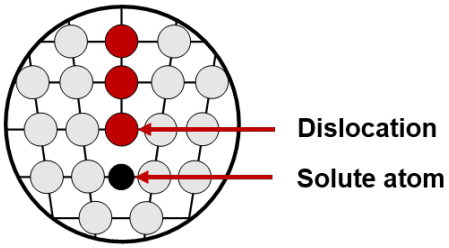


*Figure 2.7. Schematic of movement of dislocation atmospheres.*

*Activated Cross-Slip:* Activated cross-slip involves the interchange of slip planes of screw dislocations (Fig. 2.9). In order for cross-slip to occur, a screw dislocation needs to dissociate into a pair of partial dislocations with a connecting layer of stacking fault. The sequence of events during cross slip occurs in an extended screw dislocation in the primary slip plane undergoes thermally activated constrictions. Then, the constricted dislocation splits into a pair of partial in the cross-slip-plane. Finally, the dislocation moves under an applied stress in the cross slip plane. However, because of high SFE in Al, this mechanism is not assumed to be rate controlling [21].

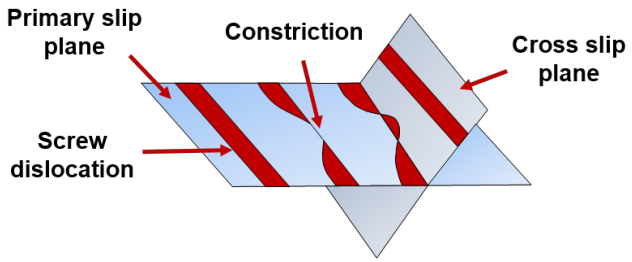


*Figure 2.8. Schematic of activated cross-slip.*

*Grain Boundary (GB) Migration and Sliding:* In dispersion strengthened alloys, GB migration can experience Zener pinning pressure given as $P_z = 3F_v\gamma_{GB}/d$ where $P_z$ = Zener pressure on the boundary from pinning dislocations; $F_v$ = vol. fraction of pinning dispersoids, $\gamma_{GB}$ = GB surface energy and $d$ = dispersoid diameter. The activation energy in this case is higher than self-diffusion. Grain boundary sliding on the other hand occurs usually at the end of creep life and involves cavitation at grain triple junctions (Fig. 2.10) [27].

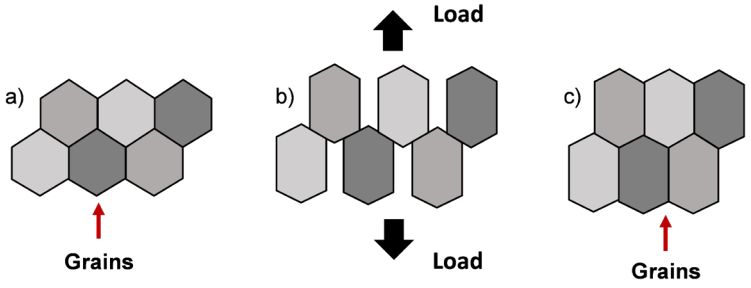


*Figure 2.9. Schematic of grain boundary migration and sliding: a) initial configuration of the grains; b) elongated grains causing cavitation due to tensile load; c) grains slide to prevent cavitation.*

*Dislocation-climb in dispersion strengthened alloys:* The activation energy for dislocation climb is equal to $q_{SD}$. In alloys strengthened with particles, creep involves climb over the obstacle and

the apparent activation energy for creep is higher than $q_{SD}$ (Fig. 2.11). To explain the deviation of the apparent activation energy of climb from $q_{SD}$ in dispersion strengthened alloys, a threshold stress was introduced in the creep equations [28–32]. The concept of threshold stress is convenient because it aligns the activation energy for creep with that of self-diffusion. However, the threshold stress is an empirical parameter that is not always supported by microstructural investigation. Its dependence on temperature and stress cannot be explained by models [33]. Different models give different threshold stress ranging from 3 MPa to 330 MPa at a given temperature for the same material [34]. There are two *physical models* that explain the threshold stress of creep in particle-strengthened alloys: (i) one involves threshold stress arising from the lengthening of the dislocation line as it climbs over the obstacle and (ii) the other involves additionally the detachment of the particle from the pinning obstacle. Here. $L =$ interparticle distance in both models.

(i) *Local and General Climb of Dislocations over Obstacles without particle attraction to dislocations*. The climb of edge dislocations occurs by increasing the length of the dislocation. The apparent threshold stress is $\tau_c = 0.19\frac{Gb}{L}$ for local climb is confined to the particle–matrix interfacial region and $\tau_c = 0.004\ to\ 0.02\frac{Gb}{L}$ for general climb where the climbing region extends beyond the interfacial region, well into the matrix (Fig. 2.11.a) [32].

(ii) *Climb and Detachment from the Obstacle*: A second mechanism involves dislocation climb accompanied by detachment of the dislocation from the particle to which it is attracted. The detachment stress for non-coherent particles was suggested to be thermal and approximated as $Gb/3L$ (Fig. 2.11.b) [33].

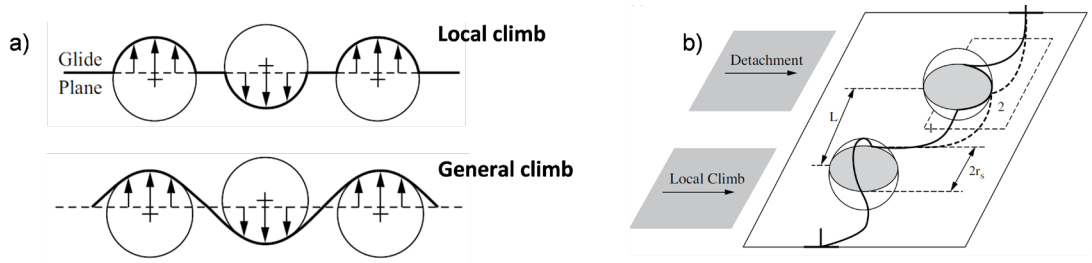


*Figure 2.10. Schematic of dislocation-climb in dispersion strengthened alloys: a) Local and general climb of dislocations over obstacles without particle attraction to dislocation; b) Climb and detachment from the obstacle.*

## 2.4 Strengthening Mechanisms

As described in section 2.3, thermal stability plays an important role in the creep resistance, becoming the next frontier for aluminum alloys. Therefore, its improvement depends on identifying factors stabilizing their microstructure at the diesel engine service conditions. In this section, the strengthening mechanisms such as alloying, heat treatment, particle size, volume fraction, homogeneous distribution, shape of particles and interfacial bonding are discussed due to their effectiveness and contribution in the strength of aluminum alloys at high temperature.

### 2.4.1 Alloying

Alloying elements in aluminum alloys may increase the thermal stability due the grain refinement (alloying elements promote the formation of smaller grains during solidification or recrystallization processes), solid solution hardening (alloying elements distort the lattice structure, making it more difficult for dislocations to move through the material) and dispersoid strengthening (alloying elements can result in the formation of second-phase particles dispersed in the matrix acting as obstacles to dislocation movement) [20]. However, some crucial

characteristics of the alloying elements need to be considered for a precipitate to be thermally stable in the aluminum matrix:

- Slow diffusion rate: Alloying elements with slow diffusion rates minimize the movement of atoms within the aluminum alloy, making it less likely for them to redistribute and form new precipitates or dissolve existing ones [20,35].

- Low solid solubility: If the alloying elements have low solid solubility in the aluminum matrix, they are more likely to precipitate out of solution during cooling or aging processes. This means that as the alloy is cooled or aged, the solute atoms will exceed their solubility limit in the aluminum matrix, leading to the formation of precipitates. Additionally, low solid solubility helps prevent the dissolution of precipitates at elevated temperatures [20,35].

### 2.4.2 Heat Treatment

Heat treatment may increase the thermal stability from the precipitation of dispersoid particles out inside the grains along the crystal boundaries or in the slip planes between the crystals, producing hindering slippage [36]. The common steps in the heat treatment for creep resistance aluminum alloys include solid solution heat treatment, quenching (commonly done in water), and natural and artificial ageing. However, certain factors need to be considered during the heat treatment to achieve a thermally stable microstructure:

- Influence of time and temperature: In solid solution, aluminum alloys are heated to temperatures above the solvus temperature to dissolve alloying elements into the aluminum matrix. The duration of heating is crucial for achieving complete dissolution of them. On

the other hand, the aging temperature is typically below the solvus temperature. Here, the temperature and time of aging influence the size, distribution, and density of precipitates [37,38].

- Influence of quenching: The rapid cooling rate suppresses the formation of equilibrium phases, allowing the retention of a metastable microstructure. In other words, these metastable phases are thermodynamically unstable but kinetically trapped due to rapid cooling, providing temporary strengthening effects until subsequent aging treatments to form equilibrium phases [37,39].

### 2.4.3 Particle Features

Particles may control thermal stability, but their influence on the creep resistance depends on size, volume fraction, distribution and shape [40]. When the particles are small and in a high volume fraction, the number of grain boundaries increases. This leads to finer grain structures in the aluminum matrix that hinder the movement of defects, such as dislocations. Additionally, when nanoparticles resist coarsening during high-temperature exposure, the fine microstructure is persevered. On the other hand, a homogeneous distribution of particles throughout the aluminum matrix is crucial for maximizing the benefits of dispersion strengthening and thermal stability because poor dispersion results in particle agglomeration, leading to localized weakening and non-uniform properties. Last but least, an optimal particle shape influences thermal stability, i.e. spherical nanoparticles tend to disperse more uniformly and minimize stress concentrations [41].

### 2.4.4 Interfacial Bonding

The stability of interfaces between nano-scale precipitates and aluminum matrix significantly influences in the thermal stability during creep deformation. Some of the effects related with this behavior are described as follows:

- Grain boundary segregation: Interfacial bonding affects the diffusion kinetics of alloying elements and impurities within the microstructure wherein creep deformation facilitate their diffusion along grain boundaries or interfaces. Consequently, stronger interfacial bonding can reduce the diffusion of impurities, which in turn improves the thermal stability of the alloy by minimizing grain boundary migration and coarsening at elevated temperatures [42].

- Precipitate stability: Strong bonding ensures that precipitates remain effectively dispersed and resistant to coarsening or dissolution, maintaining the creep resistance over time [43].

- Thermal activation barrier: Interfacial bonding influences the energy barrier for thermally activated processes. Stronger bonds between atoms or phases in the alloy hinder the movement of dislocations, requiring higher activation energies for creep deformation to occur [44].

## 2.5 Recent Studies on Creep Resistant Aluminum Alloy

Studies in creep resistant aluminum alloys continuously advance our knowledge and technology in using aluminum for elevated temperature applications. Recent studies that have occurred during the course if this PhD work has been reviewed and published as a Review paper which is given separately as Chapter 4 of this thesis. As a brief summary we can state the following have been reviewed:

- In Al-Si-Cu-Mg alloys, modifications of α-Al(Mn,Fe)Si with low additions of Mo, Mn, and Cr have a beneficial role by increasing the coherency, thermal stability, and the coherency of the dispersoids. Though the findings can still be considered a work in progress, the efficiency of the modified dispersoids can be ranked in descending order of effectiveness as:

$$\alpha\text{-Al(Fe,Mo)Si} > \alpha\text{-Al(Mn,Cr,Fe)Si} > \alpha\text{-Al(Mn,Mo,Fe)Si}$$

- Recent years have also looked at Al-Cu-based alloys that show lower minimum creep rates than the Al-Si-based alloys. However, these alloys are known to have lower castability and can have ductility and corrosion problems. In both alloy systems, the combined addition of Zr and Sc generates the Al3(Sc,Zr) phase, which seems to lead to the lowest creep rates.

- A detailed look at the most recent studies on Al-Si-Cu-Mg and Al-Cu alloys as well alternative way to improve creep resistance in aluminum are presented in The Review paper of Chapter 4.

## 2.6 Strategy and Methodology of the Study

Literature review shows that dispersion strengthening is a key design feature for improving the dislocation creep resistance of aluminum-silicon alloys. However, there are many diverse studies where creep test stresses and temperatures used differ and comparisons become difficult to make. Another difficulty is related to the extensive use of the concept of threshold stress in the creep studies of dispersion strengthened aluminum alloys. As mentioned in section 2.3.1, the threshold stress is an empirical parameter that is not always supported by microstructural investigation and cannot help the alloy designer which thermally activated creep mechanism is operative in the alloy and how the dispersoids react with microstructural features in alloy so that alloy design can be improved.

The strategy adopted in this study is to relate the experimentally determined empirical apparent activation energy to activation energies of dislocation creep processes such as dislocation climb, grain boundary migration, etc. discussed in section 2.3.1. The methodology follows three steps:

Step 1: Casting and heat treatment (T7) of the alloys.

Step 2: Creep testing of the alloys under Diesel engine operation conditions of 28 MPa and 300 – 350 °C and determine the apparent activation energy.

Step 3: Non-equilibrium and equilibrium thermodynamic simulation of phase selection in the alloys for (a) as-cast condition (non-equilibrium Scheil simulation) and (b) solutionized, T7 aged conditions (equilibrium high temperature simulations).

Step 4: Observing and analyzing creep tested samples by advanced electron microscopy techniques of transmission electron microscopy (TEM), high resolution transmission electron microscopy (HRTEM) and electron backscatter diffraction (EBSD) to determine and assess the creep processes occurring in the alloy and to calculate the activation energies that can be compared to the experimentally determined activation energies.

# CHAPTER 3: THE SYNERGISTIC EFFECTS OF NANO-SIZED α-Al(Mn,Cr,Fe)Si AND Al-Si-Zr DISPERSOIDS ON THE CREEP BEHAVIOR Al-Si-Mg-Cu (Mn, Cr, Zr) DIESEL ENGINE ALLOY

Mn, Cr and Zr form dispersoids of high thermal stability and volume fraction, resulting in the development of creep-resistant Al-Si-based alloys. The first part of the PhD research studied the effect of Mn, Cr and Zr on an Al-Si-Mg-Cu alloy. Al-7Si-0.3Mg-0.5Cu (MG1) and Al-7Si-0.3Mg-0.5Cu-0.15Mn-0.25Cr-0.15Zr (MG2-1) were creep tested and the activation energies systematically studied via electron microscopy to identify the rate controlling creep mechanisms. This chapter has been published as a journal article: R.I. Arriaga-Benitez, M. Pekguleryuz, The synergistic effects of nano-sized α-Al(Mn,Cr,Fe)Si and Al–Si–Zr dispersoids on the creep behavior Al–Si–Mg–Cu (Mn, Cr, Zr) diesel engine alloy, Mater. Sci. Eng. A. 872 (2023) 144949.

## ABSTRACT

The influence of Mn, Cr and Zr on the creep behavior of an Al-Si-Mg-Cu alloy intended for Diesel engine applications was studied. Two alloys, base alloy Al-7Si-0.3Mg-0.5Cu (MG1) and Al-7Si-0.3Mg-0.5Cu-0.15Mn-0.25Cr-0.15Zr (MG2-1) were creep tested at 300-350 °C and 28 MPa in the T7 heat-treated and soaked (100 hr at 300 °C) condition. The apparent activation energy for creep for MG1 was 184 kJ $mol^{-1}$ and for the MG2-1 was 234 kJ $mol^{-1}$. The two alloys exhibited differing rate controlling creep mechanisms. The minimum creep rates of the MG2-1 alloy were 3-5 times lower than the MG1 alloy at 300 °C and 325 °C, respectively and only 1.3 times lower at 350 °C. The TEM investigation indicated creep deformation in the MG2-1 alloy was due to thermally activated restoration processes where grain boundary migration experienced Zener pinning by coherent and ~5 nm $\alpha_{MG2\text{-}1}$-Al(Mn,Cr,Fe)Si. In the MG1 alloy, the creep mechanism was identified as climb over nano-sized (~50 nm) non-coherent α-Al(Mn,Fe) dispersoids. EDS analysis showed that semi coherent Q' phase (near equilibrium version of Q phase) existed in the MG1 alloy that had a nucleating role for nano-sized non-coherent α-Al(Mn,Fe) dispersoids.

*Keywords: Dispersoid; Al alloy; Creep; TEM; Thermodynamic calculation*

## 3.1 Introduction

The vehicle technologies are seeing continuous improvement to meet the challenges of global warming. Electric passenger vehicles are addressing effectively the difficulties of cost, range, and infrastructure [1]. The electrification of heavy vehicles (trucks, construction, military, agriculture, mining and railroad) on the other hand is slow and they rely on Diesel engines for fuel economy, performance, reliability, and durability [1,2]. Weight reduction of the Diesel engine through the use of lightweight aluminum alloys the engine block and cylinder heads is an effective way to contribute to the fuel efficiency, performance and reduction in the $CO_2$ emissions [3]. These engine components operate at temperatures up to 300 °C leading to warp and damage within areas exposed to high thermal gradients generating concerns over durability when commercial aluminum alloys are used.

Alloy development on commercial alloy A356 (Al-Si-Mg) with modified Mg, Cu levels and Ni additions on the one hand, and with alloying additions to form intermetallics and dispersoids on the other hand have led to first and second generation of aluminum alloys for diesel engine blocks and cylinder heads [4–7]. It has also been demonstrated that combined additions of Cr, Zr, and Mn to the commercial alloy A356+0.5%Cu lead to the formation, good distribution and large amount of dispersoids enhancing the creep properties at 300 °C in the 20-30 MPa stress range [8]. These alloys with the addition of peritectic elements are classified as third generation of aluminum diesel engine alloys. Alloys with different peritectic element additions have since been researched [9–12]. In 2008, our research team at McGill University added Cr in combination with Mn and Zr to the A356 + 0.5Cu alloy producing submicron dispersoids and leading to an 8% improvement in creep resistance. In 2014, Farkoosh et al. developed an Al–Si–Cu–Mg–0.3Mo-0.5Mn alloy with

thermally stable dispersoids eliminated the dispersoid-free zones (DFZ) and led to a uniform distribution of dispersoids. The alloy increased creep time-to-fracture and strain-to-fracture at 300°C [8,13].

However, a systematic study of the creep behavior of these alloys has not been undertaken. In order to further develop and design creep resistant aluminum alloys, creep micro-mechanisms of these alloys need to be determined. For dispersoid strengthened alloys, recent work has adopted the concept of threshold stress that is experimentally determined; however, electron microscopy studies of the alloys have not discovered real features that can explain the empirical threshold stress [14]. These studies cannot tell us the exact role of the microstructural features, nor can they identify which precipitates or dispersoids are interacting with dislocations. The objective of the present study is to pave the path towards a detailed understanding of the roles of second phases on the creep behavior of two aluminum.

## 3.2 Background on creep mechanisms

A background on creep activation energies are given in this paper in order to provide a tool to identify the creep micromechanisms in alloys. Creep can be classified as dislocation creep, diffusional creep and grain boundary sliding [15,16]. For light metals Al and Mg, the service conditions on powertrain components have usually presented dislocation creep conditions or grain boundary migration/sliding. Important *dislocation creep mechanisms* that can be thermally aided are dislocation intersection, movement of dislocation with jogs, dislocation climb, movement of dislocation atmospheres and activated cross-slip. Depending on the mechanism the activation energy for dislocation creep can vary. Activation energies for creep mechanisms can be estimated based thermally activated processes [15,17]. A few are described below and listed in Table 3.1.

**Dislocation Creep***: Dislocation intersection*: The activation energy $q$ for this mechanism is composed of the activation energy for jog creation and the work done by stress $\tau$ to push the dislocation segment to the stress field of the other dislocation as shown in Table 3.1. Gittus [18] concluded that the activation energy for dislocation intersection is close to the activation energy for self diffusion, $q_{SD}$. *Movement of dislocations with jogs*: this process involves screw dislocations which already have jogs and which can move by thermal activation, $q_j$, that is equal to the energy for vacancy formation, $q_f$, and the energy to move the vacancy away, $q_m$. The sum of these values is the activation energy for self-diffusion, $q_{SD}$. *Movement of dislocation atmospheres (viscous glide):* The process involves the movement of dislocations below the yield strength due to the dislodge of solute atmospheres and the rate is proportional to the diffusion rate of the solute atoms.

*Table 3.1. Micro-mechanisms of dislocation creep.*

| Mechanism | Activation energy | Ref. |
|---|---|---|
| Dislocation Intersection | $q = q_o - \tau b^2 l$ where $q_o = \alpha \mu b^3$, $q \sim q_{SD}$ | [15,18] |
| Movement of Dislocations with Jogs | $q_d = q_f + q_m = q_{SD}$ | [15] |
| Dislocation Climb | $q = q_d + q_j = q_{SD}$ | [15] |
| Movement of Dislocation Atmospheres | $q_s =$ activation energy for solute diffusion | [15] |
| Activated Cross-Slip | Related to the SFE which is high in aluminum, and not rate-controlling. | [19] |
| Grain Boundary Migration without Boundary Pinning | Low angle boundaries $\sim q_{SD}$<br>High angle boundaries $\sim 3/5\, q_{SD}$ | [16,20] |

$q_d =$ Activation energy for movement of dislocation atmosphere, $b$ is Burger's vector, $l$ is length of dislocation that moves during intersection (spacing between dislocations), and $\mu$ is shear modulus.

**Diffusional Creep:** Diffusional creep occurring at high temperatures can be lattice diffusion or

diffusion through fast diffusion pathways (dislocation pipe diffusion, grain boundary diffusion); the activation energies are equal to or lower than self-diffusion, $q_{SD}$.

**Grain Boundary (GB) Migration and Sliding**: Grain boundary migration can involve phase transformations at the boundary or grain or sub-grain growth. The activation energy of sub-grain boundary migration is approximated with $q_{SD}$. The activation energy for GB migration is lower than $q_{SD}$. In dispersion strengthened alloys, GB migration can experience Zener pinning pressure [20] given as $P_z = 3F_v\gamma_{GB}/d$ where $P_z =$ Zener pressure on the boundary from pinning dislocations; $F_v =$ vol. fraction of pinning dispersoids, $\gamma_{GB} =$ GB surface energy and $d =$ dispersoid diameter. The activation energy in this case is higher than self-diffusion. Grain boundary sliding on the other hand occurs usually at the end of creep life and involves cavitation at grain triple junctions.

**Dislocation-climb in dispersion strengthened alloys:** The activation energy for dislocation climb is equal to $q_{SD}$. In alloys strengthened with particles, creep involves climb over the obstacle and the apparent activation energy for creep is higher than $q_{SD}$. To explain the deviation of the apparent activation energy of climb from $q_{SD}$ in dispersion strengthened alloys, a threshold stress was introduced in the creep equations [21–25]. The concept of threshold stress is convenient because it aligns the activation energy for creep with that of self-diffusion. However, the threshold stress is an empirical parameter that is not always supported by microstructural investigation. Its dependence on temperature and stress cannot be explained by models [26]. Different models give different threshold stress ranging from 3 MPa to 330 MPa at a given temperature for the same material [27]. There are two *physical models* that explain the threshold stress of creep in particle-strengthened alloys: (i) one involves threshold stress arising from the lengthening of the dislocation

line as it climbs over the obstacle and (ii) the other involves additionally the detachment of the particle form the pinning obstacle. Here. $L =$ interparticle distance in both models.

(i) *Local and General Climb of Dislocations over Obstacles without particle attraction to dislocations*. The climb of edge dislocations occurs by increasing the length of the dislocation. The apparent threshold stress is $\tau_c = 0.19\frac{Gb}{L}$ for local climb is confined to the particle–matrix interfacial region and $\tau_c = 0.004\ to\ 0.02\frac{Gb}{L}$ for general climb where the climbing region extends beyond the interfacial region, well into the matrix [25].

(ii) *Climb and Detachment from the Obstacle*: A second mechanism involves dislocation climb accompanied by detachment of the dislocation from the particle to which it is attracted. The detachment stress for non-coherent particles was suggested to be thermal and approximated as $Gb/3L$ [26].

The present work focusses on understanding the creep mechanisms of two dispersion-strengthened aluminum alloys based on electron microscopy analyses of creep tested samples. Microstructural features observed in creep testing are used to assess the creep mechanisms and to calculate activation energies that can explain the experimentally determined apparent activation energies.

## 3.3 Experimental procedures

Two alloys with nominal compositions (wt.%) of Al-7Si-0.3Mg-0.5Cu (MG1) and Al-7Si-0.3Mg-0.5Cu-0.15Mn-0.25Cr-0.15Zr (MG2-1) were melted in a silicon carbide crucible at 760 °C using a high frequency NORAX (Canada) induction furnace. Each alloy was modified with 150 ppm Sr using a master alloy (Al-10wt.% Sr) to modify the eutectic Si morphology. After 3 minutes of degassing with high purity argon gas at a flow rate of 1 L $min^{-1}$, the melt was poured at 730 °C

into a constrained-rod casting mold preheated to 400 °C. The chemical composition of the alloys was determined by Inductively Coupled Plasma (ICP) technique (Table 3.2). The silicon levels differ by 1wt.% and align well with the usual range of ~1wt% in Si in commercial aluminum alloys. Si does not necessarily affect creep properties to a large extent. Cu can influence creep properties due to the effect of precipitates and dispersoids are expected to exert significant effect on dislocation creep, so differences in the creep behavior of these two alloys are expected.

Two cast rods obtained from each alloy were machined according to the ASTM E8 to produce tensile creep test specimens. Samples were exposed to a two-stage solution treatment for 4 hours at 500 °C and 10 hour at 540 °C to avoid probable incipient melting by using an electrically heated, air-circulating chamber furnace. Each sample was quenched in water at room temperature followed by ageing at 200 °C for 5 hours (T7). Tensile creep testing was performed at 300, 325 and 350 °C under a constant load at 28 MPa. The stress value and the temperature range were selected so as to simulate diesel-engine operation conditions. The temperature was monitored using a thermocouple with an error of ± 0.1°C attached to the specimen while the gauge length displacement was measured with two high precision extensometers with a resolution of 5 μm. All tests were conducted in air along with a soak of 100 hours at 300 °C prior to testing. Each test was later analyzed to determine the activation energy via Arrhenius plots of creep-strain versus inverse temperature. A minimum of three data points were obtained from each specimen.

Specimens for microstructural study were performed on as-cast and T7 alloy samples sectioned with a low-speed diamond saw and ground with a series of SiC papers. Samples were initially polished with an $Al_2O_3$ solution on a porous neoprene polishing cloth and finished with colloidal silica solution using a Buehler vibratory polisher. A Hitachi SU-3500 Variable Pressure –SEM was used at 15 kV to examine the elemental analysis and surface morphology. TEM analyses were

performed on thin foils prepared in a Gatan Precision Ion Polishing System (PIPS). A Philips CM200 microscope operated at 200 kV was used to determine the dislocation-dispersoid interactions, dislocation activity and dispersoid formation.

*Table 3.2. Chemical compositions of the alloys.*

| **Alloy** | **Chemical Composition (wt.%)** | | | | | | | | | |
|---|---|---|---|---|---|---|---|---|---|---|
| | Si | Mg | Cu | Fe | Ti | Mn | Zr | Cr | Sr | Al |
| **MG2-1** | 6.09 | 0.30 | 0.50 | 0.10 | 0.10 | 0.17 | 0.17 | 0.23 | 0.014 | Bal. |
| **MG1** | 7.01 | 0.30 | 0.58 | 0.10 | 0.10 | <0.01 | <0.01 | <0.01 | 0.014 | Bal. |

## 3.4 Results

### 3.4.1 Phase Selection and Microstructure of As-Cast MG1 and MG2-1

Phase selection in the cast alloys was determined using non-equilibrium Scheil simulation via the FactSage software (with FTlight database). Scheil calculations that assume complete mixing in the liquid and no back-diffusion in the solid simulates well the permanent mold casting used in this study. The results of the simulations were then compared to microstructural characterization using SEM/EDS.

*Phase Selection in base-alloy MG1 (Al-7Si-0.3Mg-0.5Cu):*

According to the calculated diagram (Fig. 3.1) of the base alloy, solidification starts at 615 °C with the precipitation of the α-Al phase followed by the formation of a eutectic α-Al and Si at 570 °C. With a further decrease in temperature, solidification proceeds with the formation of the β-$Al_5FeSi$ phase at 569 °C and π-$Al_8FeMg_3Si_6$ phase at 553 °C. Subsequently, a negligible amount of M-$Mg_2Si$ phase forms at 542 °C. However, this phase transforms into the Q-$Al_5Cu_2Mg_8Si_6$ phase at

537 °C. Solidification terminates at 514 °C with the formation of the θ-$Al_2Cu$ phase. Table 3.3 illustrates the different reactions occurring during non-equilibrium solidification.

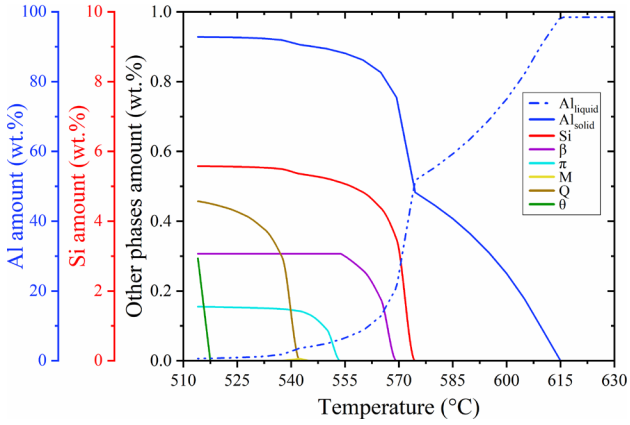


*Figure 3.1. Scheil cooling of the MG1 alloy as a function of temperature.*

*Phase Selection in MG2-1 (Al-7Si-0.3Mg-0.5Cu-0.15Mn-0.23Cr-0.15Zr):*

According to the calculated diagram (Fig. 3.2) of cast Al-7Si-0.3Mg-0.5Cu-0.15Mn-0.23Cr-0.15Zr (MG2-1), the solidification starts at 615 °C with the co-precipitation of the α-Al and ε-Al-Si-Zr phases followed by the formation of the Si phase at 574 °C. The solidification continues with the formation of the $\alpha_{MG2\text{-}1}$-Al(Mn,Cr,Fe)Si phase at 569 °C and the π-$Al_8FeMg_3Si_6$ phase at 553 °C. As the temperature decreases, the M-$Mg_2Si$ phase precipitates at 542°C and transforms into the Q-$Al_5Cu_2Mg_8Si_6$ phase at 537 °C. Solidification terminates at 514 °C with the formation of the θ-$Al_2Cu$ phase. Table 3.3 illustrates the different reactions occurring during non-equilibrium solidification.

A comparison between these simulations indicates that additions of Mn, Cr and Zr to the base alloy result in the formation of ε-Al-Si-Zr and $\alpha_{MG2\text{-}1}$-Al(Mn,Cr,Fe)Si phases where ε-Al-Si-Zr along with α-Al phase are the first to precipitate. Calculations also show that the precipitation of $\alpha_{MG2\text{-}1}$-Al(Mn,Cr,Fe)Si suppressed the formation of β-$Al_5FeSi$ phase and increased the temperature of

solidification from 560 °C to 569 °C (Table 3.3). On the other hand, the temperature of solidification for the formation of Al-Si, π-$Al_8FeMg_3Si_6$, Q-$Al_5Cu_2Mg_8Si_6$ and θ-$Al_2Cu$ phases remain unchanged in both alloy systems.

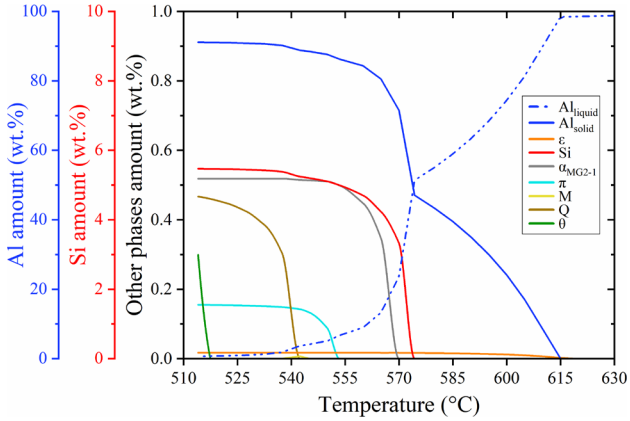


*Figure 3.2. Scheil cooling of the MG2-1 alloy as a function of temperature.*

*Table 3.3. Reactions in the MG2-1 and MG1 alloys.*

| **MG2-1 alloy** | | **MG1 alloy** | |
|---|---|---|---|
| **Reaction** | **Scheil (°C)** | **Reaction** | **Scheil (°C)** |
| L➔α-Al+ε | 615 | L➔α-Al | 615 |
| L➔α-Al+ε+Si | 574 | L➔α-Al+Si | 574 |
| L➔α-Al+ε+Si+$\alpha_{MG2-1}$ | 569 | L➔α-Al+Si+β | 560 |
| L➔α-Al+ε+Si+$\alpha_{MG2-1}$+π | 550 | L➔α-Al+Si+β+π | 550 |
| L➔α-Al+ε+Si+$\alpha_{MG2-1}$+π+M | 542 | L➔α-Al+Si+β+π+M | 542 |
| L+M➔α-Al+ε+Si+$\alpha_{MG2-1}$+π+Q | 537 | L+M➔α-Al+Si+β+π+Q | 537 |
| L➔α-Al+ε+Si+$\alpha_{MG2-1}$+π+Q+θ | 514 | L➔α-Al+Si+β+π+Q+θ | 514 |

*Microstructures of As-Cast Alloys:*

SEM images showing the as-cast microstructures of the alloys studied are presented in Fig. 3.3. EDS elemental mapping and EDS point scanning (Table 3.4) together with the results of FactSage simulations were utilized to identify the phases in each alloy. The MG2-1 and MG1 alloys changed the morphology of the silicon from acicular to fine fibrous due to Sr modification.

SEM analysis (Fig. 3.3) indicates the presence of α-Al dendrites, and the Al-Si eutectic, in both alloys. There is also the presence of an Al-Cu and an Al-Cu-Mg-Si phase in both alloys. Based on the simulations and ref. [8,9] these are θ-$Al_2Cu$ and Q-$Al_5Cu_2Mg_8Si_6$ phase.

*MG1 Alloy*: Fig. 3.3a shows the presence of an Al-Fe-Si and Al-Fe-Mg-Si phase with a plate-like and Chinese-script morphology. Based on the FactSage simulations these are the β-$Al_5FeSi$ phase and the π-$Al_8FeMg_3Si_6$ phases.

*MG2-1 Alloy*: Fig. 3.3b shows a Cr, Mn modified Al-Fe-Si phase. The addition of Cr-Mn to the base alloy MG1 resulted in the formation of the $\alpha_{MG2\text{-}1}$-Al(Mn,Cr,Fe)Si intermetallic phase as is indicated by the thermodynamic calculations. This is a modified β-$Al_5FeSi$. This phenomenon can be ascribed to the similarity of Fe atoms to Cr and Mn which are able to substitute each other inside the crystal lattice [28] and that the nucleation of the $\alpha_{MG2\text{-}1}$-Al(Mn,Cr,Fe)Si intermetallic particles is governed by the diffusion of these atoms [29]. Unlike the simulations, an Al-Fe-Mg-Si phase (π-$Al_8FeMg_3Si_6$ phase) is not revealed by SEM/EDS. Fig. 3.3b also indicates the presence of a rod-like Zr-containing phase. This is the eutectic ε-Al-Si-Zr phase in agreement with the Scheil solidification calculations.

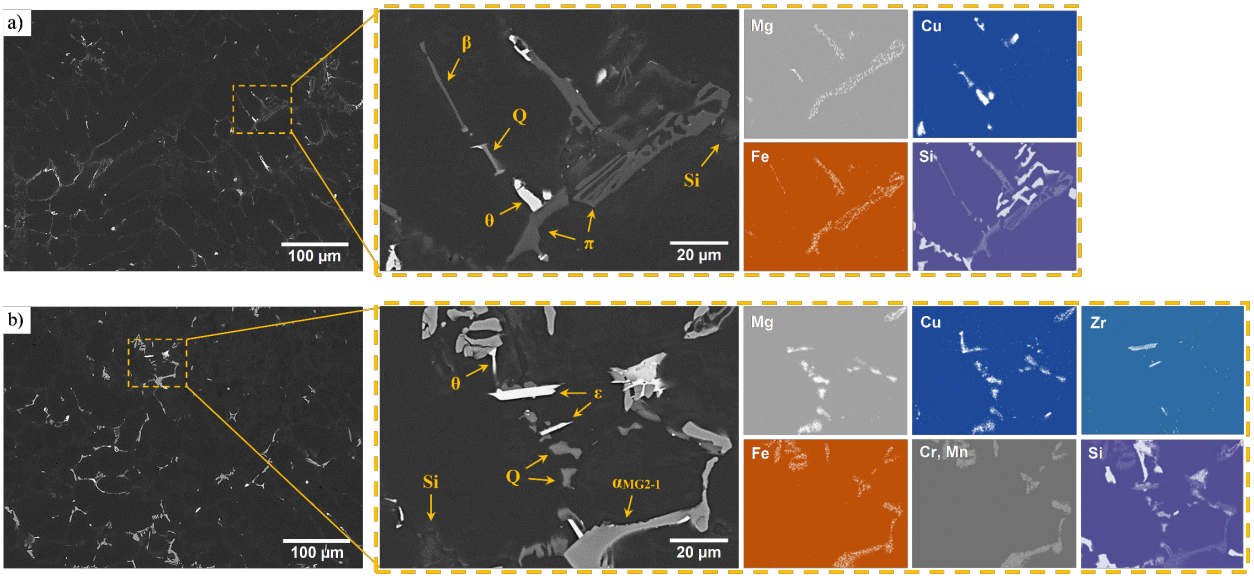

*Figure 3.3. Backscattered SEM of the as-cast microstructures along with EDS mapping at low and high magnifications of (a) MG1 and (b) MG2-1 alloys.*

*Table 3.4. Chemical composition of each phase by EDS point-scan in the as-cast condition.*

| **MG2-1 alloy** | | **MG1 alloy** | |
|---|---|---|---|
| **Phase** | **Chemical composition (wt.%)** | **Phase** | **Chemical composition (wt.%)** |
| ε | 37.6Al–13.4Si–49Zr | Si | 27Al–73Si |
| Si | 46.1Al–53.9Si | β | 71.6Al–8.6Fe–19.8Si |
| $\alpha_{MG2-1}$ | 61.2Al–9.4Mn–9.8Cr–8.3Fe–11.3Si | π | 54.7Al–10.4Fe–11.9Mg–23Si |
| Q | 35.2Al–17.3Cu–24.3Mg–23.2Si | Q | 72.1Al–26.5Cu–0.3Mg–1.1Si |
| θ | 66.4Al–33.6Cu | θ | 53.7Al–46.3Cu |

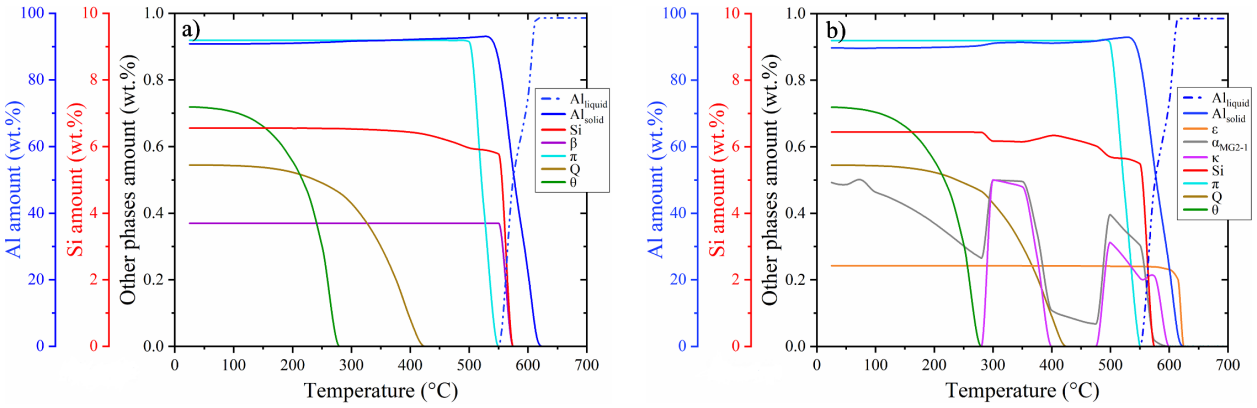


*Figure 3.4. Calculated equilibrium phase distribution of (a) MG1 and (b) MG2-1 alloys as a function of temperature.*

## 3.4.2 Phase Selection and Microstructures of (T7) Overaged Alloys

*Thermodynamic Simulations:*

Equilibrium calculations were carried out to estimate the type and amounts of precipitates in the MG1 and MG2-1 alloys in the T7 condition (solutionized at 500 °C and 540 °C followed by

overaging at 200 °C), as indicated in Fig. 3.4. The simulations indicate that when the solution treatment is performed (at 540 °C as the highest temperature), certain phases are dissolved and only ε-Al-Si-Zr, $\alpha_{MG2\text{-}1}$-Al(Mn,Cr,Fe)Si, κ-Al-Cr-Si and Al-Si eutectic phases in MG2-1 alloy and β-$Al_5FeSi$ and Al-Si eutectic phases in MG1 alloy remain.

*Table 3.5. Phases present and amounts in the MG2-1 and MG1 alloys.*

| **MG2-1 alloy** | | **MG1 alloy** | |
|---|---|---|---|
| **Phases present and amounts** | **Equilibrium (°C)** | **Phases present and amounts** | **Equilibrium (°C)** |
| 93% α-Al, 0.24% ε, 0.30% $\alpha_{MG2\text{-}1}$, 0.23% κ, 5.5% Si | 540 | 93% α-Al, 5.8% Si, 0.37% β | 540 |
| 92% α-Al, 0.24% ε, 0.39% $\alpha_{MG2\text{-}1}$, 0.31% κ, 5.7% Si, 0.90% π | 500 | 92% α-Al, 6.0% Si, 0.37% β 0.91% π | 500 |
| 91% α-Al, 0.24% ε, 0.50% $\alpha_{MG2\text{-}1}$, 0.50% κ, 6.2% Si, 0.91% π, 0.43% Q | 300 | 92% α-Al, 6.5% Si, 0.37% β 0.92% π, 0.43% Q | 300 |
| 90% α-Al, 0.24% ε, 0.37% $\alpha_{MG2\text{-}1}$, 6.4% Si, 0.91% π, 0.52% Q, 0.55% θ | 200 | 91% α-Al, 6.5% Si, 0.37% β 0.92% π, 0.52% Q, 0.55% θ | 200 |

This simulation can also report the presence and amount of precipitates at a certain temperature. At the overaging temperature (200 °C) the equilibrium microstructure of the MG1 alloy consisted of 6.5% Si, 0.37% β-$Al_5FeSi$, 0.92% π-$Al_8FeMg_3Si_6$, 0.52% Q-$Al_5Cu_2Mg_8Si_6$ and 0.55% θ-$Al_2Cu$. In MG2-1 alloy, the amount of θ-$Al_2Cu$ and Q-$Al_5Cu_2Mg_8Si_6$ remained constant while π-$Al_8FeMg_3Si_6$ transformed to $\alpha_{MG2\text{-}1}$-Al(Mn,Cr,Fe)Si with a total amount in the alloy of 1.41%. Mn, Cr and Zr additions resulted in the formation of 0.24% ε-Al-Si-Zr and 0.37% $\alpha_{MG2\text{-}1}$-Al(Mn,Cr,Fe)Si. Table 3.5 illustrates the phases present and amounts occurring during equilibrium solidification.

*Microstructures of T7 alloy:*

SEM images showing the T7 microstructures of the alloys are presented in Fig. 3.5. SEM

observations indicate that the Si phase is coarsened and spheroidized in both alloys but the phase is finer in the MG2-1 than it is in the MG1 alloy. This can be attributed to the nucleating effect of $\alpha_{MG2\text{-}1}$-Al(Mn,Cr,Fe)Si dispersoids [30].

*MG1 Alloy*: In MG1 alloy (Fig. 3.5.b), the π-$Al_8FeMg_3Si_6$ phase decomposed during solution treatment and is not seen in the T7 microstructure. The β-$Al_5FeSi$ phase was thermodynamically stable as previously determined via equilibrium calculations. The θ-$Al_2Cu$ phase was not observed in the SEM images, despite the fact that simulation indicated their existence. Recent investigation [7] has revealed the presence and growth of θ precipitates by prolonging the aging process (170 hours at 200 °C). This could explain its absence in the microstructures reveled in SEM images.

*MG2-1 Alloy*: In MG2-1 alloy, the $\alpha_{MG2\text{-}1}$-Al(Mn,Cr,Fe)Si phase and the ε-Al-Si-Zr phase were partially fragmented and coarsened. Fine dispersoids of $\alpha_{MG2\text{-}1}$-Al(Mn,Cr,Fe)Si were seen and identified throughout the microstructure (interdendritic region and inside the dendrites) by EDS analysis. Equilibrium calculation indicated the presence of the κ-Al-Cr-Si precipitates but they could not be observed via SEM analysis. κ-Al-Cr-Si particles is discussed in the TEM analysis section. The θ-$Al_2Cu$ phase was not observed in the microstructures indicating a similar behavior that in the MG1 alloy.

EDS point analysis was utilized to determine the variation in the chemical composition of each constituent in the as-cast to T7 condition for both alloys systems (Table 3.4, 3.6). The chemical analysis of the MG1 alloy indicated that during the decomposition of π-phase and the coarsened of the Si phase the amount of Si (wt.%) increased 17.8 in Al-Si eutectic and 1.1 in Q-phase but it was reduced 11.1 in β-phase. On the other hand, the dissolution of θ-phase increased the content of Cu in Q-phase about 14.6 wt.%. The chemical analysis of the MG2-1 alloy reveled that the

coarsened of the Si phase and the dissolution of the Q-phase contributed to a higher concentration in Al-Si eutectic and ε phases about 42.6 and 13.5, respectively. However, these processes did not affect the Si amount of the $\alpha_{MG2\text{-}1}$-phase.

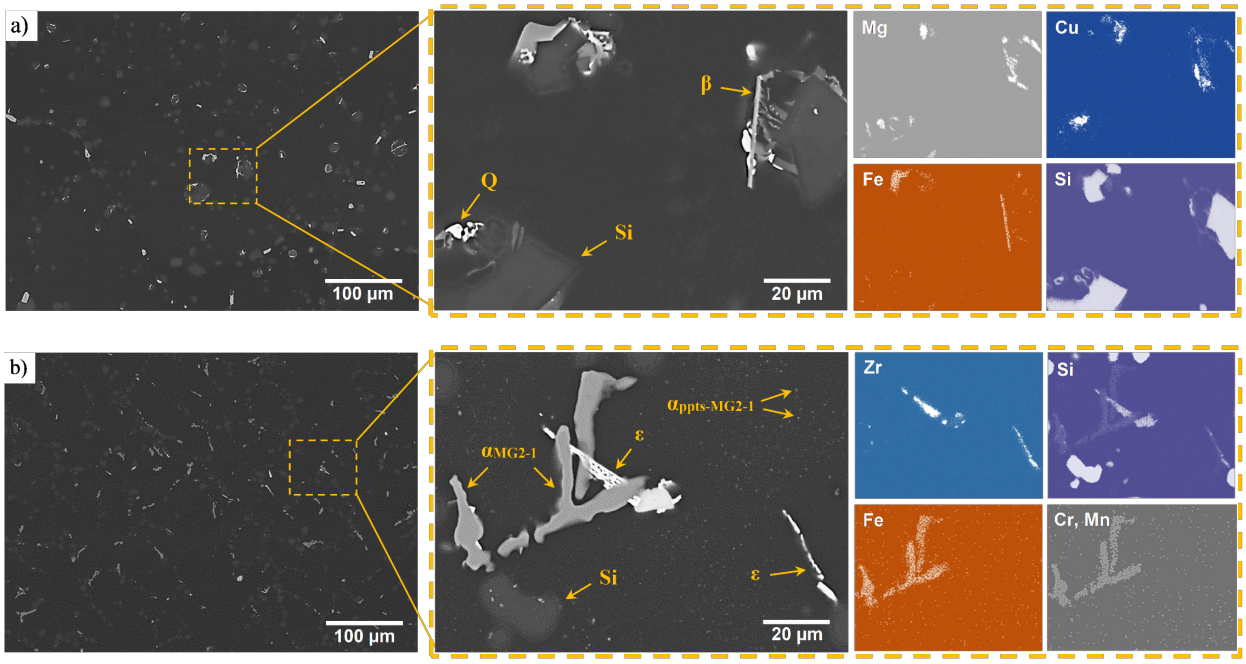


*Figure 3.5. Backscattered SEM of the T7 alloys along with EDS mapping at low and high magnifications of (a) MG1 and (b) MG2-1 alloys.*

*Table 3.6. Chemical composition of each phase by EDS point-scan in the T7 condition.*

| **MG2-1 alloy** | | **MG1 alloy** | |
|---|---|---|---|
| **Phase** | **Chemical composition (wt.%)** | **Phase** | **Chemical composition (wt.%)** |
| ε | 22.1Al–26.9Si–51Zr | Si | 9.2Al–90.8Si |
| Si | 3.5Al–96.5Si | β | 76.4Al–15Fe–8.7Si |
| $\alpha_{MG2\text{-}1}$ | 59.4Al–9.9Mn–10.2Cr–8.6Fe–11.9Si | Q | 54.6Al–41.1Cu–2.1Mg–2.2Si |
| $\alpha_{pps\text{-}MG2\text{-}1}$ | 93.8Al–1.4Mn–1.1Cr–0.8Fe–2.9Si | | |

### 3.4.3 Creep Behavior and Creep Activation Energy

Tensile creep tests were conducted on the MG1 and MG2-1 alloys at 300, 325 and 350 °C under a creep stress of 28 MPa, as shown in Fig. 3.6. All creep specimens were exposed to two-step solution treatment for 4 hours at 500 °C and 10 hours at 540 °C, followed by a soaking of 100 hours at 300 °C prior to creep testing to avoid in-situ coarsening of dispersoids and to stabilize the microstructure. Table 3.7 illustrates the creep time-to-fracture and steady state creep rate for both alloy systems at 300, 325 and 350 °C under 28 MPa.

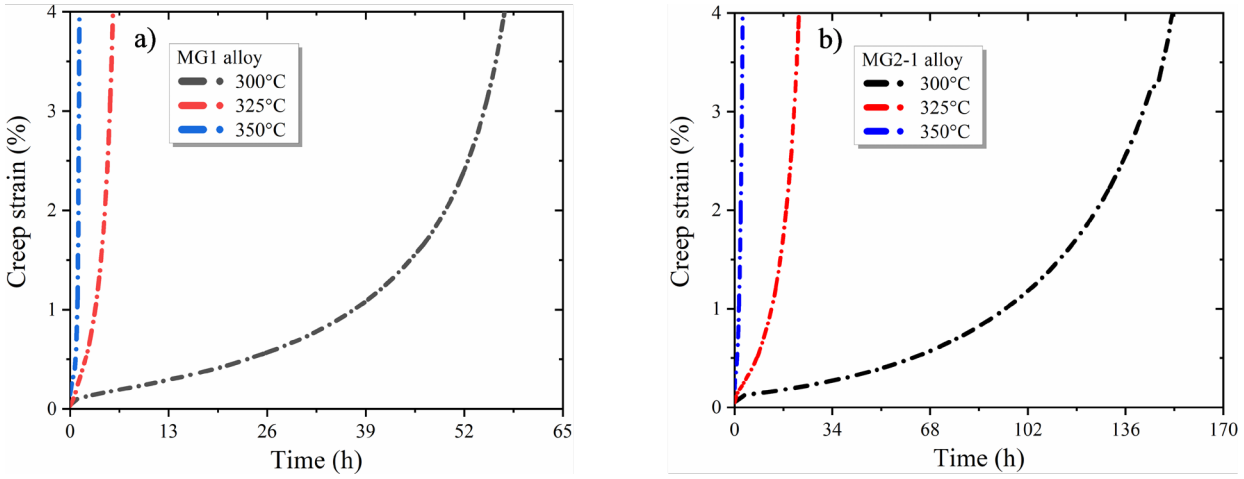


*Figure 3.6. Tensile creep test vs time under a creep stress of 28 MPa at 300 °C, 325 °C and 350 °C for (a) MG1 and (b) MG2-1 alloys.*

*Table 3.7. Creep features for MG2-1 and MG1 alloys at 300, 325 and 350 °C under 28 MPa.*

| | **MG2-1 alloy** | | | **MG1 alloy** | | |
|---|---|---|---|---|---|---|
| | **300 °C** | **325 °C** | **350 °C** | **300 °C** | **325 °C** | **350 °C** |
| **Creep time-to-fracture (h)** | 167 | 23.7 | 3.1 | 60 | 6.3 | 1.3 |
| **Steady state creep rate ($s^{-1}$)** | $1.41 \times 10^{-6}$ | $1.36 \times 10^{-5}$ | $7.26 \times 10^{-5}$ | $4.48 \times 10^{-6}$ | $6.94 \times 10^{-5}$ | $9.54 \times 10^{-5}$ |

The Arrhenius equation describes the effect of the temperature ($T$) and stress ($\sigma$) on the steady-state creep rate ($\dot{\varepsilon}_{ss}$), which is defined as $\dot{\varepsilon}_{ss} = A\sigma^{n_a} exp\left(-\frac{Q_a}{RT}\right)$, where $A$ is the pre-exponential

factor, $T$ is the absolute temperature in Kelvin, $n_a$ is the apparent stress exponent, $Q_a$ is the apparent creep activation energy and $R$ is the gas constant [31]. This relationship is applied to determine the apparent creep activation energy, $Q_a = -R\left(\frac{\partial \ln \dot{\varepsilon}_{ss}}{\partial\left(\frac{1}{T}\right)}\right)_{\sigma}$, stablished from the Arrhenius plot between ln $\dot{\varepsilon}_{ss}$ and $1000/T$ at a constant stress. The $Q_a$ calculated for the MG2-1 and MG1 alloys at temperatures of 300 °C, 325 °C and 350 °C under a creep stress at 28 MPa is shown in Fig. 3.7.

Fig. 3.7a, b. show that the value of $Q_a$ for MG1 is 184 kJ mol$^{-1}$ and for MG2-1 is 234 kJ mol$^{-1}$ that are both above the activation energy for self-diffusion (148 kJ mol$^{-1}$). As discussed above the creep mechanisms that can have activation energy above that for self-diffusion are movement of dislocations with solute atmosphere, dislocation climb with obstacles and grain boundary migration of low angle boundaries with Zener pinning. In order to assess the creep mechanisms, creep tested samples were analyzed via electron microscopy.

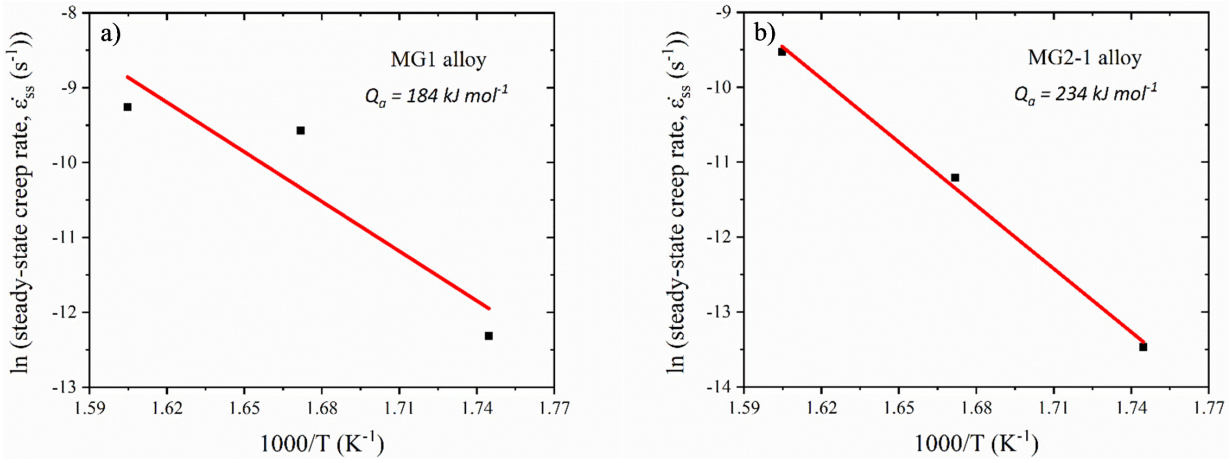


*Figure 3.7. Arrhenius plot of log of steady-state creep rate vs the reciprocal of temperature at 28 MPa for (a) MG1 and (b) MG2-1 alloys.*

*Investigation of the Creep Mechanism in Al-7Si-0.3Mg-0.5Cu (MG1) Alloy:*

The TEM images showing the microstructure of the MG1 alloy of the present study after tensile creep testing at 300 °C and 28 MPa are given in Fig. 3.8. Fig. 3.8a shows a precipitate free zone (PFZ) along the grain boundary with a calculated width of ~1.6 μm. PFZ have been observed in previous studies as well [32] and can be attributed to a non-optimized age-hardening treatment (due to a low solutionizing temperature, low quench rate and/or a high ageing temperature). No grain-boundary migration or cavitation is evident to indicate grain-boundary sliding as a potential creep mechanism. Fig. 3.8b shows dislocations pinned by particle obstacles. Two types of particles, (i) light grey and needle shaped and (ii) circular and black are detected (indicated in arrows). The image suggests that particle-dislocation interaction is involved in the creep process.

HRTEM image (Fig. 3.8c) reveals that the Al-Mg-Cu-Si precipitates are *coherent* with the Al matrix; the fringes in the interface are continuous with the Al matrix, having an inter-planar spacing of 0.3587 nm indicating a 4.5% mismatch with the aluminum matrix. These precipitates may be intermediates of the Q-$Al_5Mg_8Cu_2Si_6$ precipitate indicating that the alloy had not reached a full T7 condition. The rod-shape morphology agrees with the coherency/semi-coherency of the precipitate and strongly suggests that the Al-Mg-Cu-Si is near equilibrium. Cu and Mg content in the Q' precipitates was ~15% and ~12%, respectively. In this study this phase will be termed the Q' phase. Fig. 3.8d presents an enlarged view from Fig. 3.8b showing dislocations arcing over nano-sized (~50 nm) non-coherent α-Al(Mn,Fe) dispersoids. Fig. 3.8e shows the elemental mapping of needle-type Al-Mg-Cu-Si precipitates and their distribution in the microstructure. The corresponding SAED pattern (Fig. 3.8f) exhibits diffuse spots around α-Al matrix (the largest dot). These spots are identified as Q-precipitates (large dots) and α-precipitates (small dots). The SAED pattern suggests that α-precipitates exist in a larger amount than Q-precipitates. TEM observations

also reveal (Fig. 3.8g) the existence of Si, Sr and α-Al(Mn,Fe)Si particles in addition to the Q' phase. The EDS analysis on an α-Al(Mn,Fe)Si precipitate indicated Fe and Mn contents of ~28% and ~9%, respectively. EDS results demonstrate that Q' precipitates are associated with α-Al(Mn,Fe)Si particles; α-Al(Mn,Fe)Si is usually a non-coherent precipitate which can transform during solutionizing into a partially coherent phase [33–35].

FactSage calculations (Fig. 3.4) also indicate that the equilibrium microstructure of the MG1 alloy at 300 °C the creep temperature consists of 6.5% Si, 0.37% β, 0.92% π and 0.43% Q. Tables 3.3 and 3.5 show the phases present and amounts in the alloys. Microstructural investigation, on the other hand, indicates that the alloy has α-Al(Mn,Fe) dispersoids rather than β and π dispersoids. The π-$Al_8FeMg_3Si_6$ phase transforms to $\alpha_{MG2\text{-}1}$-Al(Mn,Cr,Fe)Si phase; the total amount of the α-phase is predicted by FactSage is then 1.41%.

*Dislocation-Obstacle Interaction and Creep Activation Energy*: TEM analysis (Fig. 3.8b) indicates that the coherent Q' precipitates are cut by the dislocations and the nano-sized α-Al(Mn,Fe)Si, ~50 nm in diameter pin the dislocations in the MG1 alloy; the interparticle spacing of α ranges from 100-500 nm or an average of 300 nm (Fig. 3.8b). The main role of the rod/needle like Q' seems to be its role in nucleating the nano-sized α-Al(Mn,Fe)Si dispersoids.

Based on the TEM investigation and the high apparent activation energy that is experimentally obtained, the rate governing creep mechanism can be attributed mainly to climb over the non-coherent α-Al(Mn,Fe)Si. In our analysis, we define the apparent activation energy, $Q_a$, as comprising the activation energy for self diffusion, $q_{sd}$, and the energy change due stress, $E_s$, to cause local climb over α-Al(Mn,Fe)Si dispersoids [25].

$Q_a = q_{sd} + E_s$ where $q_{sd} = 148$ kJ mol$^{-1}$ and

$$\tau_{sd} = 0.19(Gb/L)\ \text{N m}^{-2} \rightarrow E_s = Q_a - q_{sd} = \sim 44\ \text{kJ mol}^{-1}$$

calculated with $G$ = shear modulus = 2.4x10$^{10}$ N m$^{-2}$; $b$ = magnitude of the Burgers vector = 2.9x10$^{-10}$ m; $L$ = interparticle spacing; ~3x10$^{-7}$ m, atomic weight = 27 x10$^{-3}$ kJ mol$^{-1}$ and density = 2.7 x10$^{3}$ kg m$^{-3}$. The estimated activation energy of 192 kJ mol$^{-1}$ agrees well with the experimentally determined value of 184 kJ mol$^{-1}$.

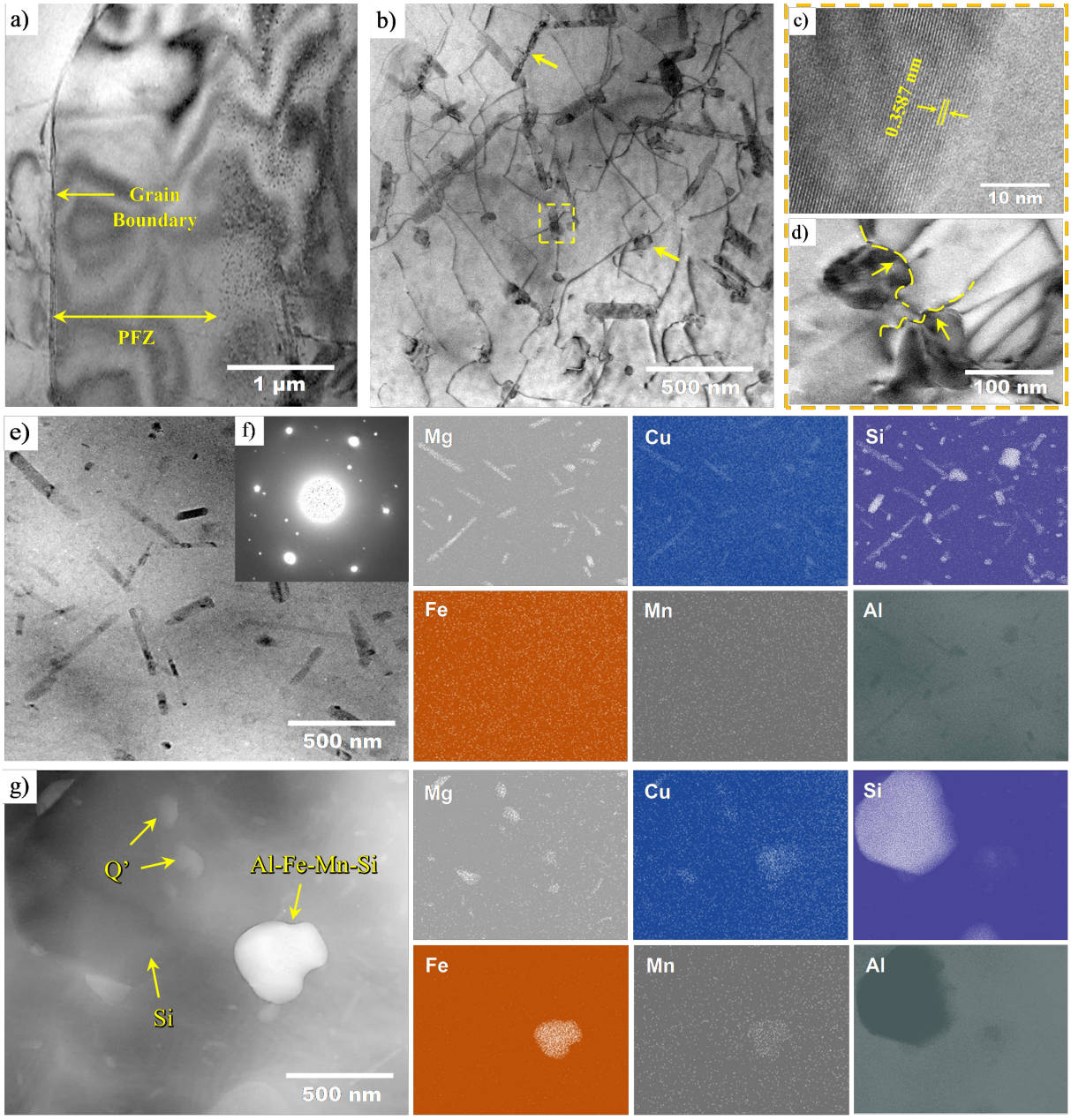

*Figure 3.8. TEM micrographs of the MG1 alloy after tensile creep at 300 °C and 28 MPa: (a) precipitate free zone (PFZ) along the grain boundary; (b) dislocation arrangements from interaction of the dislocations with the precipitates; (c) HRTEM image of an Al-Mg-Cu-Si precipitate partially coherent with the Al matrix; (d) dislocations arcing over nano-sized (~50 nm) non-coherent α-Al(Mn,Fe) dispersoids; (f) diffraction pattern indicating the reflections of α-Al matrix (large dots) and Q' precipitates (small dots); (e) Al-Mg-Cu-Si precipitates with corresponding EDS maps; g) α-Al(Mn,Fe), Si and Q' phases.*

*Investigation of the Creep Mechanism in Al-7Si-0.3Mg-0.5Cu-0.15Mn-0.25Cr-0.15Zr (MG2-1) alloy:*

The thermodynamic simulations at creep temperatures (Fig. 3.4) predict the equilibrium phases of 0.24% ε-Al-Si-Zr, 0.50% $\alpha_{MG2\text{-}1}$-Al(Mn,Cr,Fe)Si, 0.5% κ-Al-Cr-Si, 6.2% Si, 0.91% π-$Al_8FeMg_3Si_6$ and 0.43% Q-$Al_5Cu_2Mg_8Si_6$ phases. TEM images showing the microstructure of the MG2-1 alloy after tensile creep testing at 300 °C and 28 MPa are presented in Fig. 3.9. Fig. 3.9a shows a HAADF image revealing the presence of Si, Q-$Al_5Cu_2Mg_8Si_6$, $\alpha_{MG2\text{-}1}$-Al(Mn,Cr,Fe)Si, ε-Al-Si-Zr and phases; this agrees well with the thermodynamic predictions.

*Q-$Al_5Cu_2Mg_8Si_6$*: Q-$Al_5Cu_2Mg_8Si_6$ precipitates, with an average size of ~210 nm, are seen in the microstructure (Fig. 3.9a).

*ε-Al-Si-Zr*: EDS analysis reveals that ε-Al-Si-Zr particles have precipitated on the silicon phase (Fig. 3.9b).

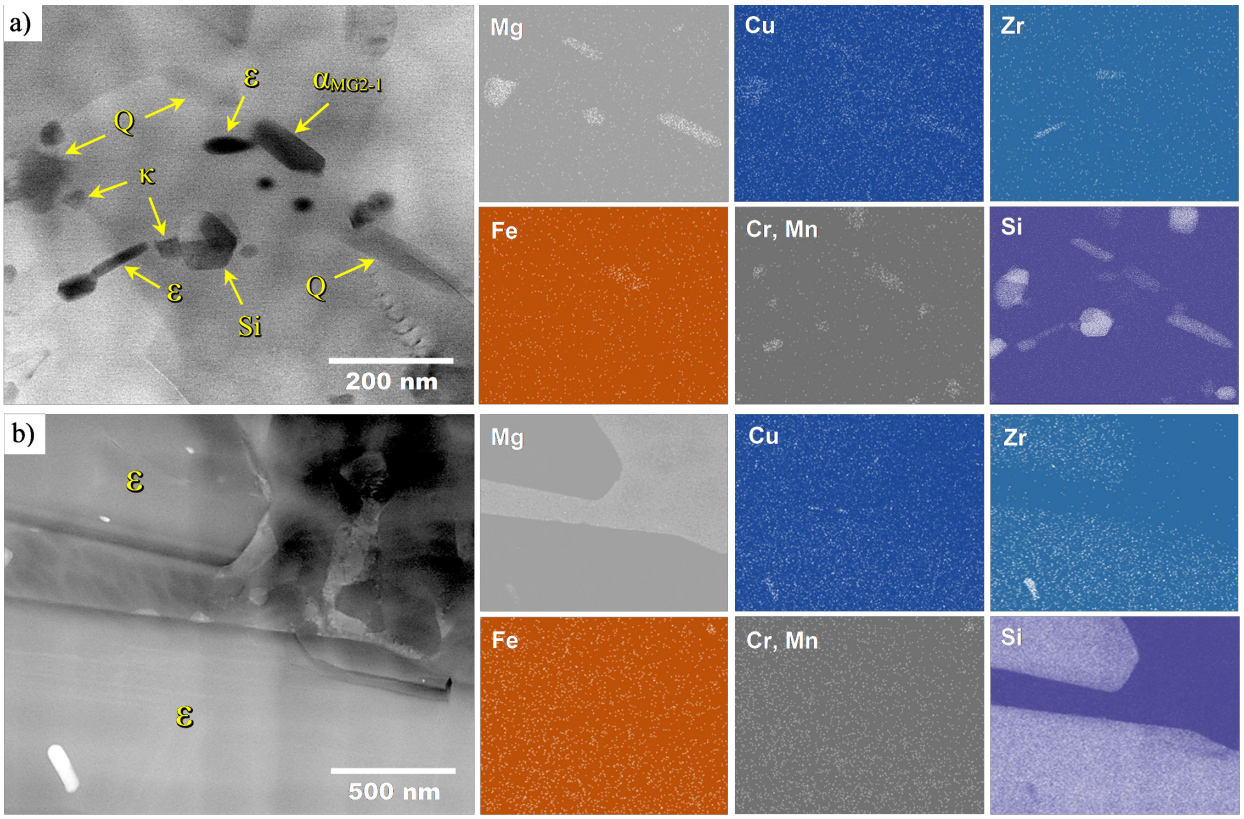


*Figure 3.9. TEM micrographs of the MG2-1 alloy after tensile creep at 300 °C and 28 MPa: (a) phase particles with corresponding EDS maps; (b) magnified image showing the ε-Al-Si-Zr particles precipitated on the silicon phase.*

*$\alpha_{MG2\text{-}1}$-Al(Mn,Cr,Fe)Si and α-Al(Mn,Cr)Si*: EDS analysis show that $\alpha_{MG2\text{-}1}$-Al(Mn,Cr,Fe)Si particles formed throughout the microstructure (Fig. 3.9a). The sizes are on the average 200 nm but can reach 500 nm. EDS maps also indicated the formation of a few α-Al(Mn,Cr)Si particles with an average size of ~ 100 nm. Figs. 3.10 a-e show HRTEM analysis α-Al(Mn,Cr,Fe)Si particles. Fig. 3.10a shows the coherency of nano-sized α-Al(Mn,Cr,Fe)Si dispersoids. The contrast lines (lattice planes) to the α-Al(Mn,Cr,Fe)Si nano-particles are continuous with the lines to the matrix; moreover, no distinct interface between the dispersoids and matrix is observed. The particle size range is 3-7 nm (average 5 nm) with an inter-planar spacing of 0.2834 nm. However,

Fig. 3.10d indicates that α-Al(Mn,Cr,Fe)Si particles lose or decrease their coherency when the particle size increases, due to an increase in the lattice misfit strain. Therefore, fine dispersoids may be coherent with the Al matrix, if they are small enough. The selected area electron diffraction (SAED) pattern in Fig. 3.10b shows that the reflections of the dispersoids (small dots) form regular patterns and distribute around the reflection of Al matrix grains (large dots). This suggests that an orientation relationship between certain dispersoids and the Al matrix can be found. Fig. 3.10d presents the HRTEM image of a partially coherent α-Al(Mn,Cr,Fe)Si interface with the Al matrix. The fringes are observed to be continuous at the interface with an inter-planar spacing of 0.4262 nm. Zenner pinning by coherent nano-sized α-Al(Mn,Cr,Fe)Si dispersoids is shown in Fig 3.10e. As can be seen, α-dispersoids interact with the grain boundary pinning them effectively. Fig. 3.10f, g show the grain size distribution in bright field and dark field TEM images. The variation in the grain size indicates that grain boundary migration and grain growth during creep process was restricted by nano-size α-Al(Mn,Cr,Fe)Si dispersoids. Reflected equiaxed grain sizes, measured from dark field mode, ranged from 200 to 700 nm.

*κ-Al-Cr-Si*: A quantification to distinguish $\alpha_{MG2\text{-}1}$-Al(Mn,Cr,Fe)Si and k-Al-Cr-Si particles was carried out by comparing the EDS mapping of Cr and Mn. The results indicated that the 98% of the particles belong to $\alpha_{MG2\text{-}1}$-Al(Mn,Cr,Fe)Si while 2% to κ-Al-Cr-Si.

*Dislocation-Obstacle Interaction and Creep Activation Energy*: The apparent creep activation energy experimentally determined for MG2-1 is 234 kJ $mol^{-1}$. Fig. 3.10c presents a TEM image showing dislocation/dispersoid interactions. Sub-grain/or grain formation is evident around a 500 nm α-Al(Mn,Cr,Fe)Si (Fig. 3.10c). Dislocation pile up is also seen at (indicated with arrows) the interface. Grain boundaries are pinned by fine α-Al(Mn,Cr,Fe)Si dispersoids while it is noted that the dislocations are not pinned by dispersoids. It seems that restoration processes (sub-grain

formation/grain nucleation) have occurred, but grain boundary migration and grain growth are impeded by Zener pinning. The activation energy for sub-grain formation is the activation energy for climb which is equal to the activation energy for self-diffusion ($q_{SD}$) of 148 kJ mol$^{-1}$ for aluminum while the subsequent grain nucleation involves grain boundary migration, the activation energy ($q_{GB}$) of which is estimated to be around 63 kJ mol$^{-1}$ for aluminum [36].

We also note that grain boundary migration has resistance from dispersoid pinning for the MG2-1 alloy. The activation energy for unpinning of the grain boundaries can be estimated after [20]: $P_z = 3F_v\gamma_{GB}/d$ where $P_z =$ Zener pressure on the boundary from pinning dislocations; $F_v =$ vol. fraction of pinning dispersoids taken as 0.0073 (calculated from 0.01 wt.% with density of alpha [37] equal to 3.59 g cm$^{-3}$); $\gamma_{GB} =$ grain boundary surface energy which is 0.324 kJ mol$^{-1}$ for aluminum [36]; and $d =$ dispersoid diameter which is 5 nm for this alloy. Using the atomic weight of aluminum of 27x10$^{-3}$ kg mol$^{-1}$ and the density of aluminum as 2.7 kg m$^{-3}$, the activation energy for Zener unpinning, $q_z$, is estimated to be ~19 kJ mol$^{-1}$. The total activation energy ($Q_a$) for the restoration process of the MG2-1 alloy during creep is then $Q_a = q_{SD} + q_{GB} + q_Z = (148 + 63 + 19) = 230$ kJ mol$^{-1}$, which agrees well with the experimentally determined activation energy of 234 kJ mol$^{-1}$.

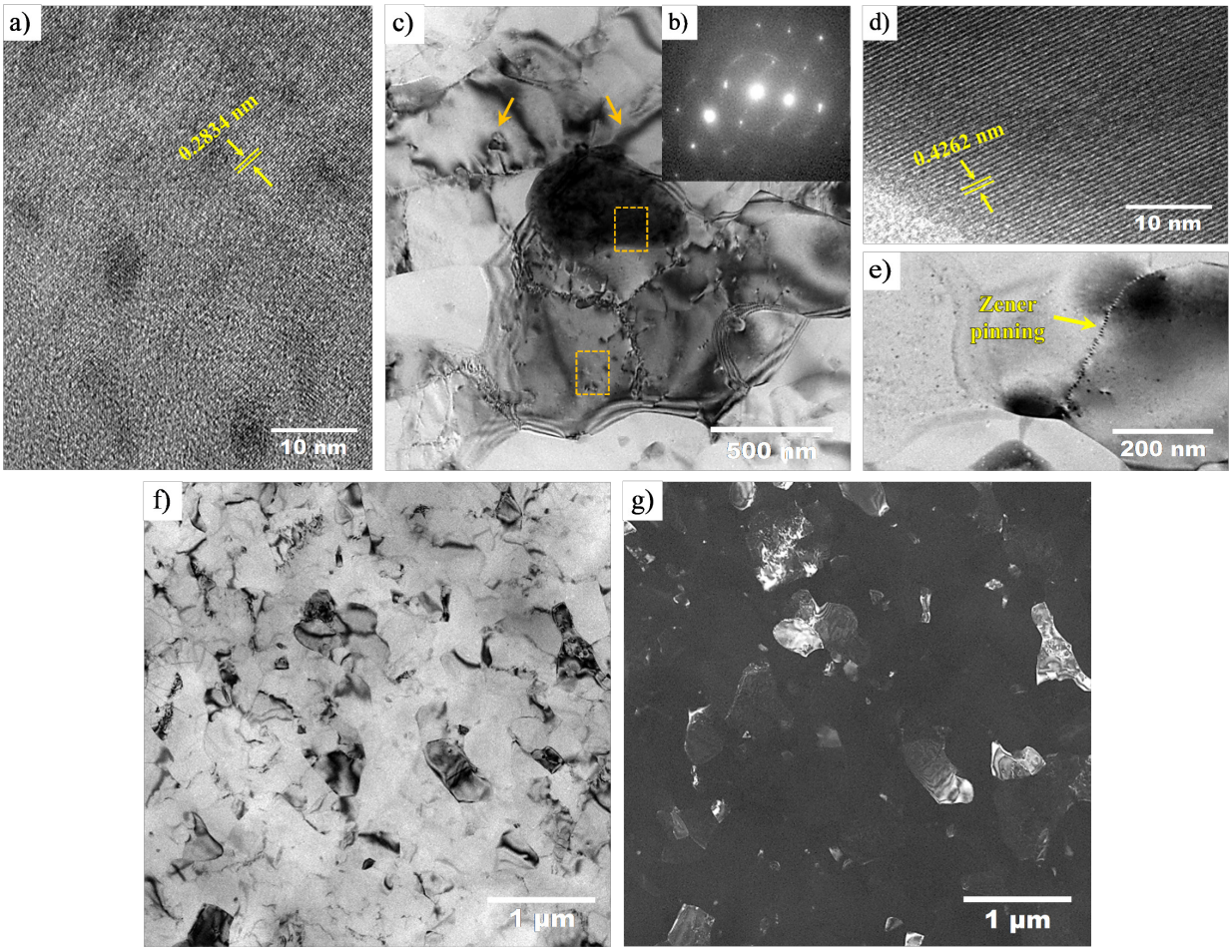


*Figure 3.10. HRTEM analysis of α-Al(Mn,Cr,Fe)Si dispersoids in MG2-1 alloy after tensile creep at 300 °C and 28 MPa: a) Coherency of the nano-scale (~6.6 nm) α-Al(Mn,Cr,Fe)Si dispersoid; b) diffraction pattern indicating the reflections of the dispersoids (small dots) and Al matrix (large dots); c) TEM image showing the dislocation-dispersoid interaction: lower and upper square show the location of Fig. a, d, respectively; d) coherency of the larger (~500 nm) α-Al(Mn,Cr,Fe)Si dispersoid; e) Zenner pinning by fine α-Al(Mn,Cr,Fe)Si dispersoids; f) bright field and g) dark field grain size distribution.*

## 3.5 Discussion

The MG1 (Al-7Si-0.3Mg-0.5Cu) alloy and the MG2-1 (Al-7Si-0.3Mg-0.5Cu-0.15Mn-0.25Cr-0.15Zr) alloy have differences in their microstructure that play key roles in their creep behavior.

*MG1 Alloy:* The T7 treatment of MG1 produces a near equilibrium semi-coherent Al-Mg-Cu-Si precipitate (called Q' in this work) which is the intermediate of the Q-$Al_5Mg_8Cu_2Si_6$ precipitate. The structural stability of Q' is related to the fact that charges of Cu, Mg and Al atoms are strongly delocalized to the Si atom suggesting a strong directional covalent bond [38]. Therefore, the presence of Q' and Q in the microstructure is related to the heat treatment process that has not fully reached the T7 condition (Fig. 3.8b). Since Q' is isostructural to Q, an increase in the aging time and temperature may result in the transformation to the incoherent phase, Q, due to the occupancy change of the atoms [39,40]. Near equilibrium lath and rod or needle-like Q precipitates of differing composition have been identified in age hardened aluminum alloys in previous studies [7,9,41]. The Q' phase has a nucleating role for nano-sized non-coherent α-Al(Mn,Fe) dispersoids which pin dislocations in the alloy (Fig. 3.8g). This nucleation effect may be attributed to the release of Si atom clusters at the locations of the dissolved metastable Q' phase and the heterogeneous nucleation of α-Al(Mn,Fe) dispersoids during homogenization process [42]. It is well expected that the Q' phase which is not completely coherent with the Al matrix would nucleate a phase also non-coherent with the Al matrix. TEM analysis of post-creep samples of the MG1 alloy of this study suggested that the creep mechanism was climb over nano-sized α-Al(Mn,Fe) dispersoids which are associated/nucleated with the Q' precipitates. It can be deduced that even if the Q' precipitates transform into the equilibrium Q precipitate and coarsen during longer creep times, their initial role in nucleating the α-Al(Mn,Fe) dispersoids is the key to the creep resistance seen in the MG1 alloy.

The activation energy for MG1 alloy experimentally determined in this study of 184 kJ $mol^{-1}$ aligns with the activation energy of 181 kJ $mol^{-1}$ for the creep of extruded Al–6Mg–2Sc–1Zr alloy in the temperature range of 150-260 °C reported by Deshmuk [27]. Their creep tests were performed under stresses of 100-140 MPa which are much higher than the stress of 28 MPa used in the present study and the temperature range is lower. They explained their results with climb of dislocations pinned with $Al_3$(Sc, Zr) precipitates which have a cubic structure with 3.8% lattice mismatch with the aluminum matrix indicating that the precipitates are coherent with some coherency strain; no dislocation detachment from particles is observed in their TEM images. The threshold stress they estimated changed with temperature and the temperature dependence could not be explained with any of the threshold-stress models. In the MG1 alloy, unlike Deshmuk [27], the pinning precipitates are non-coherent rather than coherent. Thermally activated climb over these precipitates contributes to the apparent activation energy. In the present study, the activation energy contribution of the α-Al(Mn,Fe) dispersoids to the apparent creep activation energy is determined to be 44 kJ $mol^{-1}$. Notably, Wang [43] also determined that the activation energy for hot deformation Al-Cu-Mg-Si alloys was 40 kJ $mol^{-1}$.

*MG2-1 Alloy*: The MG2-1 alloy has different phase selection at the creep temperatures when compared to the MG1 alloy. The Q phase is an equilibrium non-coherent Q-$Al_5Cu_2Mg_8Si_6$ phase rather than the semi-coherent Q' intermediate observed in the MG1 alloy. The ε-Al-Si-Zr phase has formed due to the Zr addition. The precipitation of the ε-Al-Si-Zr is due to the attractive binding energy between the Si atoms and vacancies, which create Si-vacancy clusters during homogenization/quenching and serve as nucleation sites for aging ε-Al-Si-Zr precipitates [44]. Therefore, a higher binding energy between Si-Zr (0.18 eV x $atom^{-1}$ and 0.12 eV x $vacancy^{-1}$ for Si-vacancies) [45] will cause Si atoms to bind with the Zr atoms due to a stronger attractive

interaction.

Cr addition forms a modified silicide as $\alpha_{MG2\text{-}1}$-Al(Mn,Cr,Fe)Si. Mn and Cr rich phases are reported to form in aluminum with low Fe content and high additions of Cr and Mn [28]. The Q' phase is not observed in the MG2-1 alloy acting as precipitation center for nano-sized $\alpha_{MG2\text{-}1}$-Al(Mn,Cr,Fe)Si dispersoids. Such nucleation mechanism may indicate an analogous effect to produce α-Al(MnFe)Si and α-Al(MnCrFe)Si dispersoids on dissolved β′-$Mg_2Si$ precipitates [46]. Since Q'-precipitates nucleate homogeneously and grow subsequently, a coarsening and partial dissolution is seen during continuous heating. When the Q'-reaction reaches ~400 °C (Fig. 3.4b), $\alpha_{MG2\text{-}1}$-precipitates are formed heterogeneously on the dissolving Q'-precipitates (Fig. 3.9a). At this stage, the driving force for the formation of $\alpha_{MG2\text{-}1}$-dispersoids is the supersaturation of Mn and the diffusion of Mn from the Mn-rich dispersoids to the Fe-rich primary particles. Fig. 3.9a, 3.8g also indicate that the diffusion rate of Mg and Si from Q' to the Al matrix is higher than Cu suggesting that Mg and Si atoms clusters are released and promote the nucleation of α-Al(Mn,Cr,Fe)Si dispersoids on the Q'-phase [42,47]. On the other hand, a partial dissolution of the rod shaped Q-$Al_5Cu_2Mg_8Si_6$ phase at 300 °C is observed (Fig. 3.9a). According to Farkoosh et al. [48], this behavior is associated with a decrease of the solid solubility of Q-phase on the basis of Mg content indicating that the maximum solid solubility of Mg in the Al matrix is 0.47% at 554 °C. This suggests that a full dissolution of Q-phase in the MG2-1 alloy with 0.3% Mg may occur at 350 °C. It was observed that the size range, and the variation in the coherency of the α-Al(Mn,Cr,Fe)Si dispersoids have a key role in the creep behavior of the MG2-1 alloy. The Cr modified α-phase is semi-coherent with the Al matrix unlike the non-coherent α-Al(Mn,Fe) of the MG1 alloy. However, much finer $\alpha_{MG2\text{-}1}$-Al(Mn,Cr,Fe)Si also exist in the MG2-1 in the 5 nm size range that are coherent with α-Al and are the main creep strengtheners in the MG2-1 alloy. Recent

findings reveal that α-Al(Mn,Fe) isomorphous with the α-AlFeSi are strongly correlated with the Al matrix [13,34]. The coherent nano-size dispersoids are not nucleated by the Q-phase and seem to nucleate easily in the Al-matrix (Fig. 3.10a).

The TEM investigations of the MG2-1 alloy in this study revealed that the creep deformation is due to thermally activated restoration processes. In the MG2-1 alloy, unlike the MG1, at the end of creep loading, dislocation density is low and dislocation pinning is not apparent. It can be concluded that dislocation motion is not impeded in this alloy, but the dislocations quickly accumulate at the larger α-dispersoids that then lead to sub-grain formation and the nucleation of recrystallized grains. Once restoration is underway, nano-sized (5 nm) coherent α-Al(Mn,Cr,Fe)Si dispersoids inhibit grain boundary migration and growth providing resistance to further softening imparting creep strength to the alloy; also, the fine grain size impedes further dislocation activity. This may be due to the delayed nucleation of the fine and coherent α-Al(Mn,Cr,Fe)Si. It is interesting to note that the MG2-1 alloy that shows higher creep resistance than the base alloy MG1 undergoes softening processes during creep while the MG1 alloy exhibits mainly dislocation activity.

The apparent creep activation energy determined for MG2-1 of 234 kJ $mol^{-1}$ is similar to the activation energy of ~230 kJ $mol^{-1}$ reported by Yong Li et al. [49] for the creep of Al-6092 alloy reinforced with 25% vol. of SiC particulate where the authors attributed the high activation energy to viscous glide with load transfer through the SiC phase, but they have not considered the interaction of dislocations with reinforcing particles. Their stress levels are quite low, 13-16 MPa, and the temperature range is higher (350-500 °C) than that used in the present study. The higher temperature may give rise to viscous glide.

*Table 3.8. Activation energies and creep mechanisms in MG1 and MG2-1 alloys.*

| Alloy | Activation energy (kJ mol$^{-1}$) | | Mechanism |
|---|---|---|---|
| | Experimental | Calculated | |
| MG1 (Al-7Si-0.3Mg-0.5Cu) | 184 | 192 | Local climb over dispersoids |
| MG2-1 (Al-7Si-0.3Mg-0.5Cu-0.15Mn-0.25Cr-0.15Zr) | 234 | 230 | Recovery and Zener pinning of boundary migration |

In this study, TEM analysis of creep tested samples was used to determine microstructural features that shed light into the creep mechanisms. The activation energies were then calculated based on these creep mechanisms microstructurally assessed; the calculated activation energies were found to agree very well with the experimentally determined apparent activation energies (Table 3.8).

## 3.6 Conclusions

The effect of combined additions of Cr, Zr and Mn on the microstructure and creep properties has been investigated and compared in Al-7Si-0.3Mg-0.5Cu alloys. The following conclusions can be drawn:

1. Thermodynamic calculations indicated that the MG2-1 alloy subject at 300 °C and 28 MPa consists of Q-$Al_5Cu_2Mg_8Si_6$, Si, κ-Al-Cr-Si, $\alpha_{MG2\text{-}1}$-Al(Mn,Cr,Fe)Si and ε-Al-Si-Zr phases. Calculations are in good agreement with the TEM microstructural observations.

2. MG2-1 alloy shown better creep resistance than that MG1 alloy at 300 °C, 325 °C and 350 °C due to the high density of fine and thermally stable $\alpha_{MG2\text{-}1}$-Al(Mn,Cr,Fe)Si and ε-Al-Si-Zr dispersoids.

3. $\alpha_{MG2\text{-}1}$-Al(Mn,Cr,Fe)Si dispersoids with a small particle size exhibited a low lattice strain

increasing the coherency with the Al matrix.

4. TEM-EDS analysis demonstrated that Q' phase served as nucleation site for the formation of the α-dispersoids in MG1 alloy while Q-$Al_5Cu_2Mg_8Si_6$ phase as precipitation center for nano-sized $\alpha_{MG2\text{-}1}$-Al(Mn,Cr,Fe)Si dispersoids.

5. The apparent activation energy of 234 kJ/mol and 184 kJ/mol in the MG2-1 and MG1 alloys are related to the creep deformation mechanisms of recovery and Zener pinning of boundary migration and local climb over dispersoids, respectively.

## 3.7 Acknowledgment

This research was supported by the Natural Sciences and Engineering Research Council of Canada (NSERC). The authors thank to Yizhi Wang, Mara Martinez, Parham Valipoorsalimi and Pierre Vermette for their assistance in experimental work. Raul Irving Arriaga Benitez would like to gratefully acknowledge the financial support of Gerald Hatch Fellowship (Grant No. 256938), Fonds Québécois de la Recherche sur la Nature et les Technologies – Programme de Bourses d'Excellence pour Étudiants Étrangers (FRQNT – PBEEE) (Grant No. 451069) and Consejo Nacional de Ciencia y Tecnologia – Secretaria de Energia (CONACyT – SENER) (Grant No. 451069).

## 3.8 References

[1] A. König, L. Nicoletti, D. Schröder, S. Wolff, A. Waclaw, M. Lienkamp, An overview of parameter and cost for battery electric vehicles, World Electr. Veh. J. 12 (2021) 1–29. https://doi.org/10.3390/wevj12010021.

[2] The National Research Council of the National Academies, Cost, Effectiveness, and Deployment of Fuel Economy Technologies for Light-Duty Vehicles, The National

Academies Press, 2015. https://doi.org/10.17226/21744.

[3] I.N. Fridlyander, V.G. Sister, O.E. Grushko, V.V. Berstenev, L.M. Sheveleva, L.A. Ivanova, Aluminum alloys: promising materials in the automotive industry, Met. Sci. Heat Treat. 44 (2002) 365–370. https://doi.org/10.1023/A:1021901715578.

[4] F. Feikus, Optimisation of Al-Si cast alloys for cylinder head applications, AFS Transactions 106 (1998) 1–21.

[5] L. Heysler, F. Feikus, M. Otte, Alloy and casting process optimization for engine block application, AFS Transactions 050 (2001) 1–9.

[6] M. Garat, G. Laslaz, Improved aluminium alloys for common rail diesel cylinder heads, AFS Transactions 115 (2007) 1–8.

[7] A.R. Farkoosh, M. Javidani, M. Hoseini, D. Larouche, M. Pekguleryuz, Phase formation in as-solidified and heat-treated Al-Si-Cu-Mg-Ni alloys: thermodynamic assessment and experimental investigation for alloy design, Journal of Alloys and Compounds 551 (2013) 596–606. https://doi.org/10.1016/j.jallcom.2012.10.182.

[8] E. Ozbakir, Development of aluminum alloys for diesel-engine. Master's Thesis, McGill University, 2008.

[9] A.R. Farkoosh, X. Grant Chen, M. Pekguleryuz, Dispersoid strengthening of a high temperature Al-Si-Cu-Mg alloy via Mo addition, Materials Science and Engineering: A 620 (2015) 181–189. https://doi.org/10.1016/j.msea.2014.10.004.

[10] A.R. Farkoosh, X. Grant Chen, M. Pekguleryuz, Interaction between molybdenum and manganese to form effective dispersoids in an Al-Si-Cu-Mg alloy and their influence on creep resistance, Mater. Sci. Eng. A. 627 (2015) 127–138. https://doi.org/10.1016/j.msea.2014.12.115.

[11] Z. An, W. Yang, H. Zhan, B. Hu, Q. Wang, S. Matsumura, G. Sha, On the strengthening effect of Al-Cr-Si dispersoid in an Al-Si-Mg-Cu casting alloy with Cr addition, Materials Characterization 166 (2020) 110457. https://doi.org/10.1016/j.matchar.2020.110457.

[12] H.Y. Kim, S.W. Han, H.M. Lee, The influence of Mn and Cr on the tensile properties of A356-0.20Fe alloy, Materials Letters 60 (2006) 1880–1883. https://doi.org/10.1016/j.matlet.2005.12.042.

[13] A.R. Farkoosh, Development of Creep-Resistant Al-Si Cast Alloys Strengthened with Nanoscale Dispersoids, PhD Thesis, McGill University, 2014.

[14] K.T. Park, E.J. Lavernia, F.A. Mohamed, High temperature creep of silicon carbide particulate reinforced aluminum, Acta Metallurgica Et Materialia 38 (1990) 2149–2159. https://doi.org/10.1016/0956-7151(90)90082-R.

[15] R.E. Reed-Hill, Creep, D. Van Nostrand Company, New York, 1973.

[16] M. Celikin, The creep behavior of magnesium-manganese based alloys. PhD Thesis, McGill University, 2012.

[17] M.O. Pekguleryuz, A.A. Kaya, Creep resistant magnesium alloys for powertrain applications, Advanced Engineering Materials 5 (2003) 866–878. https://doi.org/10.1002/adem.200300403.

[18] J.H. Gittus, Theoretical equation for steady-state dislocation creep effects of jog-drag and cell-formation, Philosophical Magazine 34 (1976) 401–411. https://doi.org/10.1080/14786437608222032.

[19] M.E. Kassner, Fundamentals of Creep in Metals and Alloys, Elsevier, Los Angeles, 2008.

[20] F.J. Humphreys, M.G. Ardakani, Grain boundary migration and zener pinning in particle-containing copper crystals, Acta Mater. 44 (1996) 2717–2727. https://doi.org/10.1016/1359-6454(95)00421-1.

[21] J. Lin, O.D. Sherby, Creep of oxide d strengthened materials (with special reference to T-D nichrome)., Res Mechanica: International Journal of Structural Mechanics and Materials Science 2 (1981) 251–293.

[22] K.R. Williams, B. Wilshire, On the stress- and temperature-dependenceof creep of nimonic 80a, Metal Science Journal 7 (1973) 176–179. https://doi.org/10.1179/030634573790445695.

[23] J.D. Parker, B. Wilshire, The effect of a dispersion of cobalt particles on high-temperature creep of copper, Metal Science 9 (1975) 248–252. https://doi.org/10.1179/030634575790445053.

[24] R.W. Lund, W.D. Nix, High temperature creep of Ni-20Cr-2ThO2 single crystals, Acta Metallurgica 24 (1976) 469–481. https://doi.org/10.1016/0001-6160(76)90068-7.

[25] M.E. Kassner, Creep behavior of particle-strengthened alloys, in: M.E. Kassner (Ed.), Fundamentals of Creep in Metals and Alloys, Elsevier, Massachusetts, 2015: pp. 161–180.

[26] F. Carreño, G. González-Doncel, O.A. Ruano, High temperature deformation behavior of an Al-Fe-V-Si alloy, Materials Science and Engineering: A 164 (1993) 216–219. https://doi.org/10.1016/0921-5093(93)90665-2.

[27] S.P. Deshmukh, R.S. Mishra, K.L. Kendig, Creep behavior and threshold stress of an extruded Al-6Mg-2Sc-1Zr alloy, Materials Science and Engineering A 381 (2004) 381–385. https://doi.org/10.1016/j.msea.2004.05.025.

[28] S.G. Shabestari, The effect of iron and manganese on the formation of intermetallic compounds in aluminum-silicon alloys, Materials Science and Engineering A 383 (2004) 289–298. https://doi.org/10.1016/j.msea.2004.06.022.

[29] A. Dhinakar, P.Y. Lu, N.K. Tang, J.K. Chen, Iron reduction in 356 secondary aluminum alloy by Mn and Cr addition for sediment separation, International Journal of Metalcasting 15 (2021) 182–192. https://doi.org/10.1007/s40962-020-00433-2.

[30] Y. Zhao, W. Zhang, C. Yang, D. Zhang, Z. Wang, Effect of Si on Fe-rich intermetallic formation and mechanical properties of heat-treated Al-Cu-Mn-Fe alloys, Journal of Materials Research 33 (2018). https://doi.org/10.1557/jmr.2017.441.

[31] A.M. Brown, M.F. Ashby, On the power-law creep equation, Scripta Metallurgica 14 (1980) 1297–1302. https://doi.org/10.1016/0036-9748(80)90182-9.

[32] G. Zhang, The formation mechanism of α-phase dispersoids and quantification of fatigue crack initiation by experiments and theoretical modeling in modified. Doctoral Dissertation, University of Kentucky, 2018.

[33] S.W. Han, Transformation of α-Al(Fe,Mn)Si in Al-7Si-0.4Mg cast alloys after solution heat treatment, Metals and Materials International 19 (2013). https://doi.org/10.1007/s12540-013-1001-x.

[34] Y.J. Li, A.M.F. Muggerud, A. Olsen, T. Furu, Precipitation of partially coherent α-Al(Mn,Fe)Si dispersoids and their strengthening effect in AA 3003 alloy, Acta Materialia 60 (2012) 1004–1014. https://doi.org/10.1016/j.actamat.2011.11.003.

[35] T. Gao, K. Hu, L. Wang, B. Zhang, X. Liu, Morphological evolution and strengthening behavior of α-Al(Fe,Mn)Si in Al–6Si–2Fe–xMn alloys, Results in Physics 7 (2017). https://doi.org/10.1016/j.rinp.2017.02.040.

[36] A. Rollett, G.S. Rohrer, J. Humphreys, Recrystallization and Related Annealing Phenomena, Elsevier, Amsterdam, 2017.

[37] L.F. Mondolfo, Al–Fe–Si Aluminum–Iron–Silicon system, Butterworths, 1976. https://doi.org/10.1016/b978-0-408-70932-3.50235-7.

[38] L. Ding, Z. Jia, J.F. Nie, Y. Weng, L. Cao, H. Chen, X. Wu, Q. Liu, The structural and compositional evolution of precipitates in Al-Mg-Si-Cu alloy, Acta Materialia 145 (2018) 437–450. https://doi.org/10.1016/j.actamat.2017.12.036.

[39] E. Sjölander, S. Seifeddine, The heat treatment of Al-Si-Cu-Mg casting alloys, Journal of Materials Processing Technology 210 (2010) 1249–1259. https://doi.org/10.1016/j.jmatprotec.2010.03.020.

[40] D. Apelian, S. Shivkumar, G. Sigworth, Fundamental aspects of heat treatment of cast Al-Si-Mg alloys, AFS Transactions 97 (1989) 727–742.

[41] A.R. Farkoosh, M. Pekguleryuz, The effects of manganese on the T-phase and creep resistance in Al-Si-Cu-Mg-Ni alloys, Mater. Sci. Eng. A. 582 (2013) 248–256. https://doi.org/10.1016/j.msea.2013.06.030.

[42] Z. Li, J. Qin, H. Zhang, X. Wang, B. Zhang, H. Nagaumi, Improved distribution and uniformity of α-Al(Mn,Cr)Si dispersoids in Al-Mg-Si-Cu-Mn (6xxx) alloys by two-step homogenization, Metallurgical and Materials Transactions A: Physical Metallurgy and Materials Science 52 (2021) 3204–3220. https://doi.org/10.1007/s11661-021-06243-3.

[43] X. Wang, J. Qin, H. Nagaumi, R. Wu, Q. Li, The effect of α-Al(MnCr)Si dispersoids on activation energy and workability of Al-Mg-Si-Cu Alloys during hot deformation, Advances in Materials Science and Engineering 2020 (2020). https://doi.org/10.1155/2020/3471410.

[44] S.H. Wu, H. Xue, C. Yang, P.M. Cheng, P. Zhang, J. Kuang, J.Y. Zhang, G. Liu, J. Sun, Effect of Si addition on the precipitation and mechanical/electrical properties of dilute Al–Zr-Sc alloys, Materials Science and Engineering A 812 (2021) 141150. https://doi.org/10.1016/j.msea.2021.141150.

[45] C. Booth-Morrison, Z. Mao, M. Diaz, D.C. Dunand, C. Wolverton, D.N. Seidman, Role of silicon in accelerating the nucleation of Al3(Sc,Zr) precipitates in dilute Al-Sc-Zr alloys, Acta Materialia 60 (2012) 4740–4752. https://doi.org/10.1016/j.actamat.2012.05.036.

[46] L. Lodgaard, N. Ryum, Precipitation of dispersoids containing Mn and/or Cr in Al-Mg-Si alloys, Materials Science and Engineering: A 283 (2000) 144–152. https://doi.org/10.1016/s0921-5093(00)00734-6.

[47] Z. Li, Z. Zhang, X.G. Chen, Effect of Metastable Mg2Si and Dislocations on α-Al(MnFe)Si Dispersoid Formation in Al-Mn-Mg 3xxx Alloys, Metallurgical and Materials Transactions A: Physical Metallurgy and Materials Science 49 (2018). https://doi.org/10.1007/s11661-018-4852-4.

[48] A.R. Farkoosh, M. Pekguleryuz, Enhanced mechanical properties of an Al-Si-Cu-Mg alloy at 300°C: Effects of Mg and the Q-precipitate phase, Materials Science and Engineering: A 621 (2015) 277–286. https://doi.org/10.1016/j.msea.2014.10.080.

[49] Y. Li, T.G. Langdon, A comparison of the creep properties of an Al-6092 composite and the unreinforced matrix alloy, Metallurgical and Materials Transactions A: Physical Metallurgy and Materials Science 29 (1998) 2523–2531. https://doi.org/10.1007/s11661-998-0224-9.

# CHAPTER 4: Recent Progress in Creep-Resistant Aluminum Alloys for Diesel Engine Applications: A Review

The study of Al alloys has become strategically important in heavy-duty diesel engines, supporting the global movement towards lightweighting and environmental sustainability. New research has been published during the course of this PhD including the part of this PhD research of Chapter 3. This section aims at reviewing the recent technological and scientific advancements in designing and developing creep-resistant cast aluminum alloys, considering historical studies in the alloy design and new processing technologies approaches. This chapter has been published as a journal article: R.I. Arriaga-Benitez, M. Pekguleryuz, Recent Progress in Creep-Resistant Aluminum Alloys for Diesel Engine Applications: A Review. Materials 2024, 17, 3076.

## ABSTRACT

Diesel engines in heavy-duty vehicles are predicted to maintain a stable presence in the future due to the difficulty of electrifying heavy trucks, mine equipment, and railway cars. This trend encourages the effort to develop new aluminum alloy systems with improved performance at diesel engine conditions of elevated temperature and stress combinations to reduce vehicle weight and, consequently, $CO_2$ emissions. Aluminum alloys need to provide adequate creep resistance at ~300 °C and room-temperature tensile properties better than the current commercial aluminum alloys used for powertrain applications. The studies for improving creep resistance for aluminum casting alloys indicate that their high-temperature stability depends on the formation of high-density uniform dispersoids with low solid solubility and low diffusivity in aluminum. This review summarizes three generations of diesel engine aluminum alloys and focuses on recent work on the third-generation dispersoid-strengthened alloys. Additionally, new trends in developing creep resistance through the development of alloy systems other than Al-Si-based alloys, the optimization of manufacturing processes, and the use of thermal barrier coatings and composites are discussed. New progress on concepts regarding the thermal stability of rapidly solidified and nano-structured alloys and on creep-resistant alloy design via machine learning-based algorithms is also presented.

*Keywords: Second Phase; Al alloy; Creep; Heavy Vehicle; Diesel Engine Component*

## 4.1 Introduction

The report presented in 2023 by the International Energy Agency revealed that 10 million electric passenger light-duty vehicles, including cars of different sizes, sports utility-vehicles, and light trucks, were sold in 2022, compared to only 120,000 electric heavy-duty vehicles, including electric buses and medium- and heavy-duty trucks, representing a difference of more than 8000% [1]. While electric cars are making headway in the environmental sustainability of the transport industry, the limited electrification in construction, military, agriculture, mining, and railroad sectors due to challenges in battery technology and charging infrastructure necessitates the implementation of new technologies for heavy-duty vehicles. Lightweighting of diesel engine components through aluminum (Al) substitution is positioned to offer fuel economy, better performance, and increased environmental benefits in heavy vehicles [2,3].

This review is structured into five sections. After a brief introduction in Section 1, Section 2 discusses the importance of the diesel engine for heavy vehicles and summarizes the operating conditions, failure modes, and the early development of aluminum alloys for the diesel engine (first- and second-generation alloys), and Section 3 presents a review of the third generation of alloys. Section 4 focuses on new approaches (materials and processes) that can improve the elevated-temperature performance of aluminum and enable the use of aluminum in the diesel engine. Section 5 provide a partial comparison of the experimental alloys and the future direction in aluminum research for the diesel engine.

## 4.2 Diesel Engines in Heavy Vehicles, Operating Conditions, Failure Modes, and the Early Development of Aluminum Alloys for the Diesel Engine

In terms of transportation, battery electric vehicles (BEVs) offer highly viable solutions for efficiency, reduction in greenhouse gas (GHG) emissions, and lower operating costs (because they have fewer moving parts). Despite these benefits, the limitations of battery technology, such as poor gravimetric and volumetric energy density, are the main barriers to the electrification of heavy vehicles [4]. Additionally, development in the charging infrastructure is required to scale up the adoption of heavy EVs [5]. A study on army power and energy needs through 2035 [6] indicated that all-battery electric ground combat vehicles are impractical now or in the foreseeable future because of the extensive use of batteries in tactical vehicles, limited use in a battlefield environment, long recharging times, and the need for sizeable electrical power sources. In fact, an analysis on the average global battery capacity in medium- and heavy-duty vehicles from 2019 to 2022 shows that the electric heavy-duty trucks have the largest battery capacity, with a total of 350 kWh [7]. However, this amount of energy is not enough to power heavier vehicles; for example, M109A7 Howitzer (448 kWh), Caterpillar 797F (2983 kWh), freight rail locomotive (3355 kWh), and front loaders, bulldozers, and other construction vehicles use diesel engines to carry loads of heavy materials. Therefore, for heavy vehicles, diesel engines that can generate high torque and high energy density and that have more extensive refueling infrastructure are more viable than any other type of vehicle technology (i.e., electric and gasoline).

### 4.2.1 Materials, Operating Conditions, and Failure Mechanisms in Diesel Engine Cylinder Head and Engine Block

Historically, cast iron has been used for manufacturing diesel engine components. In cylinder head and engine block production (Figure 1a, b), grey and ductile iron are typically used because of their good castability and machinability, relatively low cost, and good mechanical and thermal properties [8]. Unfortunately, these iron-carbon alloys cannot be used as a choice in vehicle weight design due to their high density. Consequently, switching from cast iron to aluminum alloys would result in very effective weight reduction (40–55%), thereby increasing the environmental benefits, improving the fuel economy, and reinforcing the vehicle performance (i.e., lowering the center of gravity of the engine in a vehicle to improve handling).

The cylinder head and engine block materials are exposed to high compression pressures and temperatures during diesel engine operation. Generally, four types of loads affect the lifetime of these diesel engine components [9]: (i) manufacturing process loads, such as residual stresses due to molding, heat treatment (due to quenching), and machining processes, (ii) assembly loads, such as bolting load and press-fits, (iii) mechanical operating load due to cylinder gas pressure, and (iv) thermal load caused by high in-cylinder gas temperatures and large variation in temperatures during operating cycles. The performance of these components, when constructed in aluminum, is limited by thermal fatigue (also called thermomechanical fatigue) and mechanical fatigue due to the engine start, operate, and stop cycles, as well as repeated combustion events [82]. The thermomechanical cyclic loadings on the cylinder head, namely, in the inter-cylinder bridge zone, are more severe than those in the engine block, as shown in Figure 4.1.

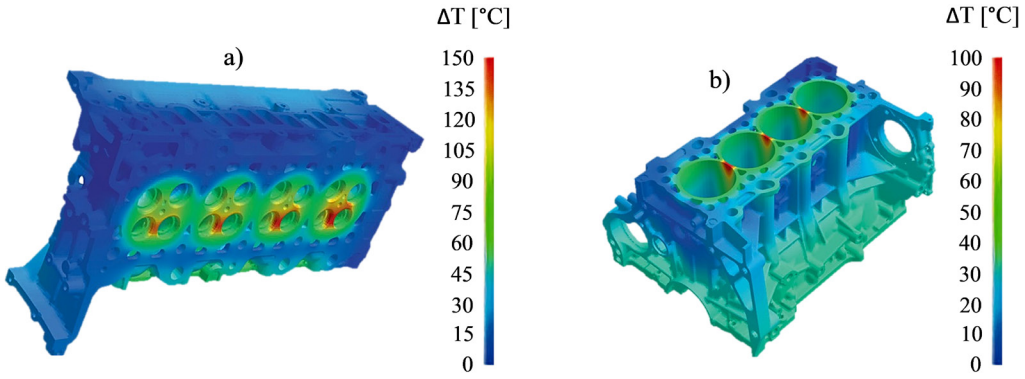


*Figure 4.1. Temperature distribution surfaces at the (a) cylinder head and (b) engine block for an engine speed of 4000 rpm. Reproduced with permission from [11]. Copyright Springer Nature, 2012.*

### 4.2.2 Mechanical Fatigue in Aluminum Cylinder Head and Engine Block

While this review is on thermal fatigue issues in the cylinder head, a short background on mechanical fatigue in the diesel engine is presented below. In the cylinder head, mechanical fatigue cracks are generated from high peak cylinder pressures or high stresses occurring mostly at the water/cooling ducts (temperature range from 120 °C to 170 °C), where high tensile residual stress occurs during the heat treatment process.

In the engine block, the maximum stress occurs at the engine-block wall and cylinder liner when the lateral force of the cylinder piston generates a maximum explosion pressure. At this point, the cracks are created and expanded under the cyclic effect of the explosion pressure at 120 °C [10]. Other factors include engine geometry, residual stresses, and casting conditions (porosity, secondary dendrite arm spacing, and inter-metallic phase morphology), which can determine the mechanical fatigue performance for both the cylinder head and engine block [12]. Additional loads

occurring during the cylinder head and engine block processing can also influence its performance, although they can be reduced or eliminated by using annealing processes [13].

### 4.2.3 Thermomechanical Fatigue in Cylinder Head and Engine Block

Thermomechanical fatigue is the most important failure in the aluminum cylinder head. A typical case of cylinder head thermomechanical fatigue is at the inter-valve bridge area, especially between the intake and exhaust valves (Figure 4.2). As depicted in Figure 4.2, the maximum heat flux in a marine diesel engine cylinder head is found in the exhaust–exhaust valve bridge due to the exposure to the high-temperature gases during combustion, and it decreases toward the outside of the combustion chamber and cylinder liner (Figure 4.2a). Similarity, the temperature distribution of the cylinder head under working conditions can reach 368 °C in the bridge area between the two exhaust valves, and it decreases from the cylinder center to the cylinder liner side due to the cooling hole of the water chamber (Figure 4.2b).

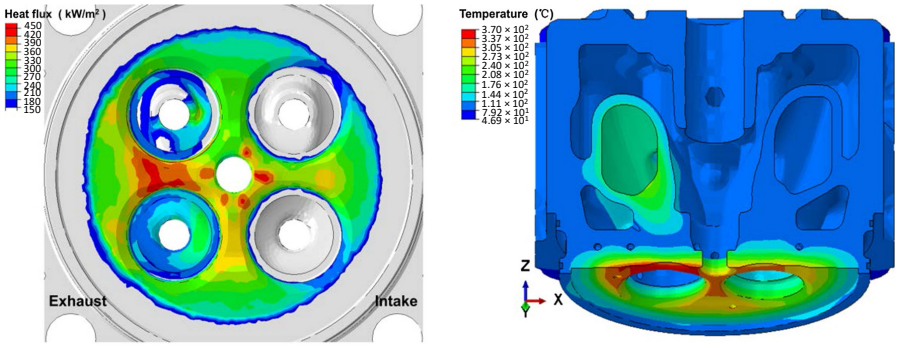


*Figure 4.2. (a) Heat flux distribution along the cylinder head fire surface and (b) temperature distribution of the cylinder head. Reproduced with permission from [14]. Copyright Springer Nature, 2021.*

The thermomechanical fatigue is due to the thermal expansion and contraction during engine operation (Figure 4.3). During engine heat-up, the inter-valve region reaches 300 °C and the metal tries to expand but is constrained due to the geometry of the region. This puts the metal under compressive loads of around 20–30 MPa. The alloy is subjected to creep deformation due to loading at elevated temperatures. At engine cooldown, the metal tries to contract from its state at elevated temperature, but it is constrained and is placed under tensile loads, leading to tensile deformation, causing the greatest contribution to fatigue at this critical region. The repetition of expansion and contraction cycles identified during engine heat-up and cooldown result in local tensile stresses, causing fatigue cracks that can be nucleated during the engine cooldown period if the initial creep deformation is high and the material does not have sufficient ductility to accommodate these stresses by local plastic deformations. Even when the material is ductile, the repetition of these alternating compressive and tensile stresses can cause crack initiation due to plastic damage accumulation and eventually lead to failure in diesel engines.

Zhang et al. [15] simulated a thermal cycling test of a marine engine cylinder head to evaluate the stress under start–stop cycle conditions. Figure 4.3 shows the stress distribution of the first cycle. In the heating stage, the local stress concentrates on the exhaust nose bridge area, but at the maximum temperature, a decrease in the stress is seen due to stress relaxation. This stress change is attributed to the material exhibiting cyclic softening with higher temperatures [16]. In the cooling stage, the stress reaches the maximum value, and decreases as time goes on. Consequently, the failure mode of inelastic deformation during the thermal cycle is reproduced by thermal-gradient-cycle-induced structural constraints.

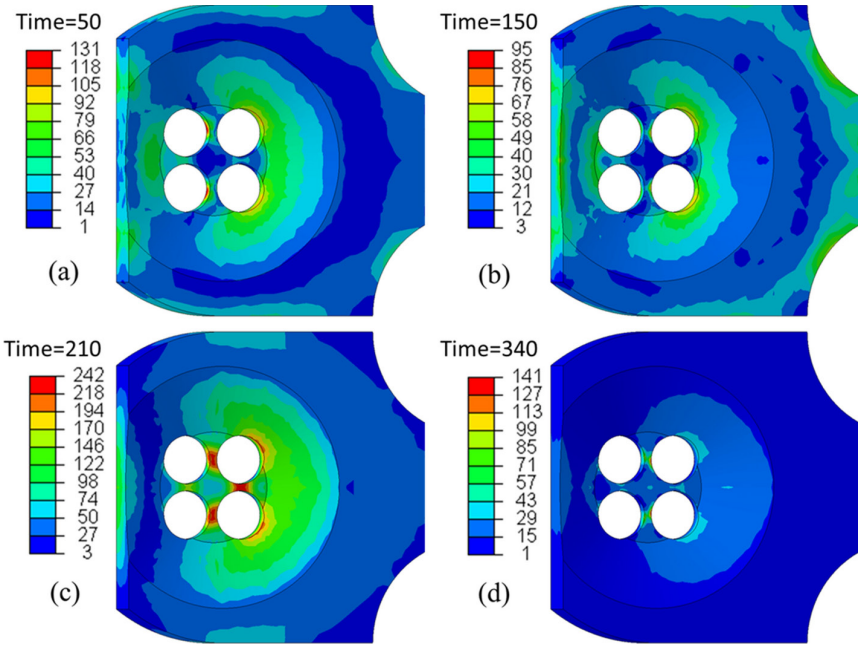


*Figure 4.3. Stress distribution at the typical time during thermal cycling: (a) 50 s heating, (b) 150 s heating, (c) 210 s cooling, and (d) 340 s cooling. Reproduced with permission from [15]. Copyright Springer Nature, 2022.*

There is no material property that can properly assess the response of the inter-valve region to thermal cycles and stresses during diesel engine operation. Thermal fatigue evaluates the response of the material during thermal cycling when the specimen is totally free to expand or contract so that only mechanical strains resulting from the thermal gradients are experienced by the specimen [17]. Instead, the resistance to the specific type of thermal fatigue experienced by the geometrically constrained inter-valve can be assessed based on two properties of the material: (1) tensile performance at engine cooldown (at room temperature) and (2) creep resistance at engine heat-up (300 °C and 22–30 MPa). For tensile performance, there are two schools of thought that place more importance on either ductility or tensile strength, which depends on whether it is preferable for the material to accommodate the tensile stresses either elastically or plastically during engine

cooldown. Therefore, the material property requirements, such as creep resistance at 300 °C to resist creep deformation in the inter-valve regions during engine heat-up, ductility to accommodate and avoid catastrophic failure, and strength to accommodate the tensile stresses elastically when ductility is low, have been the main objectives during the development of diesel engine components based on Al alloys.

### 4.2.4 The Early Use of Aluminum in the Diesel Engine: First- and Second-Generation Alloys

Over the years, different generations of aluminum diesel engine alloys have been investigated to provide adequate strength and creep resistance under diesel engine operating conditions. A review of first- and second-generation aluminum alloys for use in the diesel engine was conducted by Pekguleryuz et al. [18]. A summary and the principles discovered are provided here.

The first-generation alloys were developed to achieve improved creep resistance as modifications of the commercial aluminum alloys A356 (Al-7Si-0.3Mg-0.2Fe) or the A319 (Al-6Si-3.5Cu-1Fe) used in gasoline engine vehicles. The researchers who valued increasing strength over ductility used modified A319, and those who preferred to maintain ductility used A356 as the base alloy. These alloys are based on the Al-Si system with β′-$Mg_2Si$, λ-Al-Mg-Si-Cu, or the θ-$Al_2Cu$, Q-Mg-Si-Cu precipitation sequence depending on the Mg and Cu levels, with the second sequence providing higher strength. In the T6 condition, they possess metastable phases that transform and coarsen under diesel engine service temperatures, leaving only the Q precipitate for strengthening. Aluminum alloy development activities for diesel engines began in 1998 by VAW. These activities focused on adding 0.5–1% copper to the commercial Al-Si casting alloys (319, 356, 380, and 390) to increase strength and creep resistance for use in cylinder head applications [13,19]. Among the

alloys optimized, the A356 (Al-Si-Mg) alloy showed the most promising results. Studies indicated that after T6 treatment (solutionizing for 5 h at 525 °C, followed by water quenching and annealing for 4 h at 165 °C), there was no improvement in yield stress or hardness at ambient temperature. However, a significant improvement in yield stress and creep resistance was observed at service temperatures above 150 °C. This behavior was associated with the formation of Cu-precipitates after the T6 heat treatment [18,20,21], but a loss of strength was seen at 300 °C due to the coarsening of the precipitates.

The second generation emerged from the addition of nickel to the A356 + 0.5% Cu alloy for engine block applications, because they require higher strength than the cylinder head [22,23]. The Al-7Si-0.4Mg-0.4Cu-0.3-Mn-0.5Ni-0.4Fe alloy in the T6 condition exhibited creep resistance at 120 MPa and 200 °C, because the time to reach from 0.2 and 0.5% strains was longer than the commercial alloys. In addition to the improvement in creep resistance of 500 h at 250 °C, the fatigue strength also increased by 20%, and tensile strength showed an improvement. This phenomenon was attributed to the formation of Ni-bearing inter-metallics. However, the alloy presented low ductility due to the brittleness of the Ni-bearing inter-metallics.

Some of the points obtained from the studies of the first and second generation of aluminum diesel engine alloys can be summarized as follows:

1 Since peak age T6 is not sustainable in Al alloys for diesel cylinder heads (e.g., time at 300 C), the nature of the equilibrium precipitate determines the strengthening effect [20]. The strength of the diesel engine alloy needs to be designed on the over-aged/equilibrium-state microstructure, and the tensile properties need to be evaluated after long presoaking at temperature.

2 In the Al-Si-Mg-Cu system, the equilibrium precipitates can vary depending on the Si/Mg ratio and Cu level [18]. This quaternary alloy composition can be adjusted to yield (Q, Si, θ) or (Q, β, Si) equilibrium phases [18]. While the mix of equilibrium precipitates is well known in wrought Al alloys with low Si levels, the precipitate mix versus composition in experimental casting alloys with higher Si is not well documented. The authors suggest that the precipitates in these experimental alloys can be predicted/determined via thermodynamic calculations, scanning calorimetry (DSC) validations, and high-resolution transmission electron microscopy (HRTEM). These can be viable research directions in future studies.

3 Nickel additions to the Al-Si-Mg-Cu alloy usually led to low ductility due to the existence of the brittle T-phase [22,23], which can lead to early failures in tensile or creep testing.

## 4.3 Review of the Third Generation of Aluminum Diesel Engine Alloys

The development of the third generation of aluminum diesel engine alloys focused on improving the most important performance requirements of creep resistance at 300 °C to resist the deformation in the inter-valve area [18,24]. The alloys were designed to form a high-volume fraction of thermally stable dispersoids with the addition of peritectic elements to Al-Si-Mg-Cu alloy compositions.

### 4.3.1 Early Work on Third-Generation Aluminum Alloys for the Diesel Engine

In 2008, Prof. Pekguleryuz's team at McGill, in collaboration with Rio Tinto (London, UK) (then Alcan Aluminum, Montreal, QC, Canada), developed a creep-resistant aluminum alloy from the combined addition of peritectic elements (Cr, Zr, Ti, and Mn) to the A356 + Cu alloy [18,25]. The alloy (MG2) showed better compressive creep resistance by reaching only a creep strain of 4.9%

after 300 h at 300 °C. The improvement in the MG2 alloy was up to three times better than the R1 (A356), R2 (A356 + 0.5% Cu), and the MG1 (A356 + 0.15% Mn +0.15% Cr +0.15% Zr) alloys (Figure 4.4a). Microstructural analysis in the MG2 alloy revealed that the Zr-Si-Al ternary phase, a complex Cr phase (Al-Cr-Mn-Fe-Si), and Zr submicron phases in the grain interior were responsible for enhancing the creep resistance (Figure 4.4b).

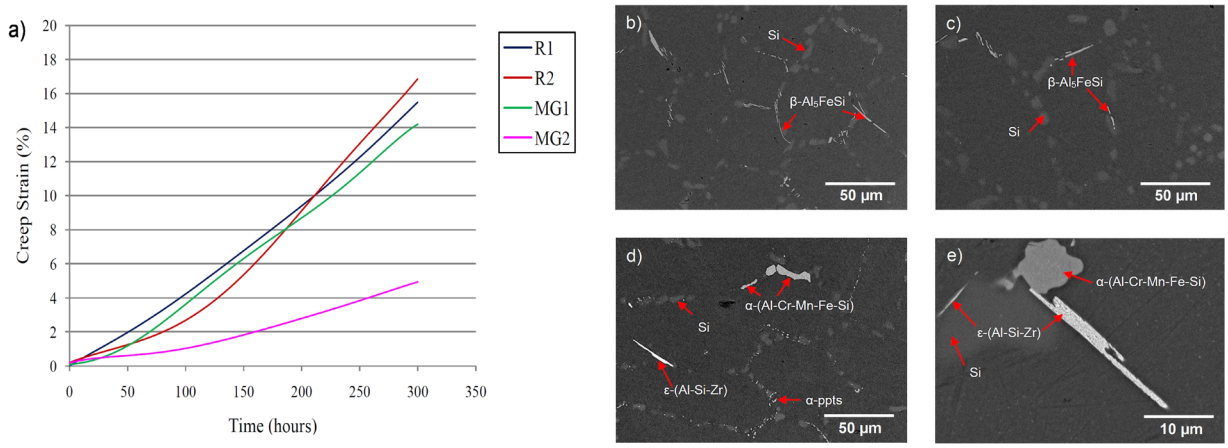


*Figure 4.4. (a) Compressive creep curves at 300 °C under 30 MPa and SEM micrographs of the (b) R1, (c) R2, (d) MG1, and (e) MG2 alloys in the over-aged condition [26].*

In 2015, Farkoosh and Pekguleryuz [27] demonstrated that molybdenum (Mo) in combination with manganese (Mn) formed a large volume fraction of dispersoids that resulted in the development of highly creep-resistant Al-Si-Cu-Mg-Mo-Mn alloys. Mn was of interest because of its low diffusivity and relatively high solid solubility in the Al matrix. Creep testing results on the Al-7Si-0.5Cu-0.3Mg-0.1Fe-0.3Mo-(0-1.0) Mn alloy at 300 °C and 30 MPa indicated that creep time-to-fracture (Figure 4.5a) increased from ~25 to ~180 h as Mn increased from 0.0 to 0.5. However, at 1% Mn, creep time-to-fracture dramatically decreased to 130 h. Microstructural observations associated the increase in creep resistance with the increase in the precipitation density of α-

Al(Fe,Mn,Mo)Si dispersoids (from ~0.6 to ~4 $\mu m^{-2}$), reducing the dispersoid-free zone (DFZ; Figure 5d). This pattern resulted from the Mn supersaturation and Mo segregation in the intra-dendritic and inter-dendritic regions, respectively, improving the creep resistance in the Al-7Si-0.5Cu-0.3Mg-0.1Fe-0.3Mo-0.5Mn (MG3RM50Mn) alloy system. It was suggested that Mn, a peritectic element, enriches in the α-Al dendrite cores (as a solid solution) and diffuses slowly, forming the α-Al(Fe,Mn,Mo)Si dispersoids and coarsening slowly, maintaining thermal stability. The decrease in creep resistance at 1 wt% Mn was due to the increased amount of the inter-metallics, which embrittled the alloy. As a result, the dislocation pile-up at the inter-metallic/matrix interface can generate sufficiently high stresses that can cause fracture.

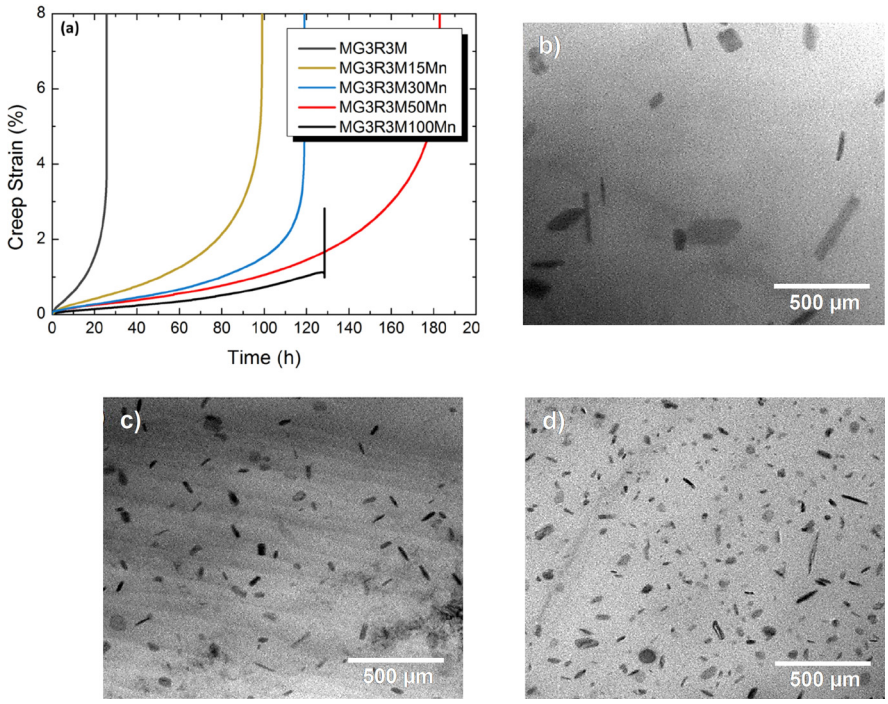


*Figure 4.5. (a) Tensile creep deformation vs. time at 30 MPa and 300 °C. TEM micrographs showing the distribution of α-Al(Fe,Mo,Mn)Si dispersoids in (b) Al-7Si-0.5Cu-0.3Mg-0.1Fe-0.3Mo, (c) Al-7Si-0.5Cu-0.3Mg-0.1Fe-0.3Mo-15Mn, and (d) Al-7Si-0.5Cu-0.3Mg-0.1Fe-0.3Mo-0.5Mn at 540 °C after 600 min. Reproduced with permission from [27]. Copyright Elsevier, 2015.*

In 2020, Rashno et al. [28] compared the creep behavior of the cast A356 alloy with combined and singular additions of Zr and Er and obtained improved creep resistance due to an increase in the amount of Zr- and Er-rich inter-metallics, characterized by their various shapes and sizes. Fe-rich inter-metallics did not form because Fe atoms were replaced by Zr and Er atoms. As a result, the modified alloy exhibited uniform elongation. Microstructural features also showed that the formation of fine dendritic α-Al and fibrous and partially rounded eutectic Si improved the creep resistance, restricting the mean free path for dislocation motion. Researchers indicated that lattice self-diffusion, climb-controlled creep is the dominant creep mechanism in the 493–553 °K temperature and 480–730 MPa stress regimes, with an average activation energy between 121.6 and 148.2 kJ $mol^{-1}$. These stresses are too high for A356, and the mechanisms would be related to plastic deformation rather than to creep.

De Luca et al. [29] investigated the creep resistance at 300 °C and 400 °C under stress ranges of 10 and 70 MPa and 5 and 30 MPa, respectively, using Mn and Mo additions in the Al-Zr-Sc-Er-Si-based alloy. The Al-0.08Zr-0.02Sc-0.01Er-0.10Si-0.25Mn-0.11Mo subjected to compressive creep in the aged condition indicated no degradation in the creep resistance at both testing temperatures. The researchers associated this behavior with the solid-solution strengthening and the formation of thermally stable α-Al(Mn,Mo)Si submicron precipitates (on the grain boundaries) and $Al_3(Zr,Sc,Er)(L1_2)$-nanoprecipitates (at the grain boundaries). Additional results revealed that the formation of fine equiaxed grains in the modified alloy (0.35 mm) and elongated grains (0.6 mm) in the base alloy, with inter-precipitate distances from ~10 μm to >100 μm, influenced the creep resistance. The deformation mechanisms were identified as diffusional creep at 400 °C for both alloys, and as dislocation glide for the modified alloy and dislocation climb for the base alloy

at 300 °C. However, better creep resistance was obtained in the modified alloy due to the presence of α-Al(Mn,Mo)Si-precipitates that provided GB strengthening.

Certain findings of the early work on the third generation of aluminum alloys are worth summarizing:

1. Formation of submicron precipitates: Zr addition forms submicron precipitates (ternary Al-Si-Zr) in Al-Si-Mg-Cu casting alloys, which enhance creep resistance [18]. Zr, Sc, and Er also form $Al_3(Zr,Sc,Er)(L1_2)$-nanoprecipitates in aluminum [29], which improve creep resistance.

2. Modification of the Al-Mn-Fe-Si dispersoids for ductility: Cr addition [18] and Zr and Er, added singly or in combination [28], modify the Al-Fe-Si into Al-Cr-Mn-Fe-Si dispersoids and seem to have a role in improving ductility.

3. Thermally stable Al-Mn-Fe-Si dispersoids for creep resistance: Mn (<1 wt%) and Mo added in combination modify and improve the thermal stability of the Al-Fe-Si dispersoids, forming α-Al(Fe,Mn,Mo)Si dispersoids that improve creep resistance.

The exact role of the dispersoids/precipitates in creep behavior, e.g., the interaction of precipitates with dislocations, sub-grain and grain boundaries, and the evolution of the microstructure with time, was not clarified in these early studies with microstructural investigation.

### 4.3.2 Recent Studies on the Third-Generation Aluminum Alloys

Recent work on Al-Si-Mg-Cu alloys in 2023 focused mainly on identifying the creep mechanisms and the role of dispersoids in creep resistance. It was noted that the dispersoids impeded dislocation climb and/or restoration processes of sub-grain formation and sub-grain migration.

Li et al. [30] carried out compressive creep tests at 300 °C and 50 MPa for 100 h after T7 heat treatment in 356 alloy with individual and combined additions of V, Zr, and Mo. The study showed that the minimum creep rate decreased 67% and 50% for the alloys containing V and V-Zr-Mo, respectively, when they were compared with the base A356 alloy. The decrease was associated with the formation of large grain sizes, lower fraction of DFZ, and more rounded dispersoids. They also reported that the A356 alloy with V, Zr, and Mo addition exhibited the highest strengthening effect at 300 °C, with a 22% improvement compared with the A356 alloy due to a high-volume fraction of thermally stable $(Al,Si)_3(Ti,V,Zr)$ and α -Al(Mn,Mo,V,Fe)Si dispersoids. The stress used was, however, higher than that observed during diesel engine operation.

Qian et al. [31] studied a strengthening method based on multi-element additions and on the correlation between creep resistance and microstructure in the AA6111 (Al-0.95Mg-1.0Si-0.8Cu-0.1Mn-0.15Fe-0.1Cr-0.1Zn-0.08Ti) alloy strengthened by synergistic Er and Zr addition. The results showed better creep resistance in the Er- and Zr-containing alloy (165 kJ/mol) than in the alloy containing only Er (160 kJ/mol). Microstructural investigation related this improvement with the formation and refinement of the coarse $Al_3Er$ inter-metallics to $Al_3(Er, Zr)$ nanoprecipitates, which were characterized by their thermal stability (29 and 34 nm before and after creep, respectively) and produced through the combination of a Zr-enriched outer shell and an Er-enriched inner core. The $Al_3(Er, Zr)$ particles prevented grain boundary migration and the movement of the dislocation rate during creep deformation. They claimed dislocation climb to be the main creep deformation rate-controlling mechanism in both alloy systems. Alloy 6111, however, is a wrought alloy, and the principles need to be further developed for cast alloy compositions. Selective reinforcement of sections of the cylinder head via a wrought alloy is also a possibility that can be investigated.

Arriaga-Benitez and Pekguleryuz [32] carried out a systematic study on the creep behavior of Al-Si-Mg-Cu (Mn, Cr, Zr) alloys. Considering that threshold stress analysis does not reveal the creep micro-mechanisms and the specific role of the dispersoids in softening processes, the authors utilized in-depth electron microscopy analyses of creep-tested samples to theoretically assess the activation energy for creep and compare it to experimentally determined activation energies. The modified Al-7Si-0.3Mg-0.5Cu-0.15Mn-0.25Cr-015Zr (MG2-1) alloy activation energy of 234 kJ $mol^{-1}$ indicated a higher apparent activation energy ($Q_a$) of 50 kJ $mol^{-1}$ than the base alloy Al-7Si-0.3Mg-0.5Cu (MG1) after the tensile creep tests at 300–350 °C and 28 MPa in the T7 condition, suggesting better creep resistance (Figure 6a). TEM microstructural observations in the base alloy showed that Q' precipitates are cut by the dislocations and the nano-sized α-Al(Mn,Fe)Si, ~50 nm in diameter, pin the dislocations. Based on the TEM investigation and the apparent activation energy, the researchers attributed the creep-rate-governing mechanism to climb over non-coherent α-Al(Mn,Fe)Si (Figure 6b). On the other hand, the modified alloy presented dislocation/dispersoid interactions and sub-grain formation, wherein the creep mechanism was identified as sub-grain boundary migration with Zener pinning by coherent and ~5 nm $\alpha_{MG2\text{-}1}$-Al(Mn,Cr,Fe)Si dispersoids (Figure 4.6c). The theoretical assessment used in this research to determine the creep mechanisms was found to agree very well with the experimental results.

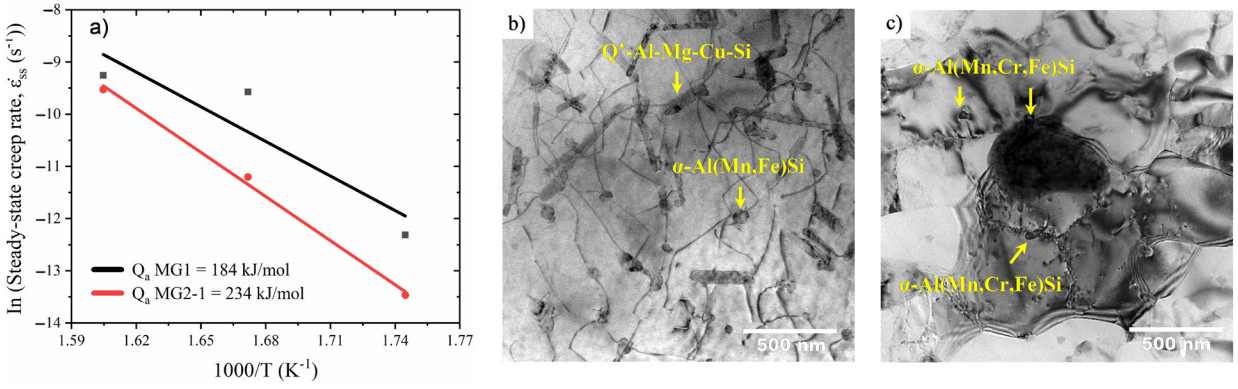

*Figure 4.6. (a) Arrhenius plot of log of steady-state creep rate vs. the reciprocal of temperature at 28 MPa, (b) dislocation arrangements from interaction of the dislocations with α-Al(Mn,Fe)Si and Q'-Al-Mg-Cu-Si particles, and (c) interaction of $\alpha_{MG2\text{-}1}$-Al(Mn,Cr,Fe)Si particles with dislocations and sub-grain boundaries. Reproduced with permission from [32]. Copyright Elsevier, 2023.*

Some of the important findings of the recent work on the third generation of aluminum alloys can be summarized as follows:

1. Modification of the Al-Mn-Fe-Si dispersoids: V-Zr-Mo addition to A356 created a high-volume fraction of thermally stable (Al,Si)3(Ti,V,Zr) and α-Al(Mn,Mo,V,Fe)Si dispersoids that decreased the creep rate by 50% [30].

2. Formation of submicron precipitates: Er and Zr addition to wrought alloy 6111 generated $Al_3$(Er,Zr) nanoprecipitates (~30 nm) that prevented grain boundary migration and dislocation motion during creep. A very important discovery was the chemical inhomogeneity of the precipitates with a Zr-enriched outer shell and an Er-enriched inner core [31].

3. The role of Cr-modified Al(Mn,Cr,Fe)Si dispersoids in creep resistance was determined. Coherent ~5 nm dispersoids produced Zener pinning of sub-grain boundaries, slowing softening processes during creep [32].

The remaining issues are still related to determining the exact creep-strengthening mechanisms in the alloys, comparison of alloys (creep rates) under identical creep conditions (of the diesel engine), and the optimization of the alloys for castability and manufacturability.

## 4.4 New Approaches Enabling the Elevated-Temperature Use of Aluminum

The first three generations of alloys for diesel engine applications were based on Al-Si-Mg-Cu systems with varying Cu or Mg content or with Ni or transition/peritectic element additions. Recent work on developing aluminum for elevated-temperature applications investigated different alloy systems (mostly Al-Cu alloys) and nanostructured and/or Al composites. The use of coatings, optimization of the fabrication process, and the development of statistical algorithms are also studies that can be enablers of aluminum use for the diesel engine. These material advances may promote creep strength by introducing grain boundary reinforcement, reduction of the processing defects, and optimizing processing techniques (e.g., heat treatment). Their use in the diesel engine is not straightforward, but these studies can pave the path to the development of new diesel engine aluminum materials and processes.

### 4.4.1 Al-Cu-Based Alloys

Al-Cu-based alloys have lower castability than Al-Si-based alloys, but can achieve higher strengths, especially through age hardening with the θ-$Al_2Cu$ precipitation. Al-Si casting alloys have over the years replaced Al-Cu alloys due to improved fluidity and castability imparted by the Si addition. Studies on Al-Cu alloys have been carried out since 2017 on the elevated-temperature strength and creep resistance of these alloy systems; however, the studies did not consider castability in conventional casting techniques.

Awe et al. [33] developed a high-temperature Al-27Cu-5Si cast alloy with 0–1.5 wt% additions of Ni through the high-cooling-rate casting technique. Tensile tests performed at 300 °C revealed that

yield strength and ultimate tensile strength increased from 96 MPa to 267 MPa and from 208 MPa to 272 MPa, respectively, with increasing Ni content, but elongation decreased from 12.3% to 4%. On the other hand, yield strength and ultimate tensile strength at 400 °C for the 1.5% Ni alloy decreased by 70% and 62%, respectively, but the elongation increased from 4% to 7%. Thermodynamic calculations and SEM-EDS analysis concluded that the enhanced tensile properties at elevated temperatures in the Ni-containing alloys are attributed to a change in the solidification profile in the base alloy by Ni. A thermally stable Ni-rich phase ($Al_7Cu_4Ni$) is produced that forms ahead of the eutectic front at a temperature greater than the eutectic temperature. Due to the high Cu content, its castability and microstructural refinement required rapid solidification, and Ni together with Cu seems to have created ductility problems.

Gao et al. [34] studied the co-stabilization of θ′-$Al_2Cu$ and $Al_3Sc$ precipitates in Al-1.08 at.%Cu alloys, including 0.18 at.%Sc, 0.18 at.%Sc with 0.05 at.%Si, and 0.18 at.%Sc with 0.05 at.%Zr additions after thermal exposure at 300 °C on artificial aged samples. The results showed that Sc-Si and Sc-Zr microalloying enhanced the thermal stability of θ′-$Al_2Cu$ precipitates. However, an increase in the Si addition accelerated the growth of $Al_3Sc$ particles, leading to limited optimization on high-temperature resistance. Therefore, the combined Sc-Zr microalloying showed the most desirable effect on the thermal stabilization of the dual precipitates at 300 °C. Experimental evidence of atom probe tomography associated the θ′-$Al_2Cu$ thermal stabilization with a reduction in interfacial energy caused by solute segregation at the θ′-$Al_2Cu$/matrix interface. Similarly, $Al_3Sc$ thermal stabilization was related to the formation of a Zr-rich outer shell that encapsulated the inner Sc-rich core and served as a diffusion barrier to limit the solute exchange across the $Al_3Sc$-based particles and to restrain their growth during thermal exposure at 300 °C. The idea of surface

segregation in dispersoids and precipitates seems to open an interesting future direction in dispersoid strengthening of aluminum alloys.

Li et al. [35] performed compressive creep deformation tests at 300 °C for 100 h and 50 MPa on Al-Cu 224 cast alloys with micro-level transition metals (TMs) of Zr, V, and Sc to evaluate the thermal stability of θ″/θ′-$Al_2Cu$ precipitates and $L1_2$-$Al_3M$ dispersoids. Creep resistance under the T7A condition indicated that the minimum creep rate with Sc and Zr additions obtained the lowest value of $2.8 \times 10^{-9}$ $s^{-1}$ when compared with the other alloys, wherein the base alloy obtained the highest minimum creep value of $2.0 \times 10^{-7}$ $s^{-1}$. Microstructural investigation indicated that this behavior is due to the presence of a high amount of $Al_3$(Sc, Zr) dispersoids in combination with finer θ′ precipitates that inhibited dislocation movement, resulting in a small creep strain (0.007 after 100 h). Researchers associated the low degree of coarsening of θ′-$Al_2Cu$ with the segregation of TMs at the θ′ interface, reducing its interfacial energy and acting as a diffusion barrier for Cu atoms. Similar to the study of Gao et al. [34], this study [35] also underlines the importance of surface segregation in precipitates and can be an important design tool for second-phase strengthening, as well as for aging heat treatment.

Bahl et al. [36] evaluated the effect of θ-$Al_2Cu$ precipitates at the grain boundaries on Al-Cu-Mn-Zr (ACMZ) alloys with 6 wt% Cu and 9 wt% Cu, with tensile and compressive creep tests performed at 300 °C. Microstructural analysis showed that θ-precipitates increased their volume fraction from ~0.7% in 6Cu to ~6% in 9Cu at the grain boundaries. However, tensile creep indicated that the alloy with 9Cu failed in creep faster than 6Cu at stresses above 20 MPa, while deformation rates in the stress range of 115–110 MPa were not affected in compressive creep. Microstructures after creep testing related this behavior with a higher formation of cavities on

grain boundaries promoted by large-sized intergranular θ-precipitates in 9Cu during tensile creep. This study, however, used stress levels higher than the service stresses of the diesel engine.

These recent studies on the Al-Cu system reveal that the Al-Cu-Ni system highlights the need for the addition of low-level elements to improve ductility and the thermal stability of the aging precipitates or to create thermally stable precipitates. The combined addition of Zr and Sc, and especially the presence of Zr, emerge as important alloy design tools for the future development of the Al-Cu system for elevated-temperature use.

### 4.4.2 Al Matrix Composites

Aluminum-based matrix composites (AMCs) combine an Al matrix with rein-forcing phases (borides, carbides, oxides, nitrides, and their combinations) in the form of particles, whiskers, or fibers, leading to the development of lightweight and heat-resistant diesel engine components [37–39]. Some recent studies on this subject are presented below.

Ji et al. [40] evaluated the creep performance on Al-12Si alloy reinforced with borate whiskers ($Al_{18}B_4O_{33}$) and unreinforced Al-12Si alloy at 250–400 °C and 50–230 MPa. Creep resistance in the reinforced alloy was improved by three orders of magnitude, compared with the unreinforced alloy. TEM microstructural investigations after the creep test indicated that the dislocations accumulated near the reinforced whiskers, which restricted their motion; in addition, the whiskers hindered the grain growth, leading to a more refined structure. However, due to the strain mismatch between the whiskers and the Al matrix, a stress concentration zone was formed around the whisker, causing its fracture. The creep fracture surfaces at 300, 350, and 400 °C showed that the fracture mechanism was related to reinforced whiskers, interfacial debonding between the whisker and matrix, and interfacial debonding and whisker fracture, respectively.

Zhao et al. [41] studied the creep behavior of the in situ ($ZrB_2$ + $Al_2O_3$)/AA6016 composites prepared by the electromagnetic induction heating furnace. The AMCs in the T6 condition (545 °C for 2 h and 180 °C for 3 h) tested at 300 °C and 70 MPa showed creep lives of 9.1 and 11.2 h, respectively, when the particle content reached 1 and 3 vol.%. However, a reduction of 5.5 h with 5 vol.% was seen due to the stress concentration, which is caused by the presence of large particle clusters. Microstructural observations indicated that the introduction of $ZrB_2$ (61 nm) and $Al_2O_3$ (49 nm) nanoparticles inhibited grain growth (68 μm) when compared with the 6016 alloy. In addition, θ and β phases decreased their diameters to 17 and 168 nm from 26 and 201 nm in the composite, inhibiting the dislocation movement, resulting in a higher creep resistance.

Huang et al. [42] investigated the synergetic effect of 1.3 wt% $Al_2O_3$ and 4.4 wt% $ZrB_2$ in the 7075-aluminum alloy to determine the creep resistance after the hot rolling deformation. The homogenized (743 K for 24 h) ($Al_2O_3$ + $ZrB_2$)/7075 Al composites subjected to 523, 543, and 563 K and 60, 70, and 80 MPa showed an apparent activation energy of ~370 kJ $mol^{-1}$, indicating the stability and efficiency of the nanoparticles at high temperatures. Particle characterization revealed that the average grain size in the reinforced composite was the smallest, with 4.07 μm, compared to the 7055 Al alloy (6.31 μm) and $ZrB_2$/7055 Al composites (4.42 μm). The authors associated this behavior with the inhibition of the recrystallization process due to the nanoparticles ($Al_2O_3$ and $ZrB_2$) and precipitates (Cu, Mg, and Zn), wherein a high concentration of precipitates was easy to obtain due to their nucleation at the interface between the nanoparticles and the Al matrix.

Abd-Elaziem et al. [43] reviewed the effect of metal-matrix nanocomposites on the creep behavior of aluminum alloys. The literature studied indicated that hard, non-shearable, incoherent nanoparticles in the Al matrix may increase the creep resistance by reducing load transfer and dislocation activities at the matrix reinforcement interfaces. This assumption was made because

the creep deformation of Al and its alloys is mostly caused by dislocation climb or gliding processes. Researchers also pointed out that smaller particle sizes may have major implications on the creep resistance due to their smaller spacing among each other. As a result, stiffer reinforcement can carry more stress load, allowing for higher applied stresses.

Studies have revealed that although the properties of Al alloys are improved with the addition of reinforcing second phases, factors such as porosity from composite processing, brittleness in the reinforcement material, and poor wettability in terms of bonding between the matrix and reinforcement may result in a reduction of the creep resistance with increasing temperature [44,45]. Therefore, a comprehensive review of the selection of proper reinforcement materials and methods to produce a homogenous distribution of the reinforcements in the Al matrix is needed to achieve the desired creep properties of the composites. Systematic studies on rate-governing creep mechanisms and activation energies would also be good contributions to the understanding of the roles of the reinforcements in creep behavior.

### 4.4.3 Additive Manufacturing

The additive manufacturing (AM) process provides a tool to create complex geometries, leading to the development of cylinder head and engine block designs [109]. In Al alloy design, AM may offer better creep performance over conventional manufacturing processes due to the formation of refined precipitates, control of particle distribution, and the ability to create high-volume fractions of thermally stable phases [47]. However, defects such as inhomogeneous microstructure, hot cracking, porosity, anisotropy, poor surface quality, and residual stresses during AM processing lead to deficient material properties [48,49]. Some recent studies that have contributed to this trend are presented below.

Michi et al. [50] investigated a creep-resistant, additively manufactured Al-Ce-Ni-Mn alloy in the 300–400 °C temperature range. The results indicated that the Al-10.5Ce-3.1Ni-1.2Mn alloy showed superior creep resistance to Al-12.5Ce, Al-6.4Cu-0.19Mn-0.13Zr, and Al-0.10Sc-0.12Er cast alloys. This behavior was associated with a higher volume fraction (35%) of submicron $Al_{11}Ce_3$ and $Al_3Ni$ precipitates, which are thermally stable up to ~400 °C that controlled the dislocation climb and acted as barriers to grain boundary migration. A low creep ductility in the alloy was observed due to the appearance of voids at the melt pool boundaries (MPBs) during AM processing.

Glerum et al. [51] investigated the creep properties and microstructure evolution at 260–300 °C of AlSi10Mg manufactured via laser powder-bed fusion. The Al-10Si-0.6Mg alloy subjected to compressive creep in the aged condition indicated an apparent activation energy equal to 256 kJ $mol^{-1}$ when tested at 200–320 °C and 45 MPa. The researchers compared the creep response to cast alloys strengthened via load transfer (Al-12.5Ce, Al-10Ce-5Ni, and Al6.9Ce-9.3Mg). Microstructural observations revealed that the Si phase in the LPBF alloy was much finer than the eutectic $Al_{11}Ce_3$ phase in the cast alloys due to the rapid solidification rate from the LPBF process.

Rakhmonov et al. [52] examined the laser-melted Al-3.6Mn-2.0Fe-1.8Si-0.9Zr (wt%) alloy with outstanding creep resistance due to the formation of α-Al(Fe,Mn)Si precipitates. Compressive creep results at 300 °C and 50–80 MPa on the aged alloy (350 °C for 8 h) showed lower stress exponents with better creep resistance when the alloy was compared with creep-resistant cast and AM Al alloys. This behavior was associated with the formation of submicron, thermally stable α-Al(Fe,Mn)Si precipitates with a high-volume fraction obtained from the rapid solidification rate of the LPBF process. The study revealed that α-Al(Fe,Mn)Si precipitates were responsible for

refining the α-Al grains, preventing cracking during LPBF processing, and inhibiting diffusion-controlled dislocation climb, generating an improvement in the creep resistance.

The key finding in studies on AM aluminum alloys is the observation of fine dispersoids/precipitates obtained because of the high solidification rates in LPBF. Submicron $Al_{11}Ce3$ and $Al_3Ni$ precipitates, fine eutectic Si phase, or α-Al(Fe,Mn)Si dispersoids were able to provide creep strengthening at temperatures in excess of 300 °C.

### 4.4.4 Thermal Barrier Coating

Thermal barrier coatings (TBCs) have the potential to improve the engine power and efficiency because they can be used to insulate the engine block and cylinder head (i.e., the inter-valve bridge area) against the thermal effect of the combustion gases responsible for producing creep deformation [53]. However, their use has been limited due to defects, such as porosity, cracking, residual stress, oxidation, thermal shock, and microstructure, which may influence their performance [53,54]. In addition, factors such as high surface roughness (increases heat transfer and slows down combustion) and translucency to thermal radiation may affect their effectiveness [55,56]. Recent studies in this field are presented below.

Wang et al. [57] investigated a high-entropy $Al_{0.6}CoCrFeNiTi$ alloy coating on the aluminum 4032 alloy substrate. The coating, formed via plasma spraying, showed lower thermal conductivity (3.00 W/mK at 100 °C) and higher thermal stability (up to 700 °C) than high-velocity oxygen-fuel-spraying. This indicated that the operating surface temperature of the piston crown could increase by 13 °C because the coating provided a temperature reduction of 19 °C. The researchers associated this behavior with the refinement of grains and disordered BCC structure produced from the combination of a high cooling rate and sluggish diffusion in $Al_{0.6}CoCrFeNiTi$. The study also

revealed that defects such as porosity and oxide inclusions influenced thermal insulation properties.

Vengatesan et al. [58] studied the influence of alloying elements on the performance of an Al-Si engine piston coated with 350 mm of $MgZrO_3$ and 150 mm of NiCrAl. It was reported that a high content of alloying elements, including Cu and Ni, required more time to heat the Al-Si alloy substrate, altering the thermal conductivity of the piston exterior. As a result, an increase in the temperature in the piston surface was seen, leading to an improvement of 55% in the surface temperature when compared to the aluminum alloy. Similarly, an increase in the coating thickness led to higher values in temperature than those in the uncoated piston. However, the authors associated the best thermal behavior with coatings containing holes, showing improvements of about 8–10% compared to pistons without holes and 32–47% compared to uncoated pistons.

M. Cerit and M. Coban conducted simulations on the temperature and stress distributions of an Al-Si-Cu-Mg-Cr alloy piston, plasma-sprayed with a magnesia-stabilized zirconia ($MgZrO_3$) thermal barrier coating, an intermediate layer of NiCrAl bond coat between the piston surface, and a ceramic topcoat [59]. They obtained a 9–20% reduction in the temperature and 33–57% reduction in the residual stresses of the piston's metal surface depending on the coating thickness.

The recent studies on TBC were all conducted on the pistons and not on the engine block: $MgZrO_3$ with an intermediate layer of NiCrAl produced temperature reductions of a minimum of ~10–20%, and the high-entropy $Al_{0.6}CoCrFeNiTi$ coating produced a reduction of ~20 °C (which can translate into a 7% reduction in temperature), providing a small improvement in creep behavior. The use of TBCs in the engine block can be a design element, as it can decrease the metal surface

temperature and, consequently, the creep temperature in the engine block, provided that good-quality, thick coatings can be achieved.

### 4.4.5 Nanostructured Aluminum Alloy

Nanostructured (NS) aluminum alloys produced from mechanical alloying, severe plastic deformation, and electrodeposition are considered as potential candidates to be used in lightweighting applications at elevated temperatures due to the combined effect of ultrafine grains and nanoparticles [60,61]. Several types of NS aluminum alloys have been developed [62]. These materials are not for cast parts. Although studies [63,64] on the diesel engine piston have shown suitable strength at elevated temperatures, no research has been conducted on engine blocks and cylinder heads. This may be due to low thermal stability in the diesel engine operating condition as well as the difficulty of producing a complex shape, such as the engine block, with these materials. There is an effort in this field with respect to thermal instability and grain size stabilization through thermodynamic stabilization and kinetic stabilization that is of interest to diesel engine applications [65,66]. The implementation of these materials in a cast diesel cylinder head is not straightforward. However, a future direction can be the use of these materials for selective strengthening of certain parts of the cylinder head. Recent studies in this area are presented below.

Markushev et al. [67] investigated the role of dispersed particles in nanocrystalline Al-Zn-Mg-Cu-Sc-Mn alloys under high-pressure torsion (HPT). The results indicated the absence of recrystallization in HPT samples after the pre-age condition (170 °C for 10 h) due to the high density of thermally stable transition metal aluminides. In addition, microstructural observations revealed that the suppression of the Al matrix nano-structuring was associated with the

homogeneity of plastic flow and prevention of dislocation rearrangements. In contrast, in the over-aged condition (250 for 5 h), the main strengthening phases increased their size and decreased their density, resulting in a reduction in hardness. A better understanding of the principles of optimization was obtained to develop stable nanostructures during service conditions.

Bobruk et al. [68] studied the Al 2024 alloy with ultrafine grains produced by HPT in combination with nanoscale precipitates of $Al_2CuMg$. Tensile mechanical tests at 190, 240, and 270 °C under a strain rate of $10^{-3}$ $s^{-1}$ demonstrated elongations of 130, 280, and 400%, respectively. Similarly, the microhardness was only slightly reduced, indicating the thermal stability of the alloy with increasing temperature. The super-plasticity behavior was associated with a uniform distribution of nanosized precipitates of $Al_2CuMg$ phase and grain boundary segregation that suppressed the recovery and recrystallization process. TEM analysis also indicated that the grain size of 0.1 μm was preserved in the 120–270 °C temperature range, with no structure degradation.

Galano et al. [69] reviewed the creep and deformation mechanisms at elevated temperatures in Al-based nano-quasicrystalline alloys that had quasi-crystalline phases with high Al concentrations, such as $Al_{78}Mn_{22}$, $Al_{86}V_{14}$, and $Al_{84.6}Cr_{15.4}$. They pointed out that the thermal stability of the nano-quasicrystalline-based alloys is mainly related to the stability of the metastable icosahedral phase, wherein phase and interface stabilization in the α-Al matrix should be maintained to preserve the microstructure, without considerable changes at elevated temperatures. The study indicated that the nano-quasicrystalline Al-Fe-Cr-based alloys have improved mechanical properties at elevated temperatures when compared with standard Al alloys. In terms of creep behavior, the Al-Fe-Cr-Ta alloy showed an apparent activation energy of 440 kJ $mol^{-1}$ in the temperature range of 573 K and 623 K due to the formation of fine particles with small inter-particle distances that controlled the dislocation motion.

Future strategies in the NS Al alloy design, such as the selection of stabilizing alloying elements, size, volume fraction and distribution of second-phase particles, and microstructural evolution, need further investigation. The incorporation of thermally stable nanostructured aluminum inserts in the cylinder head will be a viable engineering route in the development of aluminum diesel engines.

### 4.4.6 Machine Learning Design for Al Alloys

Machine learning (ML) has become a useful approach in Al alloy design using complex and high-dimensional datasets to predict the mechanical properties at high temperatures [70,71]. In creep-oriented alloy design, ML has been used to predict the primary parameters associated with creep behavior (lifetime, creep rate, creep strain, and creep curves) in different alloy systems [72,73]. However, its study in Al alloys remains untouched. Among the main factors is the limited data available, wherein alloy composition, microstructure, and processing conditions are included in the datasets for the resulting creep behavior [74]. The ML studies on aluminum have focused on optimizing heat treatment or fatigue properties, as discussed below.

Jiang et al. [75] designed a three-stage solution aging process using data transfer learning of 1053 data points on AA7xx series high-strength aluminum alloys. The prediction results were carried out on the Al-8.9Zn-2.29Mg-1.76Cu-0.14Cr-0.1Mn-0.1Zr-0.06Ti alloy previously determined by the authors using the machine learning method [76]. The UTS and elongation in the T66R process (450 °C for 1 h + 470 °C for 1 h + 480 °C for 0.5 h + 65 °C for 42 h + 100 °C for 16 h + 135 °C for 4 h) showed higher values than those of common T6-treated samples (470 °C for 2 h + 120 °C for 24 h). Experimental verification of the alloy revealed that UTS and elongation increased from 715 to 767 MPa and from 8.4 to 13.4%, respectively. Microstructural investigation associated this

behavior with the reduction of the amount of micron-scale insoluble phases, wherein finer and spherical dispersed nanoprecipitates increased their density by more than 50%.

Lian et al. [77] employed empirical formulae and data-driven models to predict the fatigue life of seven different series of Al alloys, with the purpose of handling small datasets. The transfer learning used in this work included fatigue strength and S-N curves obtained from literature, and the construction of two models, fatigue strength and S-N curves. As a result, quantitative relationships in the fatigue life based on the S-N curve model were obtained.

There is current research geared toward designing Al-Si-based diesel engine alloys by the authors using transfer learning models on datasets from aluminum and magnesium alloys and superalloys [78]. Ongoing work shows that creep data on aluminum casting alloys are limited. Transfer learning methods can be applied to magnesium, steel, or superalloy datasets, or parametric analyses can be performed to create new data. ML strategies, such as transfer learning, feature engineering, and physics-informed models, can be used in the future to address the data-related limitations.

### 4.4.7 The Manufacturing of the Aluminum Diesel Engine

The manufacturing of the diesel engine basically relies on casting processes. However, incorporating material solutions that are not developed for casting into the production of an aluminum diesel engine block is not straightforward. In this section, the conventional casting processes of aluminum alloys are summarized, and the selective reinforcement of the aluminum engine block is discussed.

#### 4.4.7.1 Casting Processes for Aluminum Engine Block [79,80]

Commercial aluminum casting alloys are developed and optimized for specific casting processes (Table 1). Commonly, thin-walled castings, such as the transmission case, can be cast via the high-cooling-rate HPDC (high-pressure diecasting) process, which generates supersaturated solid solution and refined microstructures that lead to high tensile properties without heat treatment. In fact, heat treatment cannot be applied to HPDC, unless the part is hot-isostatic-pressed to remove the air entrapped during turbulent flow into the die, which leads to blistering problems during heating. HPDC is not the most suitable technique for thicker wall castings, such as the engine block, due to high amounts of air entrapment and lower cooling rates obtained in thick sections. The engine block is preferentially cast using the permanent mold (PM) casting (or modified sand casting) with and without pressure assistance, e.g., gravity casting (GC) or low-pressure casting (LPC) techniques. To improve the casting soundness and properties of GC and LPC, the melt can be treated (degassed, grain refined, and chemically modified) [80].

Al-Si-based Alloys: Modifications of the A356 alloy constitute the bulk of the studies [18–28] of the first-, second-, and third-generation alloys. Cu and Ni additions, as well as low-level additions, can affect the castability and ductility of A356. However, no systematic study on the castability (hot-tearing tendency, porosity, and fluidity) of these alloys has been conducted.

Al-Cu-based Alloys: The alloys investigated in this system are highly experimental at this stage, sometimes containing high (9–27 wt%) Cu content. The value of these studies lies in the insight they provide into the alloy features that enhance creep resistance. The exception is the study of the Al-Cu 224 cast alloy [35], which is the modification (microalloying) of a commercial PM casting alloy.

*Table 4.1. Casting processes for commercial aluminum alloys.*

| Alloy | Casting Process | Alloy System | Applications |
|---|---|---|---|
| Al-Si-based alloys | | | |
| 356, 357 | Sand, PM, vacuum-assisted diecasting | Hypoeutectic Al-Si with 0.35 wt% Mg | Aircraft and aerospace, wheels, pillars, sub-frame |
| 319 | PM | Hypoeutectic Al-Si with 4% Cu | Cylinder heads, manifolds, engine blocks, internal engine part |
| 380 | HPDC | | Wheels, transmission case |
| 355, 332 | PM | Hypoeutectic Al-Si with Cu and Mg | Pistons and engine block (gas or diesel) |
| 390 | PM, HPDC | Hypereutectic Al-Si with Cu and Mg | Wear applications, engine block without iron sleeves |
| Al-Cu-based alloys | | | |
| 201 | Sand cast, PM | Al-Cu with Ag | Aircraft engines |
| 242 | PM | Al-Cu with Ni and Mg | Diesel engine pistons, air-cooled cylinder heads for aircraft engines |
| 224 | PM | Al-Cu | Catalytic converters, heat shields |

#### 4.4.7.2 Selective Reinforcement in the Diesel Engine

Selective reinforcement has been used in automotive engine applications in the past. In situ selectively reinforced (SF) pistons using liquid metal infiltration of ceramic fiber preforms was introduced by Toyota diesel engines in 1983. Subsequent uses of SF using aluminum matrix composites (AMCs) were piston cylinder bores by Porsche (Stuttgart, Germany) (Boxster, 911 Carrera) and since 1990 by Honda (Tokyo, Japan) (Prelude SI, Accord, V6 engine of Acura NSX, and S2000 Roadster). The design with selective reinforcement was successfully used by BMW on their creep-resistant magnesium AJ62 alloy engine block in all models between 2004 and 2015, using a cast aluminum alloy insert in the piston area to provide improved creep resistance in this region [81].

The inter-valve area of the diesel engine is positioned to benefit significantly from selective creep reinforcement using many of the materials discussed in Sections 4.1–4.3.

Al-Cu alloys [33–36], metal-matrix composites [37–45], and additively manufactured aluminum [46–52] can be used as selective reinforcement materials. Nano-structured aluminum [60–69] can be used as inserts to improve the creep resistance of the aluminum diesel engine in the inter-valve zone if the thermal stability can be improved. An integrated technology similar to the one that has been proposed for the integration of AM parts into subtractive production processes [82] can be used by employing robot arms to move inserts, molds, and molten alloy to produce the component.

## 4.5 Conclusions and Future Directions

The review of the literature and research on the development of creep-resistant aluminum alloys intended for diesel engine applications showed that diesel engines will continue to be employed in heavy vehicles due to the limitations of battery technology and charging infrastructure of electric vehicles. High thermal gradients occurring during diesel engine operation render creep resistance a key requirement for the diesel engine cylinder head and engine block. The review also showed that there is still much work to be carried out before aluminum diesel engines can become commercially viable. The following points will pave the path to the effective development of this important application.

Effective Dispersoids: Research shows that dispersion strengthening is an effective way to control creep deformation, achieved by the addition of transition metals to Al-Si- or Al-Cu-based alloys. The dispersoids slow softening processes, such as dislocation climb, sub-grain formation, and sub-grain migration, minimizing dynamic recovery. The extent of dispersoids' effectiveness depends on their thermal stability, size, and coherency.

A direct comparison of the experimental alloys investigated in the studies reviewed is difficult, as the creep stresses and temperatures differ. There is also a difference between tensile and compressive creep rates, especially when cast samples have porosity, inclusions, or very brittle phases that cause early failure in tensile creep. The minimum creep rate can be lowered by an order of magnitude. Furthermore, experimental alloys are usually not optimized for casting, and the tensile properties may be lower than the values obtained on sound castings. A partial comparison is provided in Table 4.2, which presents steady-state (minimum) creep rates and second phases that provide creep resistance.

*Table 4.2. Creep parameters of experimental aluminum alloys for the diesel engine.*

| **Alloy (Compositions in Weight Percentage)** | **Min. Creep Rate ($s^{-1}$)** | | **Creep Enhancers** | **Ref.** |
|---|---|---|---|---|
| | **Tensile** | **Compressive** | | |
| Al-Si-based alloys creep-tested at 300 °C and 30 MPa | | | | |
| A356 + 0.5Cu | $4.5 \times 10^{-6}$ | $2 \times 10^{-7}$ | 50 nm noncoherent α-Al(Mn,Fe)Si | [18,32] |
| A356 + 0.5Cu + 0.2Mn + 0.2Cr + 0.2Zr | $1.4 \times 10^{-6}$ | - | 5 nm coherent α-Al(Mn,Cr,Fe)Si | [32] |
| A356 + 0.5Cu + 0.3Mo | $1.0 \times 10^{-6}$ | - | α-Al(Fe,Mo)Si | [25] |
| A356 + 0.5Cu + 0.3Mo + 0.2Mn | $2.1 \times 10^{-6}$ | | α-Al(Mn,Mo,Fe)Si | [27] |
| Al-0.1Si-0.1Mn-0.1Mo-0.08Zr-0.01Er-0.02Sc | - | $2 \times 10^{-7}$ | $Al_3$(Zr,Sc,Er), submicron α-Al(Mn,Mo)Si | [29] |
| Al-Cu-based alloys creep-tested at 300 °C and 50 MPa | | | | |
| Al-5Cu-(Si, Fe, Mg, Ti 0.1%ea) | - | $2.2 \times 10^{-7}$ | θ′, θ″ | [35] |
| Al-5Cu-0.18Zr-(Si, Fe, Mg, Ti 0.1ea) | - | $2.8 \times 10^{-8}$ | θ′, θ″, $Al_3$(Zr) | |
| Al-5Cu-0.25V-(Si, Fe, Mg, Ti 0.1ea) | - | $8.4 \times 10^{-8}$ | θ′, θ″ | |
| Al-5Cu-0.15Zr-0.13V-(Si, Fe, Mg, Ti 0.1ea) | - | $1.3 \times 10^{-8}$ | θ′, θ″ | |
| Al-5Cu-0.15Zr-0.16Sc-(Si, Fe, Mg, Ti 0.1ea) | - | $5.5 \times 10^{-9}$ | θ′, θ″, $Al_3$(Sc,Zr) | |
| Al-6Cu-0.4Mn-0.16Zr-0.08Si | $7.0 \times 10^{-8}$ | $6.0 \times 10^{-8}$ | θ′, θ | [36] |
| Al-8.5Cu-0.4Mn-0.16Zr-0.07Si | $2.0 \times 10^{-8}$ | $6.0 \times 10^{-9}$ | θ′, θ | |

In Al-Si-Cu-Mg alloys, modifications of α-Al(Mn,Fe)Si with low additions of Mo, Mn, and Cr have a beneficial role by increasing the coherency, thermal stability, and the coherency of the

dispersoids. Though the findings can still be considered a work in progress, the efficiency of the modified dispersoids can be ranked in descending order of effectiveness as:

$$\alpha\text{-Al(Fe,Mo)Si} > \alpha\text{-Al(Mn,Cr,Fe)Si} > \alpha\text{-Al(Mn,Mo,Fe)Si}$$

Al-Cu-based alloys show lower minimum creep rates than the Al-Si-based alloys. However, these alloys are known to have lower castability and can have ductility and corrosion problems. In both alloy systems, the combined addition of Zr and Sc generates the $Al_3(Sc,Zr)$ phase, which seems to lead to the lowest creep rates.

Future studies should emphasize creep tests that use the conditions of the diesel engine service temperatures and stresses. Compressive creep is more representative of the inter-valve creep conditions, but it may mask the inherent problems of the alloys, such as their tendency to crack formation. Tensile creep tests underestimate the alloy's creep resistance if the samples have casting defects. Alloy comparisons must be made either on compressive or tensile creep or both. The improvement of the ductility and castability of the Al-Cu alloys is also a topic of interest for the future.

Alternative ways of improving creep resistance or elevated-temperate performance in aluminum: Alternative ways (other than casting alloys) were also reviewed in this paper. Composites can develop creep resistance by inhibiting recrystallization but can suffer from interface debonding. An interesting direction in the development of aluminum diesel engine alloy is through additive manufacturing (AM). The development of submicron dispersoids is very effective in improving creep resistance in AM aluminum alloys. The processing of these alloys does not lead to effective manufacturability of the diesel engine block but selective reinforcement of the block in the inter-valve region using inserts of these materials. This is an equally important topic to investigate in

the future. Nano-structuring is seen to be challenged by thermal instability, requiring further research in stabilization. Their incorporation into the aluminum diesel engine as selective reinforcers would be a viable future direction. Thermal coatings can reduce creep deformation by limiting the temperature increase in the alloy.

The future trends in heat-resistant aluminum alloys involve their process optimization, alloy design by dispersoid design and/or via machine learning, incorporation of inserts of AM and AMCs, and advanced coating technologies to obtain Al alloy components with longer durability, higher efficiency, and better performance. The development and deployment of these materials and processes in diesel engines need to be accelerated to improve sustainability in heavy vehicles. The research can benefit from funding of multi-partner precompetitive research projects that combine multiple end-users, multiple alloys, alloy suppliers, and manufacturing into a systematic study with a focus on application.

**Funding:** This research was supported by the Natural Sciences and Engineering Research Council of Canada (NSERC). Raul Irving Arriaga Benitez would like to gratefully acknowledge the financial support of the Gerald Hatch Fellowship (Grant No. 256938), Fonds Québécois de la Recherche sur la Nature et les Technologies—Programme de Bourses d'Excellence pour Étudiants Étrangers (FRQNT—PBEEE; Grant No. 451069), and Consejo Nacional de Humanidades, Ciencias y Tecnologias—Secretaria de Energia (CONAHCyT—SENER; Grant No. 451069).

## 4.6 References

[1] International Energy Agency;, Global EV outlook 2023: catching up with climate ambitions, Paris, France, 2023, pp. 14–43. https://doi.org/10.1787/cbe724e8-en.

[2] I.N. Fridlyander, V.G. Sister, O.E. Grushko, V.V. Berstenev, L.M. Sheveleva, L.A. Ivanova, Aluminum alloys: promising materials in the automotive industry, Met. Sci. Heat Treat. 44

(2002) 365–370. https://doi.org/10.1023/A:1021901715578.

[3] A. König, L. Nicoletti, D. Schröder, S. Wolff, A. Waclaw, M. Lienkamp, An overview of parameter and cost for battery electric vehicles, World Electr. Veh. J. 12 (2021) 1–29. https://doi.org/10.3390/wevj12010021.

[4] S. Pelletier, O. Jabali, G. Laporte, M. Veneroni, Battery degradation and behaviour for electric vehicles: Review and numerical analyses of several models, Transp. Res. B: Methodol. 103 (2017) 158–187. https://doi.org/10.1016/j.trb.2017.01.020.

[5] F. Alanazi, Electric vehicles: benefits, challenges, and potential solutions for widespread adaptation, Appl. Sci. 13 (2023) 6016. https://doi.org/10.3390/app13106016.

[6] National Academies of Sciences, Engineering, and Medicine 2021., Powering the U.S. army of the future, National Academies Press, Washington, DC, USA, 2021. https://doi.org/10.1080/0889311x.2021.1972098.

[7] International Energy Agency;, Global EV outlook 2023: catching up with climate ambitions, Paris, France, 2023, pp. 9–10. https://doi.org/10.1787/cbe724e8-en.

[8] K. Hoag, B. Dondlinger, Cylinder block and head materials and manufacturing, in: K. Hoag, B. Dondlinger (Eds.), Vehicular Engine Design, 2nd ed., Springer, Vienna, Austria, 2016: pp. 1–386. https://doi.org/10.1007/978-3-7091-1859-7.

[9] Q. Xin, Durability and reliability in diesel engine system design, in: Q. Xin (Ed.), Diesel Engine System Design, 1st ed., Woodhead Publishing Limited, Cambridge, UK, 2011: pp. 143–145. https://doi.org/10.1533/9780857090836.

[10] M. Azadi, Failure analysis and prevention in powertrain systems, in: A.S.H. Makhlouf, M. Aliofkhazraei (Eds.), Handbook of Materials Failure Analysis with Case Studies from the Aerospace and Automotive Industries, 1st ed., Butterworth-Heinemann, Kidlington, England, 2016: pp. 471–491.

[11] N. Tiney, M. Spiller, V. Pržulj, R. Penning, Conjugate Heat Transfer Modelling of Internal Combustion Engine, MTZ Worldw 73 (2012) 44–49. https://doi.org/10.1007/s38313-012-0251-1.

[12] H. Ye, An overview of the development of Al-Si-alloy based material for engine applications, J. Mater. Eng. Perform. 12 (2003) 288–297. https://doi.org/10.1361/105994903770343132.

[13] M. Garat, G. Laslaz, Improved aluminium alloys for common rail diesel cylinder heads, AFS Transactions 115 (2007) 1–8.

[14] H. Zhang, Y. Cui, G. Liang, L. Li, G. Zhang, X. Qiao, Fatigue life prediction analysis of high-intensity marine diesel engine cylinder head based on fast thermal fluid solid coupling method, J Braz. Soc. Mech. Sci. Eng. 43 (2021) 327. https://doi.org/10.1007/s40430-021-03049-7.

[15] H. Zhang, G. Liang, X. Qiao, Z. Lyu, L. Li, G. Zhang, Y. Cui, Experimental and numerical study of inelastic behavior based on simulated cylinder head specimen under thermal cycling conditions, J Braz. Soc. Mech. Sci. Eng. 44 (2022) 372. https://doi.org/10.1007/s40430-022-03652-2.

[16] E. Natesan, J. Ahlström, S. Eriksson, C. Persson, Effects of Temperature on the evolution of yield surface and stress asymmetry in A356–T7 cast aluminium alloy, Materials 14 (2021) 7898. https://doi.org/10.3390/ma14247898.

[17] K. Bhanu Sankara Rao, B. Raj, A. Nagesha, Fatigue testing: thermal and thermomechanical, in: K.H.J. Buschow, M.C. Flemings, E.J. Kramer, P. Veyssière, R.W. Cahn, B. Ilschner, S. Mahajan (Eds.), Reference Module in Materials Science and Materials Engineering, Elsevier, Amsterdam, 2017: pp. 8687–8691. https://doi.org/10.1016/B978-0-12-803581-8.03464-0.

[18] M. Pekguleryuz, E. Ozbakir, A.R. Farkoosh, Diesel engine: applications of aluminum alloys, in: G.E. Totten, M. Tiryakioglu, O. Kessler (Eds.), Encyclopedia of Aluminum and Its Alloys, CRC Press, Boca Raton, 2018: pp. 743–762.

[19] F. Feikus, Optimisation of Al-Si cast alloys for cylinder head applications, AFS Transactions 106 (1998) 1–21.

[20] A. Biswas, D.J. Siegel, D.N. Seidman, Compositional evolution of Q-phase precipitates in an aluminum alloy, Acta Mater. 75 (2014) 322–336. https://doi.org/10.1016/j.actamat.2014.05.001.

[21] F. Stadler, H. Antrekowitsch, W. Fragner, H. Kaufmann, P.J. Uggowitzer, Effect of main alloying elements on strength of Al-Si foundry alloys at elevated temperatures, Int. J. Cast Met. Res. 25 (2012) 215–224. https://doi.org/10.1179/1743133612Y.0000000004.

[22] L. Heysler, F. Feikus, M. Otte, Alloy and casting process optimization for engine block application, AFS Transactions 050 (2001) 1–9.

[23] A.R. Farkoosh, M. Pekguleryuz, The effects of manganese on the T-phase and creep resistance in Al-Si-Cu-Mg-Ni alloys, Mater. Sci. Eng. A. 582 (2013) 248–256. https://doi.org/10.1016/j.msea.2013.06.030.

[24] K.E. Knipling, D.C. Dunand, D.N. Seidman, Criteria for developing castable, creep-resistant aluminum-based alloys - A review, IJMR. 97 (2006) 246–265. https://doi.org/10.1515/ijmr-2006-0042.

[25] A.R. Farkoosh, Development of creep-resistant Al-Si cast alloys strengthened with nanoscale dispersoids, PhD Thesis, McGill University, 2014.

[26] E. Ozbakir, Development of aluminum alloys for diesel-engine. Master's Thesis, McGill University, 2008.

[27] A.R. Farkoosh, X. Grant Chen, M. Pekguleryuz, Interaction between molybdenum and manganese to form effective dispersoids in an Al-Si-Cu-Mg alloy and their influence on creep resistance, Mater. Sci. Eng. A. 627 (2015) 127–138. https://doi.org/10.1016/j.msea.2014.12.115.

[28] S. Rashno, M. Reihanian, K. Ranjbar, Tensile and creep properties of Al–7Si–0.3Mg alloy with Zr and Er addition, Mat. Sci. Technol. 36 (2020) 1603–1613. https://doi.org/10.1080/02670836.2020.1809144.

[29] A. De Luca, D.N. Seidman, D.C. Dunand, Mn and Mo additions to a dilute Al-Zr-Sc-Er-Si-based alloy to improve creep resistance through solid-solution- and precipitation-strengthening, Acta Mater. 194 (2020) 60–67.

https://doi.org/10.1016/j.actamat.2020.04.022.

[30] D. Li, K. Liu, X.-G. Chen, Evolution of microstructure and elevated-temperature properties during thermal exposure with transition elements (V, Zr and Mo) in Al–Si 356 type cast alloys, Mater. Trans. 64 (2023) 406–413. https://doi.org/10.2320/matertrans.MT-LA2022003.

[31] W. Qian, X. Kai, R. Tao, X. Gao, L. Huang, Y. Zhao, The corelation between creep resistance and microstructure in AA6111 alloy strengthened by synergistic Er, Zr addition, Mater. Sci. Eng. A. 870 (2023) 144867. https://doi.org/10.1016/j.msea.2023.144867.

[32] R.I. Arriaga-Benitez, M. Pekguleryuz, The synergistic effects of nano-sized α-Al(Mn,Cr,Fe)Si and Al–Si–Zr dispersoids on the creep behavior Al–Si–Mg–Cu (Mn, Cr, Zr) diesel engine alloy, Mater. Sci. Eng. A. 872 (2023) 144949. https://doi.org/10.1016/j.msea.2023.144949.

[33] S. A. Awe, S. Seifeddine, A. E. W. Jarfors, Young. C. Lee, A. K. Dahle, Development of new Al-Cu-Si alloys for high temperature performance, Adv. Mater. Lett. 8 (2017) 695–701. https://doi.org/10.5185/amlett.2017.1471.

[34] Y.H. Gao, L.F. Cao, J. Kuang, J.Y. Zhang, G. Liu, J. Sun, Assembling dual precipitates to improve high-temperature resistance of multi-microalloyed Al–Cu alloys, J. Alloys Compd. 822 (2020) 153629. https://doi.org/10.1016/j.jallcom.2019.153629.

[35] D. Li, K. Liu, J. Rakhmonov, X.-G. Chen, Enhanced thermal stability of precipitates and elevated-temperature properties via microalloying with transition metals (Zr, V and Sc) in Al–Cu 224 cast alloys, Mater. Sci. Eng. A. 827 (2021) 142090. https://doi.org/10.1016/j.msea.2021.142090.

[36] S. Bahl, J.U. Rakhmonov, C. Kenel, D.C. Dunand, A. Shyam, Effect of grain-boundary θ-Al2Cu precipitates on tensile and compressive creep properties of cast Al–Cu–Mn–Zr alloys, Mater. Sci. Eng. A. 840 (2022) 142946. https://doi.org/10.1016/j.msea.2022.142946.

[37] D.K. Koli, G. Agnihotri, R. Purohit, Advanced aluminium matrix composites: the critical need of automotive and aerospace engineering fields, Mater. Today: Proc. 2 (2015) 3032–3041. https://doi.org/10.1016/j.matpr.2015.07.290.

[38] A.V. Narivskyi, M.M. Voron, M.A. Fon Pruss, V.V. Perekhoda, O.V. Chistyakov, Principles of creep-resistant aluminum alloys development, Casting Processes 143 (2021) 50–56. https://doi.org/10.15407/plit2021.01.050.

[39] C.O. Ujah, D.V.V. Kallon, Trends in aluminium matrix composite development, Crystals 12 (2022) 1357. https://doi.org/10.3390/cryst12101357.

[40] Y. Ji, Y. Yuan, W. Zhang, Y. Xu, Y. Liu, Elevated temperature tensile creep behavior of aluminum borate whisker-reinforced aluminum alloy composites (ABOw/Al–12Si), Materials 14 (2021) 1217. https://doi.org/10.3390/ma14051217.

[41] P. Zhao, Y. Zhao, X. Kai, L. Huang, M. Zhang, W. Chen, Research on microstructure and high-temperature creep behavior of in-situ (ZrB2+Al2O3)/AA6016 nanocomposite, Int. J. Met. (2023). https://doi.org/10.1007/s40962-023-01057-y.

[42] L. Huang, Y. Zhao, X. Kai, C. Guan, X. Gao, P. Zhao, T. Wang, Research on high strength and creep behavior of in-situ (Al2O3 + ZrB2)/7055 Al nanocomposites, Mater. Charact. 193

(2022) 112296. https://doi.org/10.1016/j.matchar.2022.112296.

[43] W. Abd-Elaziem, J. Liu, N. Ghoniem, X. Li, Effect of nanoparticles on creep behaviour of metals: A review, JMR&T. 26 (2023) 3025–3053. https://doi.org/10.1016/j.jmrt.2023.08.068.

[44] O.P. Oladijo, S.A. Awe, E.T. Akinlabi, R.R. Phiri, L.L. Collieus, R.E. Phuti, High-temperature properties of metal matrix composites, in: Dermot Brabazon (Ed.), Encyclopedia of Materials: Composites, 1st ed., Elsevier, Radarweg, Netherlands, 2021: pp. 360–374. https://doi.org/10.1016/B978-0-12-819724-0.00096-3.

[45] P. Samal, P.R. Vundavilli, A. Meher, M.M. Mahapatra, Recent progress in aluminum metal matrix composites: A review on processing, mechanical and wear properties, J. Manuf. Process. 59 (2020) 131–152. https://doi.org/10.1016/j.jmapro.2020.09.010.

[46] J. Gray, C. Depcik, Review of additive manufacturing for internal combustion engine components, SAE Int. J. Engines. 13 (2020) 617–632. https://doi.org/10.4271/03-13-05-0039.

[47] R.A. Michi, A. Plotkowski, A. Shyam, R.R. Dehoff, S.S. Babu, Towards high-temperature applications of aluminium alloys enabled by additive manufacturing, Int. Mater. Rev. 67 (2022) 298–345. https://doi.org/10.1080/09506608.2021.1951580.

[48] S.C. Altıparmak, V.A. Yardley, Z. Shi, J. Lin, Challenges in additive manufacturing of high-strength aluminium alloys and current developments in hybrid additive manufacturing, Int. J. Lightweight Mater. Manuf. 4 (2021) 246–261. https://doi.org/10.1016/j.ijlmm.2020.12.004.

[49] Y. Ding, J.A. Muñiz-Lerma, M. Trask, S. Chou, A. Walker, M. Brochu, Microstructure and mechanical property considerations in additive manufacturing of aluminum alloys, MRS Bull. 41 (2016) 745–751. https://doi.org/10.1557/mrs.2016.214.

[50] R.A. Michi, K. Sisco, S. Bahl, Y. Yang, J.D. Poplawsky, L.F. Allard, R.R. Dehoff, A. Plotkowski, A. Shyam, A creep-resistant additively manufactured Al-Ce-Ni-Mn alloy, Acta Mater. 227 (2022) 117699. https://doi.org/10.1016/j.actamat.2022.117699.

[51] J.A. Glerum, J.E. Mogonye, D.C. Dunand, Creep properties and microstructure evolution at 260–300 °C of AlSi10Mg manufactured via laser powder-bed fusion, Mater. Sci. Eng. A. 843 (2022) 143075. https://doi.org/10.1016/j.msea.2022.143075.

[52] J.U. Rakhmonov, N.Q. Vo, J.R. Croteau, J. Dorn, D.C. Dunand, Laser-melted Al-3.6Mn-2.0Fe-1.8Si-0.9Zr (wt%) alloy with outstanding creep resistance via formation of α-Al(FeMn)Si precipitates, Addit. Manuf. 60 (2022) 103285. https://doi.org/10.1016/j.addma.2022.103285.

[53] V.S. Godiganur, S. Nayaka, G.N. Kumar, Thermal barrier coating for diesel engine application - A review, Mater. Today: Proc. 45 (2020) 133–137. https://doi.org/10.1016/j.matpr.2020.10.112.

[54] National Research Council., Coatings for High-Temperature Structural Materials, The National Academies Press, Washington, DC, USA, 1996, pp. 26–33.

[55] J. Somhorst, M. Oevermann, M. Bovo, I. Denbratt, Evaluation of thermal barrier coatings and surface roughness in a single-cylinder light-duty diesel engine, Int. J. Engine Res. 22

(2021) 890–910. https://doi.org/10.1177/1468087419875837.

[56] K.Z. Mendera, Effectiveness of Plasma Sprayed Coatings for Engine Combustion Chamber, in: International Fuels & Lubricants Meeting & Exposition, Texas, USA, 2000. https://doi.org/10.4271/2000-01-2982.

[57] X. Wang, H. Yao, L. Yuan, L. Chen, F. Xu, Z. Tan, D. He, Y. Yang, Y. Liu, Z. Zhou, Novel candidate of metal-based thermal barrier coatings: High-entropy alloy, Surf. Coat. Technol. 474 (2023) 130087. https://doi.org/10.1016/j.surfcoat.2023.130087.

[58] S. Vengatesan, P. Yadav, E.G. Varuvel, Effect of alloying elements and ceramic coating on the surface temperature of an aluminum piston in a diesel engine, J. Nanomater. 2022 (2022) 1–11. https://doi.org/10.1155/2022/9916742.

[59] M. Cerit, M. Coban, Temperature and thermal stress analyses of a ceramic-coated aluminum alloy piston used in a diesel engine, Int. J. Therm. Sci. 77 (2014) 11–18. https://doi.org/10.1016/j.ijthermalsci.2013.10.009.

[60] F. Czerwinski, Thermal stability of aluminum alloys, Materials 13 (2020) 1–49. https://doi.org/10.3390/ma13153441.

[61] P. Cavaliere, Nanostructuring of metals, alloys, and composites, in: Pasquale Cavaliere (Ed.), Fatigue and Fracture of Nanostructured Materials, 1st ed, Springer, Heidelberg, Germany, 2021: pp. 1–58. https://doi.org/10.1007/978-3-030-58088-9_1.

[62] A. Inoue, F. Kong, S. Zhu, C.T. Liu, F. Al-Marzouki, Development and applications of highly functional al-based materials by use of metastable phases, Mater. Res. 18 (2015) 1414–1425. https://doi.org/10.1590/1516-1439.058815.

[63] H. Adil, Characterisation of a new nanostructured aluminium alloy and piston design for internal combustion engines, PhD Thesis, Oxford Brookes University, 2023.

[64] Department of Energy., www.Energy.Gov/Eere/Vehicles/Articles/High-Temperature-Aluminum-Alloys [Accessed: 2023-11-28] (n.d.). www.energy.gov/eere/vehicles/articles/high-temperature-aluminum-alloys (accessed November 28, 2023).

[65] H.R. Peng, M.M. Gong, Y.Z. Chen, F. Liu, Thermal stability of nanocrystalline materials: thermodynamics and kinetics, Int. Mater. Rev. 62 (2017) 303–333. https://doi.org/10.1080/09506608.2016.1257536.

[66] H. Asgharzadeh, H.J. McQueen, Grain growth and stabilisation of nanostructured aluminium at high temperatures: Review, Mater. Sci. Technol. 31 (2015) 1016–1034. https://doi.org/10.1179/1743284714Y.0000000706.

[67] M.V. Markushev, E.V. Avtokratova, S.V. Krymskiy, O.Sh. Sitdikov, Effect of precipitates on nanostructuring and strengthening of high-strength aluminum alloys under high pressure torsion, J. Alloys Compd. 743 (2018) 773–779. https://doi.org/10.1016/j.jallcom.2018.02.047.

[68] E.V. Bobruk, M.Yu. Murashkin, I.A. Ramazanov, V.U. Kazykhanov, R.Z. Valiev, Low-temperature superplasticity and high strength in the Al 2024 Alloy with ultrafine grains, Materials 16 (2023) 727. https://doi.org/10.3390/ma16020727.

[69] M. Galano, F. Audebert, Novel Al based nanoquasicrystalline alloys, Prog. Mater. Sci. 123 (2022) 100831. https://doi.org/10.1016/j.pmatsci.2021.100831.

[70] U. Masood Chaudry, K. Hamad, T. Abuhmed, Machine learning-aided design of aluminum alloys with high performance, Mater. Today Commun. 26 (2021) 101897. https://doi.org/10.1016/j.mtcomm.2020.101897.

[71] J. Wang, A. Yousefzadi Nobakht, J.D. Blanks, D. Shin, S. Lee, A. Shyam, H. Rezayat, S. Shin, Machine learning for thermal transport analysis of aluminum alloys with precipitate morphology, Adv. Theory Simul. 2 (2019) 1800196. https://doi.org/10.1002/adts.201800196.

[72] J. Wang, Y. Fa, Y. Tian, X. Yu, A machine-learning approach to predict creep properties of Cr–Mo steel with time-temperature parameters, J. Mater. Res. Technol. 13 (2021) 635–650. https://doi.org/10.1016/j.jmrt.2021.04.079.

[73] S. Dutta, P.S. Robi, Experimental investigation and modeling of creep curve of Zr–2.5Nb alloy by machine learning techniques, Met. Mater. Int. 28 (2022) 2884–2897. https://doi.org/10.1007/s12540-022-01182-z.

[74] X. Liu, P. Xu, J. Zhao, W. Lu, M. Li, G. Wang, Material machine learning for alloys: Applications, challenges and perspectives, J. Alloys Compd. 921 (2022) 165984. https://doi.org/10.1016/j.jallcom.2022.165984.

[75] L. Jiang, Z. Zhang, H. Hu, X. He, H. Fu, J. Xie, A rapid and effective method for alloy materials design via sample data transfer machine learning, Npj Comput. Mater. 9 (2023) 26. https://doi.org/10.1038/s41524-023-00979-9.

[76] L. Jiang, C. Wang, H. Fu, J. Shen, Z. Zhang, J. Xie, Discovery of aluminum alloys with ultra-strength and high-toughness via a property-oriented design strategy, J. Mater. Sci. Technol. 98 (2022) 33–43. https://doi.org/10.1016/j.jmst.2021.05.011.

[77] Z. Lian, M. Li, W. Lu, Fatigue life prediction of aluminum alloy via knowledge-based machine learning, Int. J. Fatigue. 157 (2022) 106716. https://doi.org/10.1016/j.ijfatigue.2021.106716.

[78] Y. Wang, Pekguleryuz, M., Sari, Y.A., ML Study on Al Alloys for the Prediction of Creep Resistant Alloy Compositions. McGill University, Montreal, Quebec, Canada, 2024, Status (manuscript in preparation) (n.d.).

[79] I.J. Polmear, D. StJohn, J.-F. Nie, M. Qian, Light alloys: metallurgy of the light metals, 5th ed., Butterworth-Heinemann, Oxford, England, 2017.

[80] J.E. Gruzleski, B.M. Closset, The treatment of liquid Aluminium-Silicon alloys, American Foundrymen's Society, DesPlaines, USA, 1999.

[81] M. Hoeschl, W. Wagener, J. Wolf, BMW's magnesium-aluminium composite crankcase, state-of-the-art light metal casting and manufacturing, in: 2006: pp. 2006-01–0069. https://doi.org/10.4271/2006-01-0069.

[82] P. Stavropoulos, P. Foteinopoulos, A. Papacharalampopoulos, H. Bikas, Addressing the challenges for the industrial application of additive manufacturing: Towards a hybrid solution, International Journal of Lightweight Materials and Manufacture 1 (2018) 157–168. https://doi.org/10.1016/j.ijlmm.2018.07.002.

# CHAPTER 5: THE INFLUENCE OF DISPERSOIDS AND SOLUTES ON THE RECOVERY PROCESESS OF CREEP DEFORMATION IN AN Al-Si-Mg-Cu (Mo, Mn) DIESEL ENGINE ALLOY

The first part of this PhD (Chapter 3) showed successful implementation of the systematic study of creep based on electron microscopy analyses of creep tested samples to identify the rate controlling creep mechanisms aluminium alloys. Research has also shown that the level of Mn has an influence on the creep resistance of Al-Si-Cu-Mg-Mn alloys. This part of the PhD research aimed at evaluating the creep mechanisms in Al alloys with different concentration of Mn. A comparison was conducted to understand the correlation between dispersoids and solutes and the creep behavior. This chapter has been accepted as a journal article: R.I. Arriaga-Benitez, M. Pekguleryuz, The Influence of Dispersoids and Solutes on the Recovery Processes of Creep Deformation in an Al-Si-Mg-Cu (Mo, Mn) Diesel Engine Alloy, J. Mater. Sci. 60, 2554–2579 (2025).

## ABSTRACT

The creep behavior of Mn-modified Al-Si-Mg-Cu-Mo alloy intended for diesel engine applications was investigated. Al-7Si-0.3Mg-0.5Cu-0.15Mn-0.3Mo (MG3-1) and Al-7Si-0.3Mg-0.5Cu-0.5Mn-0.3Mo (MG4-1) alloys presented apparent activation energies for creep of 203 kJ $mol^{-1}$ and 249 kJ $mol^{-1}$, respectively. TEM results indicated that in both alloys, dynamic recovery was the rate governing mechanism and sub-grains were associated with Si phase particles. MG4-1 had finer sub-grains and a lower creep rate than the MG3-1. In the MG3-1 alloy, the effective diffusion coefficient, $D_{eff}$, of dynamic recovery and the apparent activation energy for creep, $Q_a$, agreed with the coefficient and the activation energy of Mn diffusion in aluminum, respectively. Si diffusion played a key role in governing the creep rate of MG4-1 where Si diffusion was limited due to the stability of the α-Al(Fe,Mn,Mo)Si dispersoids; this limited the coarsening of Si particles and reduced their effect in initiating recovery. Differences in the size and coherency of α-Al(Fe,Mn,Mo)Si dispersoids that were observed and were attributed to the higher thermal stability and lower coarsening rate of the intermetallics at the solutionizing temperature. Coherent shearable α-Al(Fe,Mn,Mo)Si dispersoids did not provide sub-grain boundary pining in MG3-1. Coherent non-shearable α-Al(Fe,Mn,Mo)Si dispersoids in the size range of 6 nm pinned sub-grain boundaries in MG4-1. The apparent activation energy for creep in MG4-1 had contributions from the activation energy for Si diffusion in aluminum, pipe diffusion that governs sub-grain boundary migration, and Zener pinning by non-shearable coherent dispersoids.



*Keywords: Dispersoid; Al alloy; Creep resistance; TEM; Thermodynamic calculation*

## 5.1 Introduction

The electric vehicle is a key technology for the future of the automotive industry in the 2020s. However, diesel engines continue to maintain a strong presence in the maritime, agricultural, construction, mining and railway sector because of performance, reliability, and durability and the difficulty in electrifying these heavy and off-road transport vehicles. The use of lightweight aluminum (Al) alloys in engine blocks and cylinder heads is an effective way to improve their environmental viability through vehicle weight reduction.

Dispersoid strengthening in Al alloys with peritectic elements has been shown to be viable candidates to provide creep resistance at the diesel engine operating conditions; peritectic elements form thermally stable and intragranular particles for dislocation and grain boundary pinning [1–3]. Previous studies [4,5] have demonstrated that Mn and Mo added to the commercial A356 alloy modify the acicular β-$Al_5FeSi$ phase into α-Al(Fe,Mn)Si and α-Al(Fe,Mo)-Si phases. These nano-size α-particles (50-200 nm) of high thermal stability and partial coherence precipitate during solution treatment in large volume fractions, decreasing the minimum creep rate and increasing the creep time-to-fracture and strain-to-fracture [5]. In many creep studies on dispersoid strengthened alloys, a threshold stress is determined and the creep-rate controlling mechanism is identified as dislocation climb with an activation energy equaling self diffusion [6]. Here, the concept of threshold stress conceals the actual physical processes occurring during creep and cannot deconvolute the various effects of the dispersoids. In their previous study, the authors have discussed the shortcomings of this approach as the analysis cannot determine the actual role of the dispersoids in creep (e.g., pinning of dislocations, grain boundaries, or sub grain boundaries) [6]. In recent studies [3,6], the authors have been addressing these shortcomings and determining

creep-rate controlling micro-mechanisms in Al alloys strengthened with dispersoids that bear peritectic elements. The objectives have been to relate activation energies to the interaction of microstructural features with creep processes. The findings revealed that the role of the dispersoids differ; they can provide obstacles to dislocations or pin sub-grain boundaries slowing or inhibiting restoration processes, and these effects may be related to the size and the coherency of the dispersoids [6]. Activation energies of the rate controlling micro-mechanisms differ depending on the specific interactions of coherent and non-coherent particles with dislocations or boundaries. It must be noted that the dispersoids can and do form dynamically in-situ and may coarsen during creep; their availability during second stage creep as sub-micron coherent or non-coherent particles exerts important and differing effects on creep rates. Continued investigation of the role of dispersoids on the creep behaviour of aluminum casting alloys is needed to determine the principles for effective dispersoid design of aluminum for diesel engine use.

Mn has been identified as an important alloying addition to the Al-Si-Cu-Mg system to improve creep resistance [6], but its specific role in the alloys is not well identified. The present study investigates the creep micro-mechanisms and the activation energies of Al-7Si-0.3Mg-0.5Cu-0.3Mo alloys with two levels of Mn (0.17 and 0.5 wt.%). It aims at determining the influence of Mn on the type and distribution of α-Al(Fe,Mn,Mo)Si particles and their role in creep resistance. The study is based on electron microscopy analyses of creep-tested samples with the purpose of understanding the influence of the dispersoids on creep mechanisms. A comparison of calculated activation energies based on microstructural observations and the apparent activation energy obtained from the creep-tested specimens is used to identify the rate-controlling creep deformation mechanism.

A review of dislocation-creep mechanisms and activation energies in aluminum alloys is given

elsewhere [6], and an overview on recovery processes that occur during creep and the activation energies related to the interaction of dispersoids with recovery is provided in Appendix A at the end of this article to provide a background to the analyses.

## 5.2 Experimental procedures

Two alloys, Al-7Si-0.3Mg-0.5Cu-0.15Mn-0.3Mo (MG3-1) and Al-7Si-0.3Mg-0.5Cu-0.5Mn-0.3Mo (MG4-1), were prepared from a set of master alloys (Al-33 wt.% Cu, Al-10 wt.% Mo and Al-25 wt.% Mn) and melted in a silicon carbide crucible at 760 °C using a high frequency NORAX (Canada) induction furnace. The alloys were modified with 150 ppm Sr in the form of a master alloy (Al-10 wt.% Sr) to modify the eutectic Si morphology. After 3 minutes of degassing with high purity argon gas at flow rate of 1 L/min, the melt was poured at 730 °C into a constrained-rod casting mold preheated to 400 °C. The chemical composition of the alloys (Table 5.1) was determined by the Inductively Coupled Plasma-Optical Emission Spectroscopy (ICP-OES) technique on a Thermo Instruments (manufactured in the UK) ICAP 6700 Dual View ICP-OES.

*Table 5.1. Chemical compositions of the alloys.*

| **Alloy** | **Chemical Composition (wt.%)** | | | | | | | | |
|---|---|---|---|---|---|---|---|---|---|
| | Si | Mg | Cu | Fe | Ti | Mo | Mn | Sr | Al |
| **MG3-1** | 6.16 | 0.31 | 0.50 | 0.11 | 0.10 | 0.37 | 0.17 | 0.014 | Bal. |
| **MG4-1** | 6.19 | 0.32 | 0.52 | 0.11 | 0.10 | 0.33 | 0.53 | 0.014 | Bal. |

One rod extracted from each casting was machined according to the ASTM E8 to produce tensile creep test specimens. Samples were solutionized for 4 hours at 500 °C and 10 hours at 540 °C (to avoid probable incipient melting) in an electrically heated, air-circulating (Blue-M) chamber

furnace. Each sample was quenched in water at room temperature followed by an ageing at 200 °C for 5 hours (T7). Tensile creep testing was performed three times for each temperature (300, 325 and 350 °C) at 28 MPa to demonstrate the reproducibility of results. The creep tests were carried out at a constant load of 36 lb on a series ATS (Applied Test Systems) 2320-MM Lever Arm Tester. The temperature was monitored using a thermocouple with an error of ± 0.1 °C attached to the specimen while the gauge length displacement was measured with two high precision extensometers with a resolution of 5 μm. All tests were conducted in air along with a soak of 100 hours at 300 °C prior to testing. Each test was repeated three times.

A microstructural study was performed on as-cast and T7 alloy samples that were taken from the middle of the machined cylinders and cut with a low-speed diamond saw blade in order to avoid any additional heat or stress on the samples; they were ground with a series of SiC papers. Samples were initially polished with an $Al_2O_3$ solution on a porous neoprene polishing cloth and finished with colloidal silica solution using a Buehler vibratory polisher. This process follows the original method of our previous studies [50]. A Hitachi SU-3500 Variable Pressure–SEM (Scanning electron microscopy) was used at 15kV to examine the elemental analysis and surface morphology. Cylindrical samples, 50 mm in gauge length and 12.7 mm in diameter, for creep tests were machined from cylindrical bars following the ASTM E8 standard. Quenched samples were rapidly immersed in water at the end of the creep test to observe the changes caused in the microstructure by the rapid cooling. TEM (transmission electron microscopy) analyses were performed on specimens in quenched and non-quenched creep samples that were obtained from thin sections of 1 cm in the fracture area using a low speed cutter with a diamond blade in order to avoid any additional heat or stress on the samples. SiC paper with grit sizes of 400 and 600 immersed in water was used to reduce their thickness to approximately 0.1 mm. Subsequently, Precision Ion

Polishing System (PIPS) was employed for thinning and polishing the aluminum samples. A Philips CM200 microscope operated at 200 kV was used to determine the dislocation-dispersoid interactions and the creep mechanisms.

Samples for Electron Backscatter Diffraction (EBSD) analyses were ground to 800 grit using silicon carbide papers and subsequently polished using 0.03-μm colloidal silica for 6 h. EBSD analyses were conducted on specimens of 0.5 cm thick using a Hitachi SU-3500 Variable Pressure–SEM at 20 kV and 70 spot intensity. Image quality maps were constructed from step size 1 and a speed of acquisition of 67 Hz. Orientation maps were examined with Atex software. Misorientations <15° and >15° were considered sub-grain and recrystallized grain boundaries, respectively. Area measurement on ImageJ was used to measure the sub-grain sizes and particle sizes.

## 5.3 Results

### 5.3.1 Simulation of Phase Selection and Microstructural Investigation

*As-Cast MG3-1 and MG4-1*

Non-equilibrium (Scheil) and equilibrium simulations were carried out to predict reactions, phases present, and their amount in the MG3-1 and MG4-1 alloys by using the FactSage software (with FTlight database). The results of the simulations were then compared to microstructural characterization using SEM/EDS (energy dispersive X-ray spectroscopy).

*Phase Selection in MG3-1 and MG4-1 alloys:*

Non-equilibrium Scheil calculation in the MG3-1 alloy (Fig. 5.1a) indicated that α-Al is the first phase to solidify at 614 °C accompanied by the formation of $\alpha_{MG3\text{-}1}$-Al(Fe,Mo,Mn)Si at 576 °C.

Subsequently, Al-Si phase forms at 574 °C and π-$Al_8FeMg_3Si_6$ phase at 553 °C. Solidification ends with the formation of Q-$Al_5Cu_2Mg_8Si_6$ at 542 °C and θ-$Al_2Cu$ phase at 512 °C.

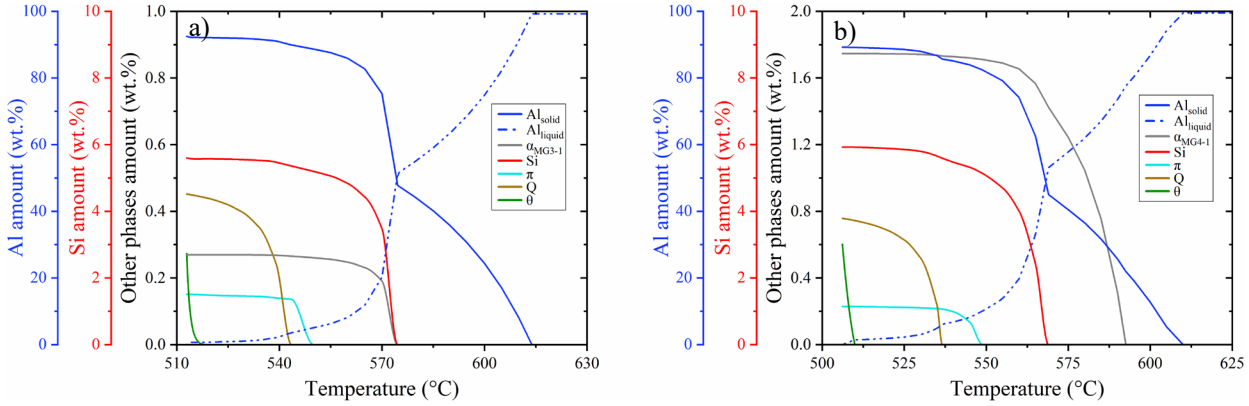


*Figure 5.1. Scheil cooling of (a) MG3-1 and (b) MG4-1 alloys as a function of temperature.*

In the MG4-1 alloy (Fig. 5.1b), solidification starts at 609 °C with the precipitation of the α-Al phase followed by the formation of $\alpha_{MG4\text{-}1}$-Al(Fe,Mo,Mn)Si phase at 590 °C. The solidification continues with the formation of a eutectic α-Al and Si microconstituent at 565 °C. With a further decrease in temperature, solidification proceeds with the development of the π-$Al_8FeMg_3Si_6$ phase at 545 °C and Q-$Al_5Cu_2Mg_8Si_6$ phase at 535 °C. Solidification terminates at 506 °C with the formation of the θ-$Al_2Cu$ phase. Table 5.2 illustrates the different reactions that occur during non-equilibrium solidification.

A comparison between these simulations indicates that the higher concentration of Mn in the MG4-1 alloy decreases the solidification temperature of α-Al (9 °C), Al-Si (9 °C), π-$Al_8FeMg_3Si_6$ (8 °C), Q-$Al_5Cu_2Mg_8Si_6$ (7 °C), and θ-$Al_2Cu$ (6 °C) phases but increases the precipitation temperature of $\alpha_{MG4\text{-}1}$-Al(Fe,Mo,Mn)Si phase (14 °C). The increase in the precipitation temperature in the $\alpha_{MG4\text{-}1}$-phase shows that the phase becomes more stable due to the incorporation of a higher amount of Mn. It has been reported that Al-transition metals form covalent bonds that have thermally

stabilized the $\alpha_{MG4-1}$-Al(Fe,Mo,Mn)Si phase [7]. The simulations also show that all phases, except α-Al, increase their weight percentage with the increase in Mn (Table 5.2).

*Table 5.2. Reactions and phase amount (at the end of the solidification) in the MG3-1 and MG4-1 alloys.*

| **MG3-1 alloy** | | | **MG4-1 alloy** | | |
|---|---|---|---|---|---|
| **Reaction** | **Scheil (°C)** | **Amount (wt.%) at 512 °C** | **Reaction** | **Scheil (°C)** | **Amount (wt.%) at 506 °C** |
| L➔α-Al | 614 | 92.58 | L➔α-Al | 609 | 89.85 |
| L➔α-Al+$\alpha_{MG3-1}$ | 576 | 0.28 | L➔α-Al+$\alpha_{MG4-1}$ | 590 | 1.78 |
| L➔α-Al+$\alpha_{MG3-1}$+Si | 574 | 5.65 | L➔α-Al+$\alpha_{MG4-1}$+Si | 565 | 5.97 |
| L➔α-Al+$\alpha_{MG3-1}$+Si+π | 550 | 0.16 | L➔α-Al+$\alpha_{MG4-1}$+Si+π | 545 | 0.26 |
| L➔α-Al+$\alpha_{MG3-1}$+Si+π+Q | 542 | 0.45 | L➔α-Al+$\alpha_{MG4-1}$+Si+π+Q | 535 | 0.78 |
| L➔α-Al+$\alpha_{MG3-1}$+Si+π+Q+θ | 512 | 0.27 | L➔α-Al+$\alpha_{MG4-1}$+Si+π+Q+θ | 506 | 0.64 |

*Microstructures of As-Cast Alloy:*

SEM BSE (Back scattered electron) micrographs of the MG3-1 and MG4-1 alloys in the as-cast condition are presented in Fig. 5.2. There are many similarities in the microstructures of the two alloys. Sr addition led to the presence of a fine and fibrous Si phase. The precipitates were identified via EDS analyses with the guidance of thermodynamic predictions. Al-Cu-Mg-Si phase appears as dark-gray and with a Chinese-script morphology and is labeled as Q-$Al_5Cu_2Mg_8Si_6$. The bright-white Al-Cu phase with a blocky morphology is identified as θ-$Al_2Cu$. Mo and Mn bearing phase with a blocky morphology appears as light-gray and is identified as $\alpha_{MG3-1}$-Al(Mn,Mo,Fe)Si intermetallic phase. Thermodynamic calculations, EDS elemental mapping, and EDS point-scan analysis correlate well with the experimental analyses. Al-Fe-Mg-Si phase (π-$Al_8FeMg_3Si_6$ phase) predicted by FactSage was not observed in the SEM/EDS. As previously

reported [6], π-phase is suppressed because the 0.1% Fe in the alloy is consumed for the formation of $\alpha_{MG3\text{-}1}$-phase.

There are also differences in the microstructures of the two alloys. The average particle size is 12.6 μm for Q and 10.1 μm for θ in MG3-1 alloy while 4.9 μm for Q and 6.7 μm for θ in MG4-1 alloy. Therefore, the Q-$Al_5Cu_2Mg_8Si_6$ and θ-$Al_2Cu$ phases in MG4-1 are more refined than those in MG3-1. It is seen in the SEM BSE images of Fig 5.2 that the Q and θ phases are closely associated with the α-Al(Mn,Mo,Fe)Si dispersoids. In this study the term precipitate is used for those phase particles that take part in ageing sequence such as those in T6 or T7 precipitation (e.g. Q and theta phases) and the dispersoids for those that are not a part of the precipitation ageing sequence (eg. iron silicides). As the thermodynamic calculations indicate (Table 5.2), the Q and the θ phases co-form with the α-Al(Mn,Mo,Fe)Si dispersoids. As the amount of the dispersoids increased while the amounts of other phases remained constant, the co-nucleation of the Q and the θ with the dispersoids results in the dispersion and the refinement of the Q and θ phases.

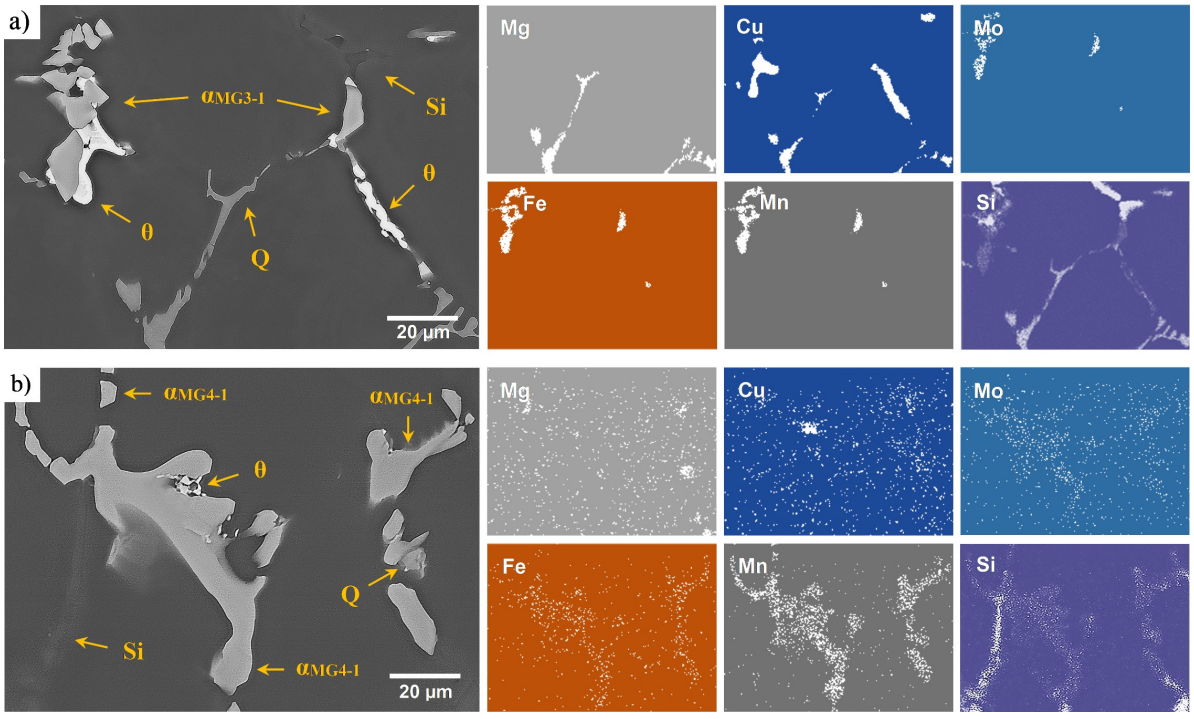

*Figure 5.2. Backscattered SEM of the as-cast microstructures along with EDS mapping of (a) MG3-1 and (b) MG4-1 alloys.*

Fig. 5.3 shows the deep-etched microstructures and EBSD images of MG3-1 and MG4-1 alloys indicating the eutectic Si morphology and grain structure in the as cast condition. It is noted that the Si coral "globes" appear slightly more dispersed in MG3-1 compared to the MG4-1 alloy (Fig. 3a, c). Si coral rods on the other hand are slightly more refined in MG3-1 than in the MG4-1 (Figs. 3b, d). The thermodynamic calculations indicate that the amount of dispersoids increased by 400 wt.% in the MG4-1 alloy compared to the MG3-1 at the end of solidification (Fig. 5.1), and the amounts of the other phases increased by a lesser amount (Si by 5 wt.%, θ by 35 wt.%, Q by 94 wt.%). The thermodynamic calculations also indicate that the Si co-forms with the dispersoids.

The significant increase in the amount of the dispersoids in the MG4-1 alloy has likely led to the dispersed nucleation of the Si coral globes. Both alloys are modified with 140 ppm of Sr, but the eutectic Si in the MG4-1 is slightly coarser than the eutectic Si in MG3-1 (0.47 μm vs 0.62 μm); the increased amount of Si in the MG4-1 would require a slightly increased amount of Sr for morphological refinement. Figs. 3e, f present the EBSD images revealing the as-cast grain structure and the Si distribution in the as-cast alloy. The as-cast grain sizes are 270 μm for MG3-1 and 102 μm for MG4-1.

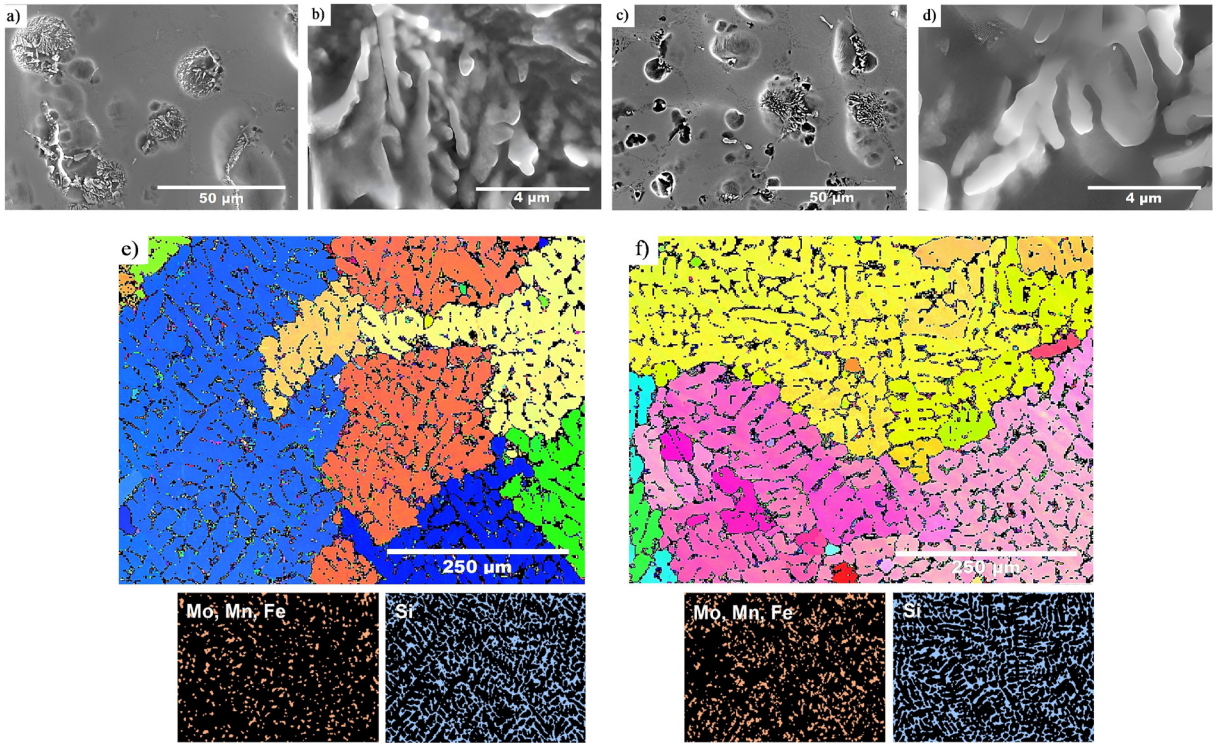


*Figure 5.3. Deep-etched microstructures showing the eutectic Si in (a, b) MG3-1 and (c, d) MG4-1. EBSD images of (e) MG3-1 and (f) MG4-1 showing the as-cast grain structure and Si distribution.*

### 5.3.2 Phase Selection and Microstructures of (T7) Overaged Alloys

*Phase Selection in MG3-1 and MG4-1 alloys:*

Equilibrium calculations were carried out to estimate the type and amounts of precipitates in the MG3-1 and MG4-1 alloys in the T7 condition (solutionized at 500 °C and 540 °C followed by overaging at 200 °C), as indicated in Fig. 5.4. The simulations indicate that when the solution treatment is performed (at 540 °C as the highest temperature), certain phases are dissolved and only α-Al(Fe,Mo,Mn)Si and the eutectic Si phases remain. The calculations show that the MG4-1 alloy with the higher Mn has a higher amount of $\alpha_{MG4\text{-}1}$-Al(Mn,Mo,Fe)Si phase, although no effect is seen on the other phases.

The precipitates present at the overaging temperature (200 °C) and their amounts were predicted via the equilibrium calculation at 200 °C (Table 5.3). The equilibrium phase selection in the MG3-1 and MG4-1 alloys is predicted to be Si, π, Q, and θ phases that remained constant in amount while the $\alpha_{MG3\text{-}1}$-phase increased in amount significantly (Table 5.3). Because π transforms to $\alpha_{MG3\text{-}1}$ and $\alpha_{MG4\text{-}1}$, the total amount of these phases is predicted as 1.43% and 2.6%, respectively.

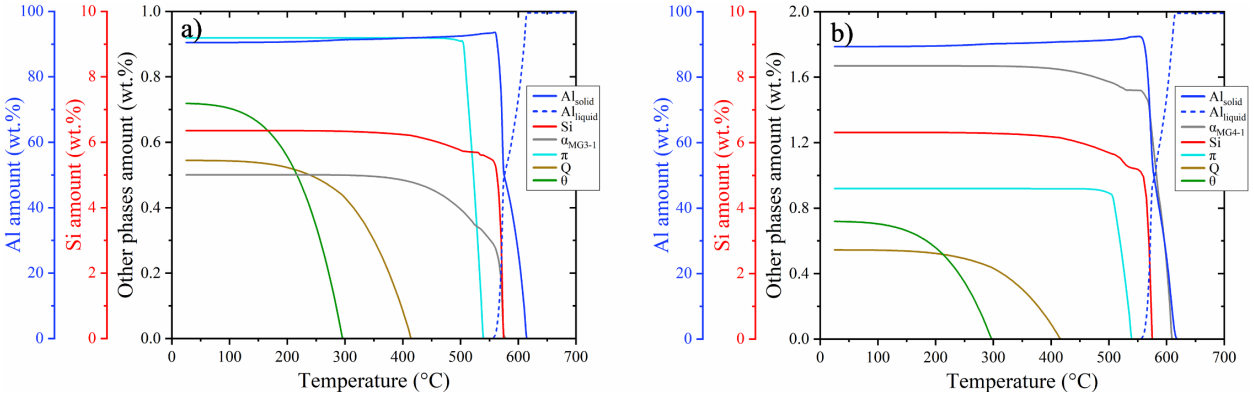


*Figure 5.4. Calculated equilibrium phase selection of (a) MG3-1 and (b) MG4-1 alloys versus temperature.*

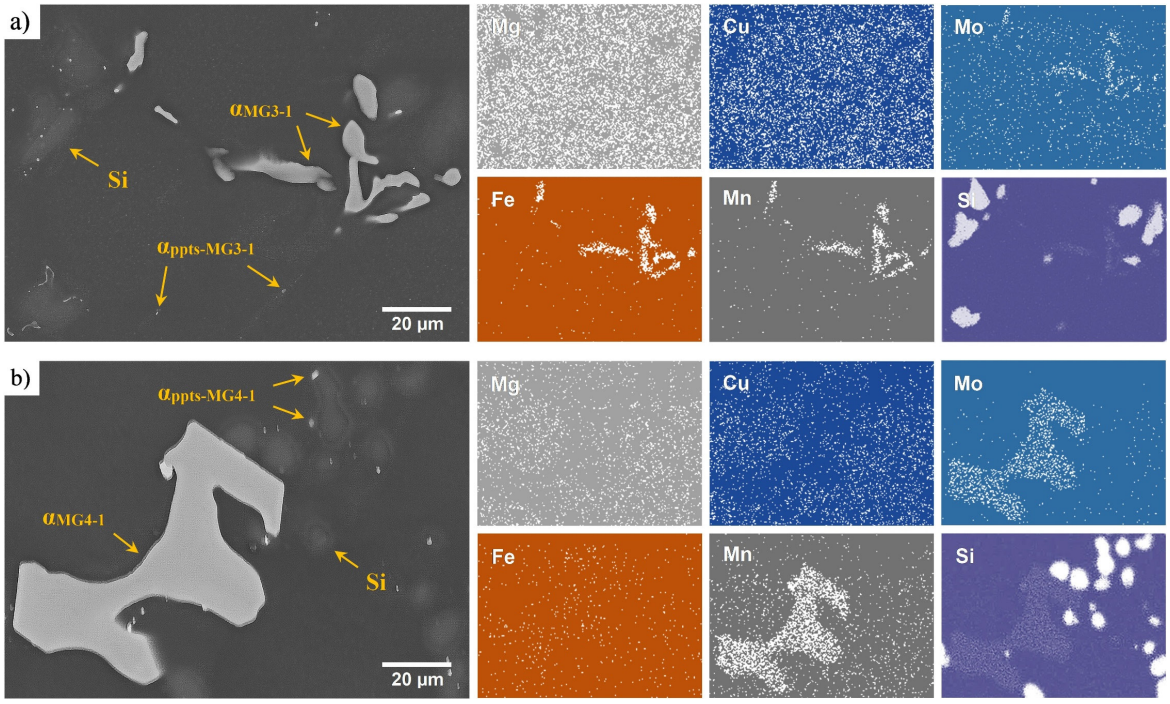

*Figure 5.5. BSE image of the T7 alloys along with EDS mapping of (a) MG3-1 and (b) MG4-1 alloys.*

*Table 5.3. Equilibrium phases and their amounts in the MG3-1 and MG4-1 alloys at 300, 200 and 25 °C.*

| **MG3-1 alloy** | | **MG4-1 alloy** | |
|---|---|---|---|
| **Phases present and amounts (wt.%)** | **Temp (°C)** | **Phases present and amounts** | **Temp (°C)** |
| 93% α-Al, 0.33% $\alpha_{MG3-1}$, 5.6% Si | 540 | 93% α-Al, 1.5% $\alpha_{MG4-1}$, 5.2% Si | 540 |
| 92% α-Al, 0.40% $\alpha_{MG3-1}$, 5.7% Si, 0.91% π | 500 | 92% α-Al, 1.6% $\alpha_{MG4-1}$, 5.7% Si, 0.89% π | 500 |
| 91% α-Al, 0.50% $\alpha_{MG3-1}$, 6.3% Si, 0.92% π, 0.43% Q | 300 | 90% α-Al, 1.7%$\alpha_{MG4-1}$, 6.3% Si, 0.92% π, 0.43% Q | 300 |
| 91% α-Al, 0.51% $\alpha_{MG3-1}$, 6.3% Si, 0.92% π, 0.52% Q, 0.56% θ | 200 | 90% α-Al, 1.7% $\alpha_{MG4-1}$, 6.3% Si, 0.92% π, 0.52% Q, 0.56% θ | 200 |
| 90% α-Al, 0.50% $\alpha_{MG3-1}$, 6.3% Si, 0.92% π, 0.55% Q, 0.71% θ | 25 | 90% α-Al, 1.7% $\alpha_{MG4-1}$, 6.3% Si, 0.92% π, 0.55% Q, 0.71% θ | 25 |
| 90% α-Al, 0.50% $\alpha_{MG3-1}$, 6.3% Si, 0.92% π, 0.55% Q, 0.71% θ | 25 | 90% α-Al, 1.7% $\alpha_{MG4-1}$, 6.3% Si, 0.92% π, 0.55% Q, 0.71% θ | 25 |

### 5.3.3 Creep Behavior and Creep Activation Energy

The region where creep is observed in the cylinder head is the inter-valve zone that heats to a peak temperature of ~285–300 °C when the engine heats up [3]. At this temperature, the material tries to expand but cannot, due to the geometric constraint of the inter-valve zone and is placed under compressive creep loading. Creep rates in tensile creep are either the same as in compressive creep or are approximately one order of magnitude higher [3]. Compressive creep tests are forgiving to the casting defects such as porosity, brittle phases and crack formation at stress risers; they therefore tend to overestimate the creep resistance. The authors have been conducting tensile creep

rather than compressive creeps in their recent studies with the knowledge that the creep rates would be similar or higher in compressive loading [3,6].

The temperature range investigated for creep deformation in this study is from 300 °C to 350 °C. Simulations of the diesel engine has shown that the cylinder head heats up to 345–365 °C during operation [8]. It is important to investigate these high temperatures because as we approach 350 °C the creep mechanism may start to change, especially if the recrystallization temperature is reached and the creep resistance decreases.

Tensile creep tests were conducted on the MG3-1 and MG4-1 alloys at 300, 325, and 350 °C with a constant creep stress of 28 MPa (Fig. 5.6). The specimens were exposed to a soaking of 100 hours at 300 °C prior to creep testing to avoid in-situ coarsening of dispersoids and to stabilize the microstructure. Time-to-fracture decreased, and creep rate increased with temperature in both alloys (Fig. 5.6). The creep curves indicated that the addition of Mn to the MG4-1 alloy improved the creep time-to-fracture over the MG3-1 alloy by 200% at 300 °C, 262% at 325 °C, and 19% at 350 °C (Table 5.4).

Plots of creep rate versus time are shown in Appendix B (Fig. 5.B1). Minimum creep rates were determined from these plots. Steady state creep rates were also determined calculating the slope of the straight line between two points in Stage II creep in the creep strain vs time curves (Fig. 5.6). Both values are shown in Table 5.4. Compared to the MG3-1, the steady state creep rate in MG4-1 decreased by 71% at 300 °C, 18% at 325 °C, and 36 % at 350 °C (Table 5.4). The maximum creep strain was ~22% in MG3-1 and ~13% in MG4-1.

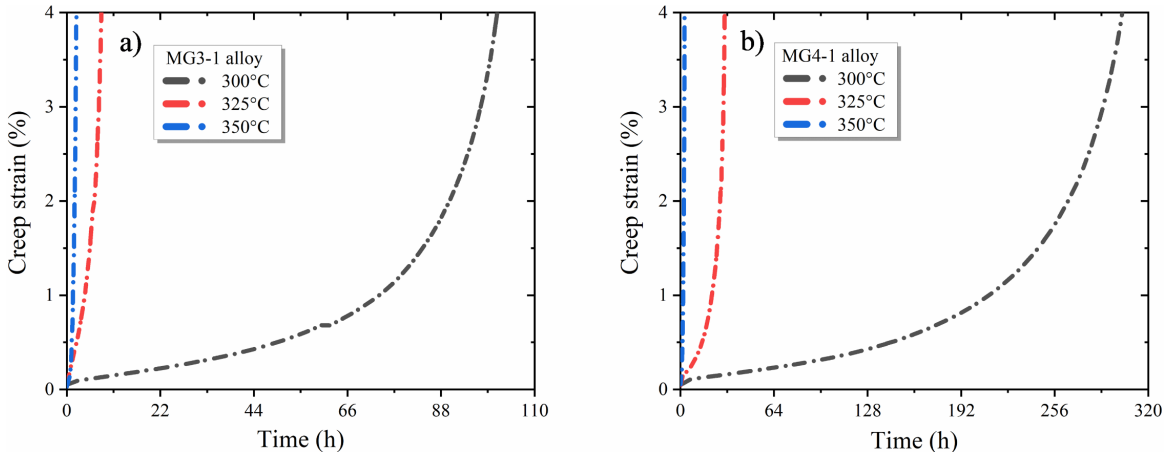


*Figure 5.6. Tensile creep test vs time under a creep stress of 28 MPa at 300 °C, 325 °C, and 350 °C for (a) MG3-1 alloy and (b) MG4-1.*

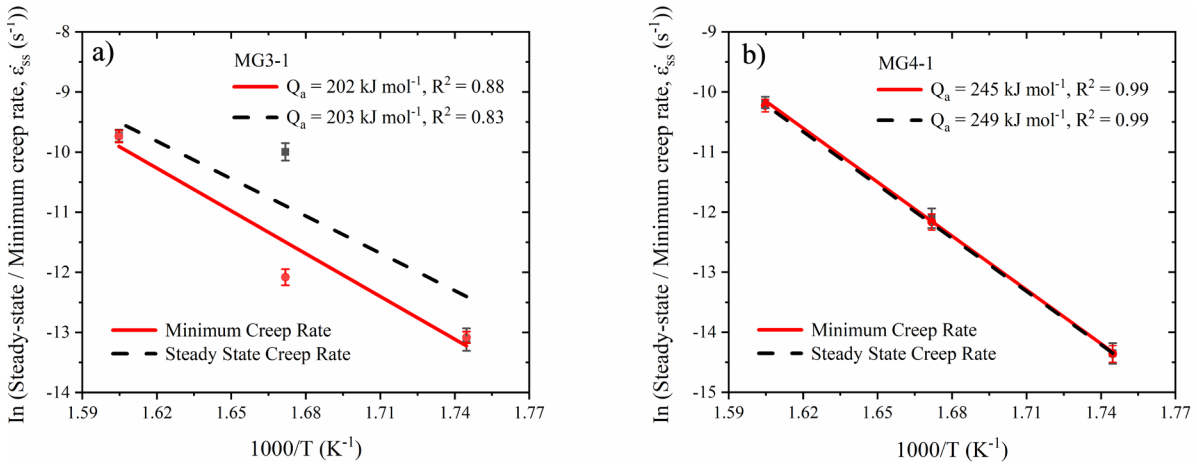


*Figure 5.7. Arrhenius plot of log of steady-state creep rate vs the reciprocal temperature and minimum creep rate versus reciprocal temperature with standard deviation obtained from Fig. B1 (Appendix B) at 28 MPa for (a) MG3-1 and (b) MG4-1 alloys.*

The apparent activation energy $Q_a = -R\left[\frac{\partial\, In\, \dot{\varepsilon}_{ss}}{\partial\left(\frac{1}{T}\right)}\right]_{\sigma}$ was determined from Arrhenius plots of ln $\dot{\varepsilon}_{ss}$ versus $1000/T$ at a constant stress. Both steady-state creep rates and minimum creep rates were

used (Fig. 5.7). The $Q_a$ calculated for the MG3-1 and MG4-1 alloys at temperatures of 300−350 °C and 28 MPa are shown in Fig. 5.7. As illustrated in Fig. 5.7, the value of the apparent activation energy for MG4-1 is higher than that for MG3-1. Due to the difficulty in establishing an exact balance of strain hardening and softening for stage II creep data, it is seen that minimum creep rates give a better fit to data with an improved $R^2$ of 0.88 instead of 0.83 for MG3-1.

*Table 5.4. Creep features for MG3-1 and MG4-1 at 300, 325, and 350 °C under 28 MPa.*

| **Creep parameters** | **MG3-1 alloy** | | | **MG4-1 alloy** | | |
|---|---|---|---|---|---|---|
| | **300 °C** | **325 °C** | **350 °C** | **300 °C** | **325 °C** | **350 °C** |
| **Creep time-to-fracture (h)** | 106 | 8.5 | 2.6 | 321 | 30.8 | 3.1 |
| **Steady state creep rate ($s^{-1}$)** | $2.01x10^{-6}$ | $5.54x10^{-6}$ | $5.96x10^{-5}$ | $5.84x10^{-7}$ | $4.56x10^{-6}$ | $3.81x10^{-5}$ |
| **Minimum creep rate ($s^{-1}$)** | $2.08x10^{-6}$ | $5.66x10^{-6}$ | $5.89x10^{-5}$ | $5.8x10^{-7}$ | $4.72x10^{-6}$ | $3.61x10^{-5}$ |

### 5.3.4 Microstructural Investigation of Creep Tested Al-7Si-0.3Mg-0.5Cu-0.3Mo-0.15Mn (MG3-1) Alloy

*Grain Boundary Misorientation Distribution and Silicon Particles*

Fig. 5.8 presents the Electron Channeling Contrast (ECC) and Electron Back-Scatter Diffraction (EBSD) analyses showing the sub-structure in the MG3-1 alloy after creep testing at 300 °C and 28 MPa. All sub-structure was determined to be sub-grains with misorientations from 0-15°. The average sub-grain size was determined to be 14.9 μm (Fig. 5.8a).

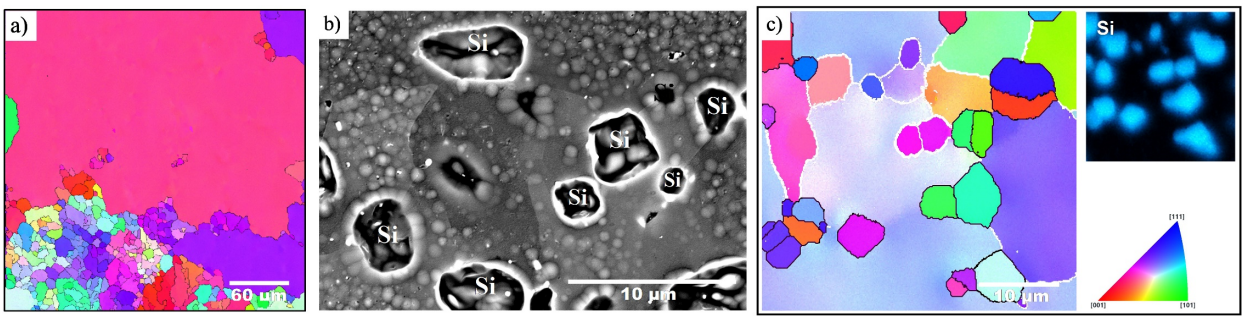


*Figure 5.8. (a, c) EBSD with inverse pole figure (IPF) coloring in the Y-direction and (b) electron channeling contrast analyses showing the grain size and silicon particles distribution after tensile creep test at 300 °C and 28 MPa in MG3-1 alloy.*

Regions with Si particles closely associated with sub-grains were also seen. Zoom-in images showing the distribution of sub-grain structures and silicon particles are presented in Figs. 5.8b, c. The misorientation angle distributions indicated that sub-grain boundaries presented misorientations <15° (white lines, sub-grain boundaries) and Si boundaries were >15° (black lines) misorientations. The origin of these Si particles in the 10-15 µm range is due to the spheroidization of the eutectic Si phase during heat treatment [9,10]. Si particles can coarsen during prolonged heating [9] through the disintegration of the Si rods of radius, r, into equidistant spheres of radius, R, via surface diffusion of Si along the Si/α-Al interface.

It is noted, however, that in the MG3-1 alloy, there is also additional Si solute that is available for Si phase coarsening due to the dissolution of a small amount of α-Al(Fe,Mo,Mn)Si dispersoids as the alloy is heated from the ageing temperature of 200 °C to the creep test temperature of 300 °C (Table 5.3). The additional Si available with the dissolution of the dispersoids would lead to the coarsening of the Si phase particles that would involve Si lattice diffusion. Silicon particles that

reach an optimal size accumulate dislocations leading to local discontinuous dynamic recovery processes and generate sub-grains.

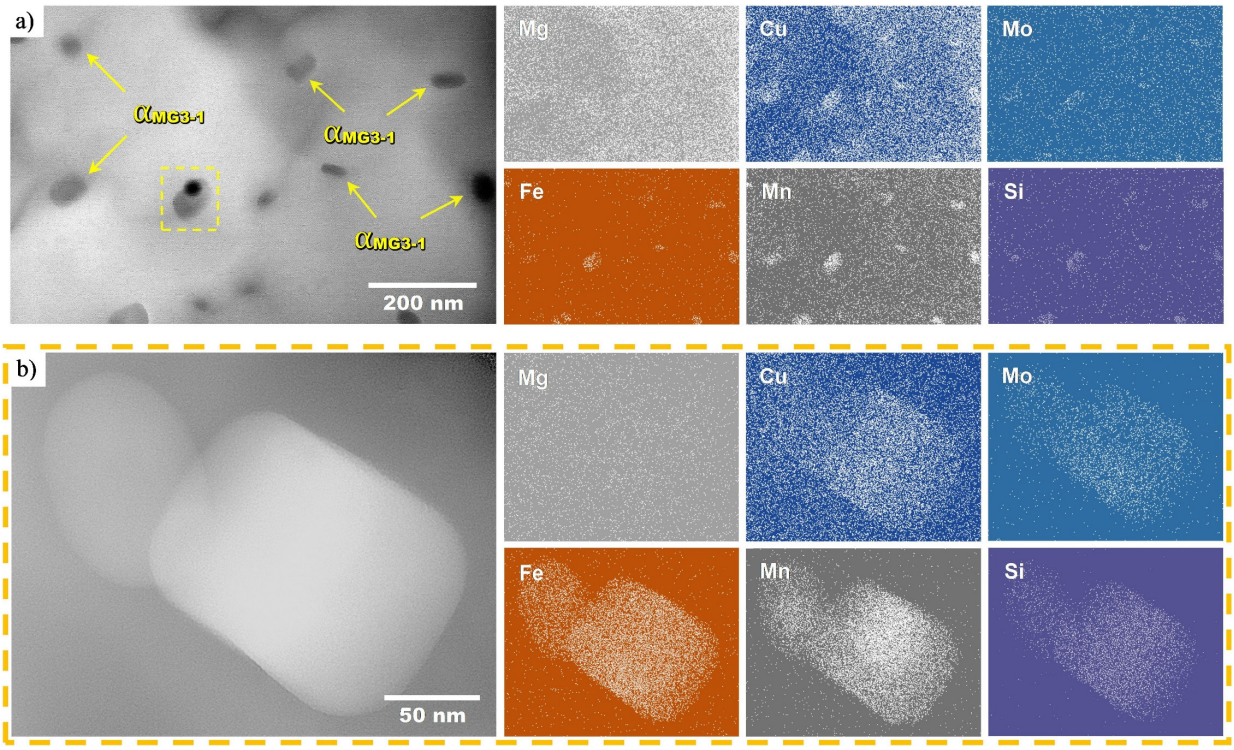


*Figure 5.9. TEM micrographs of α-Al(Fe,Mo,Mn)Si dispersoids in MG3-1 alloy after tensile creep at 300 °C and 28 MPa: (a) $\alpha_{MG3-1}$-Al(Fe,Mo,Mn)Si particles distribution with corresponding EDS maps; (b) enlarged view of $\alpha_{MG3-1}$-Al(Fe,Mo,Mn)Si dispersoids exhibiting distinct shapes with corresponding EDS maps.*

*Transmission Electron Microscopy (TEM)*

TEM images showing the $\alpha_{MG3-1}$-Al(Fe,Mo,Mn)Si dispersoids in the MG3-1 alloy after tensile creep testing at 300 °C and 28 MPa are presented in Fig. 5.9. Fig. 5.9a shows a HABF (high angle bright field) image revealing their form and distribution. The size range of the $\alpha_{MG3-1}$-dispersoids was ~50 nm to ~215 nm. The $\alpha_{MG3-1}$-dispersoids were calculated to have an average size ~135 nm

with an interparticle spacing of 263 nm. TEM-EDS maps show Q-$Al_5Cu_2Mg_8Si_6$ particles, which are closely associated with the $\alpha_{MG3\text{-}1}$-particles. This suggests that Q-precipitates and $\alpha_{MG3\text{-}1}$-dispersoids may have co-precipitated or served as co-nucleation sites, as previously observed [3].

It can be noted that smaller $\alpha_{MG3\text{-}1}$-particles exhibit rounder shapes. Fig. 5.9b shows an enlarged view from Fig. 5.9a (indicated in the square) of two $\alpha_{MG3\text{-}1}$-Al(Fe,Mo,Mn)Si dispersoids exhibiting rounded shapes 49 nm in size. EDS analysis again shows the close association of $\alpha_{MG3\text{-}1}$-Al(Fe,Mo,Mn)Si dispersoids and Q-$Al_5Mg_8Cu_2Si_6$ precipitates. The TEM-EDS analysis indicated that $\alpha_{MG3\text{-}1}$-particles contain 16.8 wt.% Fe, 4.9 wt.% Mo, 19.3 wt.% Mn, and 6.1 wt.% Si and balance Al whereas Q-particles consist of 1.4 wt.% Mg, 5.2 wt.% Cu, 6.1 wt.% Si and balance Al.

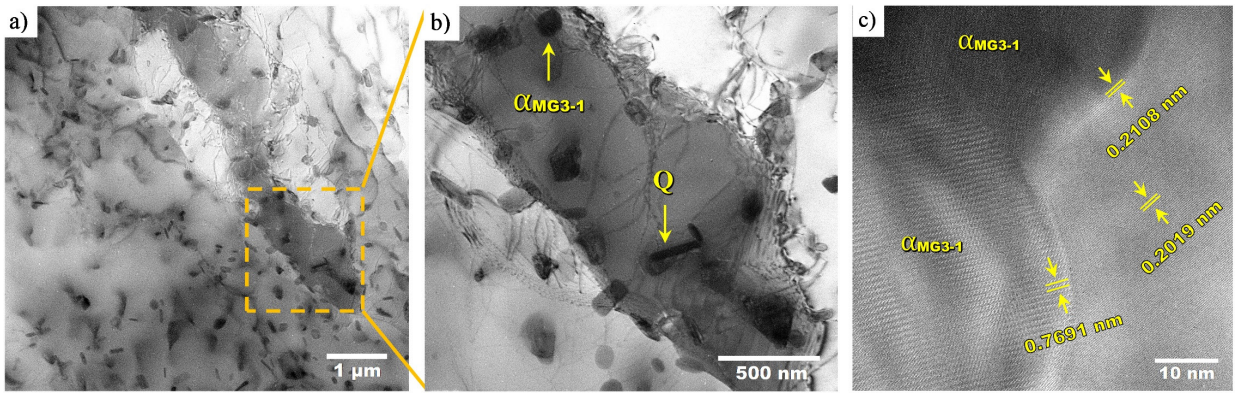


*Figure 5.10. HRTEM analysis of α-Al(Fe,Mo,Mn)Si dispersoids in MG3-1 alloy after tensile creep at 300 °C and 28 MPa: (a) $\alpha_{MG3\text{-}1}$-Al(Fe,Mn,Mo)Si dispersoid distribution in the microstructure; (b) enlarged view of an elongated grain and the interaction of $\alpha_{MG3\text{-}1}$-dispersoids with dislocations and boundaries; (c) two large $\alpha_{MG3\text{-}1}$-Al(Fe,Mn,Mo)Si dispersoids showing a coherent and incoherent interfaces with the Al matrix.*

*High Resolution Transmission Electron Microscopy (HRTEM)*

HRTEM images (Fig. 5.10) show the microstructure of the MG3-1 alloy after tensile creep testing

at 300 °C and 28 MPa. The particles were identified by TEM-EDS analysis. Fig. 5.10a shows the distribution of $\alpha_{MG3\text{-}1}$-Al(Fe,Mn,Mo)Si dispersoids and elongated sub-grains that reveals that recovery has occurred. Dislocation pile-up seen behind the sub-grain boundary indicates that this is an early stage of recovery with dislocations at the boundaries as well as inside the grains. The next step in the recovery process would be the formation of sub-grains annihilating the dislocations inside and forming ordered dislocation walls at the boundary. A zoom-in image (Fig. 5.10b) shows that the dispersoids possess a short plate morphology and that Q-$Al_5Cu_2Mg_8Si_6$ precipitates are in the form of rods (shown by the arrow). Q-precipitates do not seem to interact with dislocations or grain boundaries. The average dispersoid size at cell boundaries is ~214 nm and the inter-particle spacing is approximately 158 nm presenting a distribution similar to their bulk distribution (Fig. 5.10). The spatial distribution of $\alpha_{MG3\text{-}1}$-Al(Fe,Mn,Mo)Si particles was found to be homogeneous throughout the microstructure. Since they are coherent, and of shearable size, the dislocations and cell boundaries cut these precipitates.

Fig. 5.10c shows a high-resolution TEM (HRTEM) image of two $\alpha_{MG3\text{-}1}$-Al(Fe,Mn,Mo)Si dispersoids with particle size about 210 nm having coherent and incoherent interfaces. The incoherency, noted by the divergent angles in the lattice planes between the dispersoid and the Al matrix, may be attributed to the passage of dislocations through the dispersoid (Fig. 5.10c). The semi-coherent α-dispersoid has an inter-planar spacing ~ 0.2108 nm and a continuous interface along the Al matrix with 4.2% mismatch coherency strain. The volume fraction of the dispersoids in MG3-1 was 0.11.

### 5.3.5 Microstructural Investigation of Creep Tested Al-7Si-0.3Mg-0.5Cu-0.3Mo-0.5Mn (MG4-1) Alloy

*Grain Boundary Misorientation Distribution and Silicon Particles*

ECC and EBSD analyses showing the grain and sub-grain structures along with an IPF-Y color map for the MG4-1 alloy after tensile creep testing at 300 °C and 28 MPa are presented in Fig. 5.11. Fig. 5.11a is an enlarged view of the distribution of sub-grains with misorientations between 3° and 8° that formed because of restoration processes in MG4-1 during creep testing. The analysis showed that 95% of the substructure was sub-grain with misorientation < 15°. As illustrated, finer and higher density sub-grains are observed in MG4-1 compared to the MG3-1; an average subgrain size of 1.2 μm was determined in MG4-1 compared to 14.9 μm in MG3-1. Fig. 5.11c shows fine silicon particles that exist in the region where subgrains are found. The silicon particles have high angle boundaries with misorientations >15° and are represented with dark boundary lines in Fig. 5.11b. Sub-grains with misorientation <15° are found with close association with the silicon phase particles.

The Si particles are 2-10 μm and are smaller than those seen in MG3-1. It was reported [9] that the size of spheroidized Si after heat treatment has a relationship to the eutectic Si coral-rod diameter in the as-cast alloy; for equal coarsening time, $t$, same temperature, $T$, and similar surface diffusion coefficient, $D$, the radius, $R$, of the coarsened spheres is a function of the as-cast Si rod radius, $r$, i.e. $R = f(r)$. The study indicated that the MG4-1 has larger Si rod radius, $r$, than MG3-1 but has a larger spheroidized Si radius $R$. FactSage calculations (Table 5.3) reveal that unlike the MG3-1 alloy, the dispersoids in MG4-1 are thermally stable and retained their strengthening effect as the temperature is increased from the ageing temperature of 200 °C to the creep temperature of 300 °C. The MG4-1 alloy, unlike MG3-1, does not have additional Si solute that contributes to the coarsening of the spheroidized Si. The finer Si particles lead to a dispersed accumulation of dislocations leading to the formation of smaller sub-grains in MG4-1.

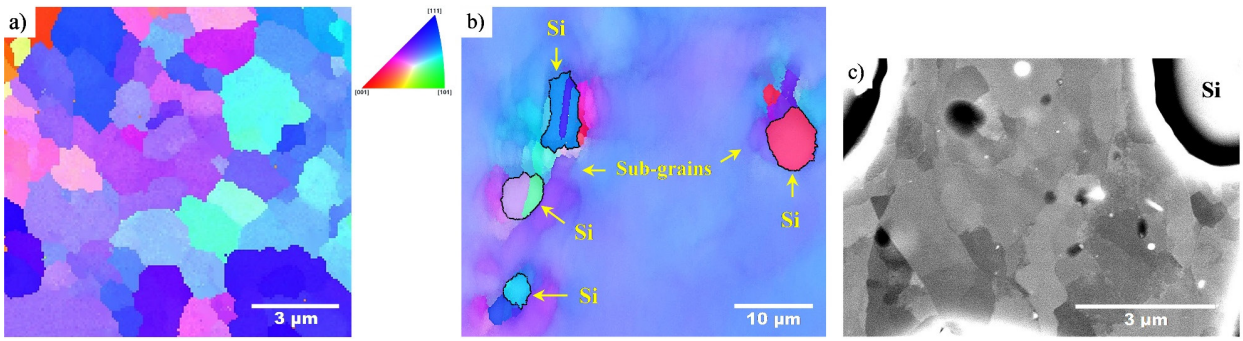


*Figure 5.11. (a, b) Orientation maps with IPF coloring in the Y-direction and (c) electron channeling contrast after tensile creep test at 300 °C and 28 MPa of MG4-1 alloy.*

*Transmission Electron Microscopy (TEM)*

A dark field TEM image showing the form and distribution of distinct particles in the MG4-1 alloy after tensile creep testing at 300 °C and 28 MPa is presented in Fig. 5.12. EDS maps combined with thermodynamic predictions indicated the presence of $\alpha_{MG4\text{-}1}$-Al(Fe,Mo,Mn)Si, Q-$Al_5Cu_2Mg_8Si_6$, and eutectic Si phases in the microstructure. TEM-EDS analysis indicates that the composition of the $\alpha_{MG4\text{-}1}$-Al(Fe,Mo,Mn)Si dispersoids is 17.9 wt.% Fe, 5.1 wt.% Mo, 22.7 wt.% Mn, 6.9 wt.% Si, and 47 wt.% Al.

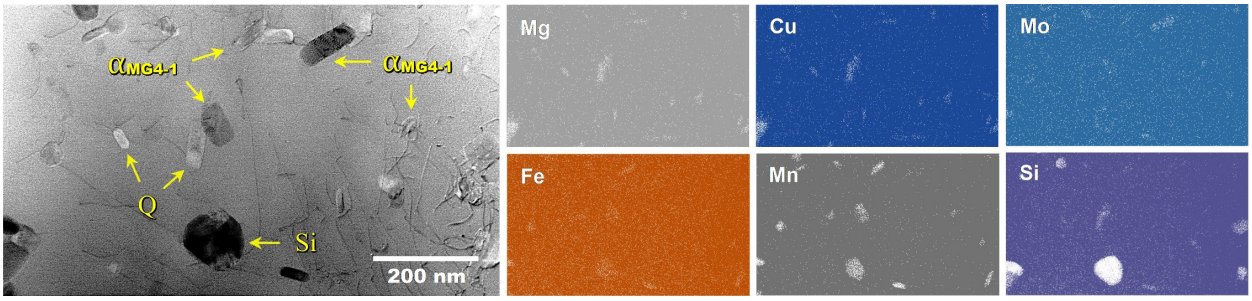


*Figure 5.12. TEM micrographs of $\alpha_{MG4\text{-}1}$-Al(Fe,Mo,Mn)Si, Q-$Al_5Cu_2Mg_8Si_6$ and the eutectic Si particles in the MG4-1 alloy after tensile creep at 300 °C and 28 MPa showing the particle distribution with corresponding EDS maps.*

The particles size of $\alpha_{MG4\text{-}1}$-dispersoids was calculated to be 149 nm. However, smaller particles were also detected having a diameter of 102 nm. It is noted that the distribution of nano-sized $\alpha_{MG4\text{-}1}$-dispersoids was enhanced with the increased level of Mn reducing the particle spacing. The amount of Q-precipitates was relatively the same as its amount in the MG3-1 alloy; the Q phase seems to have served as precipitation center for nano-sized $\alpha_{MG4\text{-}1}$-dispersoids.

*High Resolution Transmission Electron Microscopy (HRTEM)*

HRTEM images showing the form and distribution of $\alpha_{MG4\text{-}1}$-Al(Fe,Mn,Mo)Si dispersoids after tensile creep testing MG4-1 at 300 °C and 28 MPa are presented in Fig. 5.13. Fig. 5.13a indicates that softening processes occurred with the appearance of sub-grains. Sub-grains appeared in the alloy together with nano-sized $\alpha_{MG4\text{-}1}$-dispersoids showing pining interaction with grain boundaries. Fig. 5.13b presents an enlarged view of the region indicated with a square. Nano-size $\alpha_{MG4\text{-}1}$-dispersoids (indicated with arrows) were seen attached to a large $\alpha_{MG4\text{-}1}$-particle (~290 nm). As illustrated, the dislocations seem stretched when they interact with the fine dispersoids suggesting that nano-size $\alpha_{MG4\text{-}1}$-dispersoids impede dislocation motion. Additional $\alpha_{MG4\text{-}1}$-particles of different sizes are found in the micrograph attributed to the increased Mn level in MG4-1.

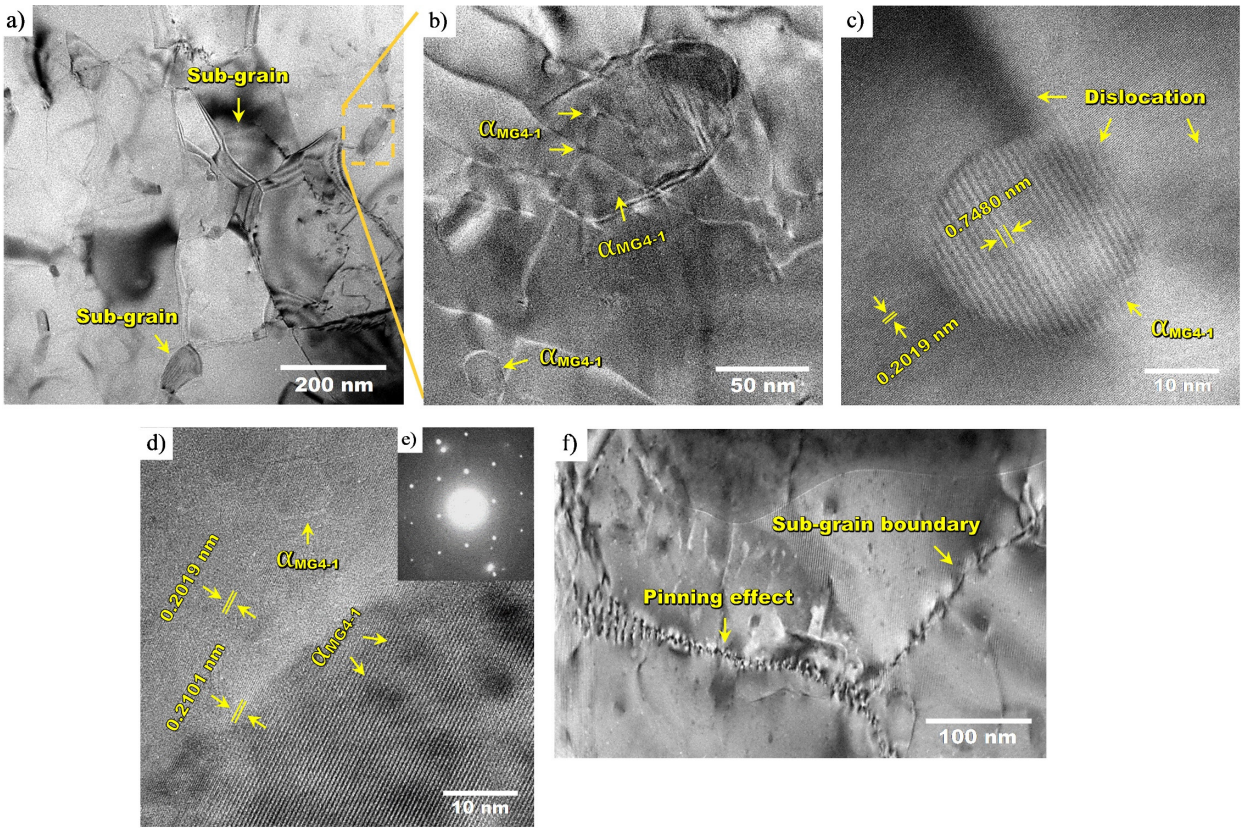


*Figure 5.13. HRTEM images of α $_{MG4-1}$-Al(Fe,Mo,Mn)Si dispersoids, dislocations and grains boundaries in MG4-1 alloy after tensile creep test at 300 °C and 28 MPa: (a) $\alpha_{MG4-1}$-Al(Fe,Mn,Mo)Si dispersoids distribution in the microstructure with sub-grain formation; (b) enlarged view of the interaction of nano-sized $\alpha_{MG4-1}$-dispersoids with dislocations; (c) dislocation passing through a $\alpha_{MG4-1}$-dispersoid (28 nm) making it incoherent; (d) semi-coherent large $\alpha_{MG4-1}$-dispersoid (~150 nm) and fully coherent nano-scale $\alpha_{MG4-1}$-dipersoid (~6 nm); (e) diffraction pattern of $\alpha_{MG4-1}$-dispersoids (small dots) distributed around an Al matrix grain (large dot); (f) interaction of $\alpha_{MG4-1}$-Al(Fe,Mo,Mn)Si dispersoids with sub-grain boundaries.*

Fig. 5.13c reveals how a dispersoid, with a particle size of 28 nm, has become incoherent due to interaction with dislocations. Here, the contrast lines (lattice planes) of the dispersoids exhibit different directions in comparison to the lines in the Al matrix. Fig. 5.13d shows a semi-coherent

interface of a large $\alpha_{MG4\text{-}1}$-dispersoid (~180 nm) and a full coherency of nano-sized $\alpha_{MG4\text{-}1}$-dispersoids (~6 nm) with the Al matrix. As can be seen, the contrast lines of large and nano-size $\alpha_{MG4\text{-}1}$-Al(Fe,Mo,Mn)Si particles are continuous with the lines to the Al matrix. However, a decrease in coherency is seen when the particle size increases. The coherency was determined from the calculation of the interplanar spacing mismatches between aluminum matrix/nano-size $\alpha_{MG4\text{-}1}$-particles (0.2019 nm) and the interface of large $\alpha_{MG4\text{-}1}$-particles (0.2101 nm), resulting in a 3.9% mismatch. At high magnification, TEM micrograph confirmed the presence of fine $\alpha_{MG4\text{-}1}$-particles attached to large $\alpha_{MG4\text{-}1}$-particles. The nano-size $\alpha_{MG4\text{-}1}$-Al(Fe,Mo,Mn)Si dispersoids show a morphology similar to nano-sized α-Al(Fe,Cr,Mn)Si dispersoids [6]. Fig. 5.13e shows the selected area electron diffraction (SAED) pattern of $\alpha_{MG4\text{-}1}$-dispersoids (small dots) distributed around an Al matrix grain (large dot). The $\alpha_{MG4\text{-}1}$-dispersoids displayed a strong orientation relationship with the Al matrix besides they exhibited a high density surrounding the Al matrix grain. Fig. 5.13f presents the interaction of the fine nano-size $\alpha_{MG4\text{-}1}$-Al(Fe,Mo,Mn)Si dispersoids with sub-grain boundaries where effective pinning is observed.

## 5.4 Discussion

This study showed that the MG4-1 (Al-7Si-0.3Mg-0.5Cu-0.5Mn-0.3Mo) alloy with a higher Mn content had a higher creep resistance than the MG3-1 (Al-7Si-0.3Mg-0.5Cu-0.15Mn-0.3Mo) alloy with lower Mn. Both alloys showed softening processes in the from of dynamic recovery and sub-grain formation during creep at 300 °C and 28 MPa, but the MG4-1 alloy showed higher restriction of dynamic recovery leading to lower creep-deformation rates compared to MG3-1. The experimentally determined activation energy for creep was higher in the MG4-1 alloy than in the MG3-1 alloy (249 kJ $mol^{-1}$ versus 203 kJ $mol^{-1}$). The differences in creep behavior and activation

energies are discussed below in terms the recovery processes, creep mechanisms and the influence of the solutes and the second phases.

The creep samples analyzed were not quenched right at failure. To see if significant relaxation and microstructural evolution occurred as the sample cooled down from the test temperature at stress to room temperature, a comparison was made of post-creep quenched MG4-1 and non-quenched MG4-1 creep sample.

*Sub-grain formation*: TEM images in bright field and dark field showing the elemental and grain distribution in the quenched MG4-1 alloy at the end of the creep test are presented in Fig. 5.14a, b. The analyses indicate the formation of sub-structure during creep in the quenched as in the non-quenched MG4-1 alloy (Fig. 5.13, 5.14). EBSD analyses in the quenched MG4-1 alloy (Fig. 5.14c) show a high density of sub-grains in the quenched sample associated with the Si particles, the structure is very similar to the structure of the non-quenched sample (Fig. 5.11a, b). Only difference was seen in the sub-grain size. TEM showed a sub-grain diameter of ~327 nm in the quenched sample as opposed to ~210 nm in the non-quenched sample. In addition, a lower density of sub-grains were seen in the quenched sample. TEM analyzes a small area so the average sub-grain size was also determined by EBSD. The analysis showed that 90% and 95% of the substructure was sub-grain with misorientation < 15° in the quenched and non-quenched MG4-1 alloy, respectively. The average sub-grain diameter was determined to be 3.6 μm in the quenched sample compared to 1.2 μm in the non-quenched sample. These findings indicate that sub-grains formed during creep, but some additional sub-grains formed post creep. The post creep decrease in sub-grain size in the non-quenched sample suggests that small sub-grains formed after creep but sub-grain coarsening was not experienced likely due to the pinning of the boundaries by fine $a_{MG4-1}$ dispersoids as seen in both the quenched and non-quenched MG4-1 (Figs 5.13 and 5.14). The

microstructural features in both the quenched and non-quenched samples reveal the same creep processes in the MG4-1 alloy.

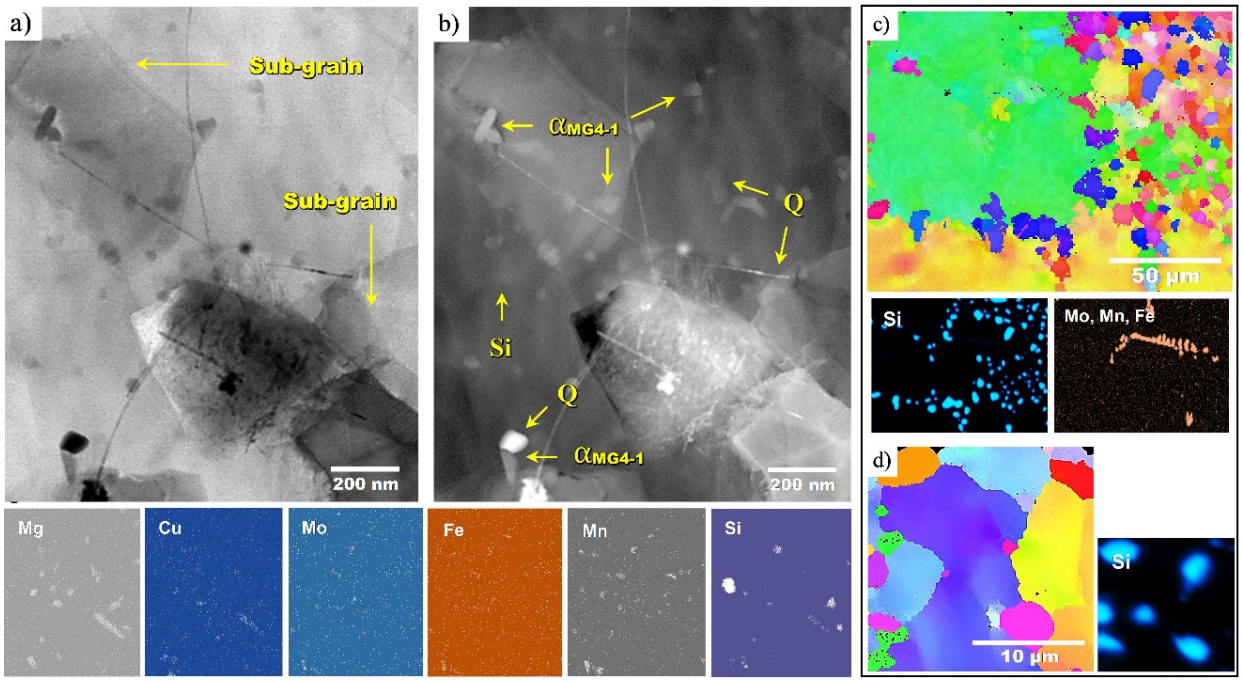


*Figure 5.14. Grain and elemental distribution in the quenched MG4-1 alloy at the end of the creep test: (a) bright field and (b) dark field; Orientation maps with IPF coloring in the Y-direction: (c) low and (d) high magnifications.*

The fact that sub-grains formed during creep agrees with the background information included in the Appendix A of the present paper. It is known that recovery and recrystallization take place during creep leading to the formation of sub-grains and grains [11]. A well-developed sub-grain structure of 0.3-3° misorientation have been observed during steady-state creep [8]. It has been discussed that sub-grain formation may be difficult in solid solution or dispersion strengthened alloys, however, the effects of temperature and dislocation density will facilitate sub-grain formation and in aluminum (with high stacking fault energy) the climb is easy and sub-grain

formation is expected [9]. The recovery in our alloys is very local due to the local strain accumulation at Si particles. This is expected to occur during creep due to the facility of dislocation climb in aluminum alloys.

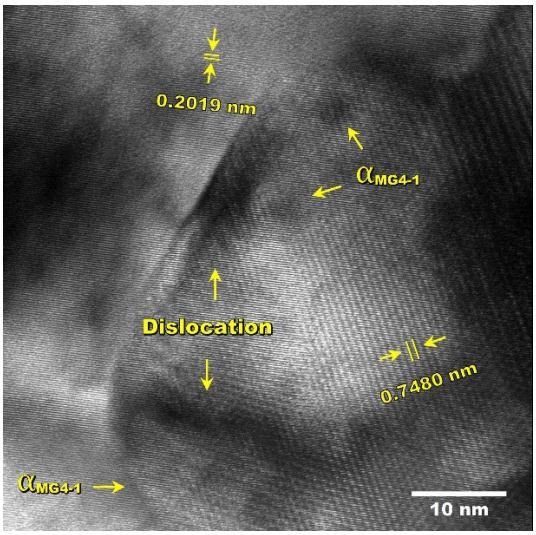


*Figure 5.15. HRTEM image shows the interaction of large and nano-size $\alpha_{MG4-1}$-Al(Fe,Mo,Mn)Si dispersoids with dislocations in the quenched MG4-1 alloy reveling a dislocation passing through a $\alpha_{MG4-1}$-dispersoid (~70 nm) making it incoherent.*

*Formation of Fine dispersoids:* HRTEM image of post-creep quenched MG4-1 sample is shown in Fig. 5.15. Nano-size $\alpha_{MG4-1}$-Al(Fe,Mo,Mn)Si dispersoids (~4–6nm, shown with arrows) are associated with a large ~70 nm $\alpha_{MG4-1}$-Al(Fe,Mo,Mn)Si dispersoid, all showing a similar size and morphology to those seen in the non-quenched MG4-1 alloy (Fig. 5.13) and revealing the same type of interaction with dislocations and sub-grain boundaries seen in the non-quenched MG4-1. A nano-dispersoid outside the large dispersoid is seen to pin the dislocation while another dislocation is seen passing through the large dispersoid making it non-coherent.

The stability of the $\alpha_{MG4-1}$-Al(Fe,Mo,Mn)Si phase observed in TEM and HRTEM analyses also agree with FactSage calculations. This phase does not change its amount in MG4-1when the temperature goes down to room temperature from creep temperature of 200° C. Table 5.3 shows that the amount of α-Al(Fe,Mo,Mn)Si in MG4-1 is 1.7 % at both 200° C and 25° C. In the MG3-1, the amount of the phase decreases slightly from 0.51 to 0.50 % so no α-Al(Fe,Mo,Mn)Si may have precipitated post creep in either alloy. The amount of Si phase also remains constant between the creep temperature and room temperature. According to FactSage, the amount of Q phase increases at room temperature in both alloys but it does not interact with dislocations or sub-grain boundaries.

### 5.4.1 Creep Behavior of MG3-1

Restoration can be considered as a series of processes involving the accumulation of strain, formation of sub-grains and the migration of boundaries. Sub-grains form in aluminum because climb is easy due to high stacking fault energy. While sub-grains can lead to creep strain or even strengthening, the migration of the sub-grain boundaries and their growth can lead to recrystallization or softening. EBSD analysis indicates the presence of sub-grains but no recrystallized grains in MG3-1 (Fig. 5.8). The figure also shows that sub-grains are closely associated with Si particles indicating that Si has a role in the local enhancement of sub-grain formation by accumulating strain. On the other hand, the TEM analysis reveals that sub-grains have been formed with the aid of Si but their growth and recrystallization has experienced a restraint by the $\alpha_{MG3-1}$ dispersoids. The MG3-1 alloy has experienced both the enhancement and restriction of dynamic recovery (DV) during creep. The creep-rate governing process is, hence, the resistance to sub-grain boundary migration.

The mechanism of sub-grain boundary migration is atom diffusion with the activation energy of self-diffusion ($q_{SD}$), solute diffusion ($q_{SD}$) [13], or pipe diffusion (T< 0.6 $T_m$) [14–19]. If boundaries interact with obstacles, there are additional contributions to the activation energy. TEM investigation has shown that shearable coherent $\alpha_{MG3\text{-}1}$-dispersoids have been cut by the dislocations and the boundaries (Fig. 5.10b). The research questions at this time were whether the sub-grain migration and growth were inhibited by self or solute diffusion or by the restraining effects of the shearable $\alpha_{MG3\text{-}1}$ dispersoids and which of these thermally activated processes contribute to the apparent activation energy experimentally determined of 202–203 kJ $mol^{-1}$ for this alloy.

***Dispersoid shearing by subgrain boundaries****:* To see if there has been significant resistance to sub-grain boundary migration by shearable $\alpha_{MG3\text{-}1}$-dispersoids, the stress contribution due to the cutting of the dispersoids by the boundaries was considered. Since sub-grain boundaries are made up of dislocations, the strengthening due to the cutting of shearable particles was calculated using the strengthening, $\tau_C$, due to chemical hardening from the creation of a surface when the dislocation cuts the dispersoid [20]:

$$\tau_C = 2G\left(\frac{\gamma_I}{Gr}\right)^{3/2}\left(\frac{vr}{b}\right)^{1/2} \qquad \text{[eq. 1]}$$

where, $\gamma_I =$ interfacial energy between dispersoid and matrix; $v =$ volume fraction of dispersoids $= 0.11$; $r =$ mean radius of dispersoids $= 68$ nm; $G =$ shear modulus of the matrix $= 26$ GPa; $b =$ Burgers vector $= 0.2857$ nm. The interfacial energy, $\gamma_I$, of coherent precipitates in metallic alloys ranges from 0-200 mJ $m^{-2}$. In aluminum alloys, coherent precipitate interface-energies have been found to range from 0.08 to 0.52 mJ $m^{-2}$ [21]. For α-dispersoids, [22] have reported an interface energy of 150 mJ $m^{-2}$ which was determined via trial and error. Using the density of aluminum of

2710 kg $m^{-3}$ and the atomic weight of 0.027 kg $mol^{-1}$ and taking $\gamma_I$ as 150 mJ $m^{-2}$, the maximum possible contribution from dispersoid shearing by dislocations and to climb would only be 2.0x$10^{-3}$ kJ $mol^{-1}$. This confirms that the contribution of the shearable dispersoids to resistance to recovery is not significant as a creep-rate governing mechanism. Coherent dispersoids in MG3-1 are shearable because of their size; they are cut by dislocations and by migrating grain boundaries offering low amount of resistance to dislocation movement and restoration processes. Dislocations can move to and accumulate at grain boundaries without seeing much resistance inside the grain. Subsequent restoration processes involving grain boundary migration also see limited resistance from shearable dispersoids.

***Solute Diffusion**:* Since the shearable coherent dispersoids in MG3-1 do not cause a significant resistance to sub-grain boundary migration, it was investigated if self, solute, or pipe diffusion governed the creep rate. Self diffusion is more operative at temperature ranges of diffusional creep and pipe diffusion is around ~68% of self-diffusion (~100 kJ $mol^{-1}$ for Al) [23], so solute diffusion is the likely atom diffusion process governing sub-grain migration and hence the creep rate in MG3-1.

*Table 5.5. Diffusion data for the solutes of MG3-1 and MG4-1 [24–35].*

| **Diffusion Coefficient at 300 °C ($m^2s^{-1}$)** | | | | | **Activation Energy for Diffusion (kJ $mol^{-1}$)** | | | | |
|---|---|---|---|---|---|---|---|---|---|
| Al | Si | Cu | Mn | Mg | Al | Si | Cu | Mn | Mg |
| 5.5x$10^{-17}$ | 1.4x$10^{-16}$ | 2.7x$10^{-17}$ | 2x$10^{-22}$ | 1.5x$10^{-16}$ | 120−142 | 136 | 138 | 203–208 | 115−130.5 |

Mn is a slow diffusing species in aluminum, much slower than the diffusion of the other major solutes in the two alloys, namely Cu, Mg, Si and the self-diffusion of Al (Table 5.5). The slow diffusing Mn provides an effective Cottrell atmosphere slowing down dislocation and grain

boundary motion. Mn solute diffusion in aluminum is 203–208 kJ $mol^{-1}$ [24,25] and fits very well the experimentally determined apparent activation energy ($Q_a$) of 202–203 kJ $mol^{-1}$. FactSage calculations show that at the creep test temperatures of 300 – 350 °C, Mn solid solubility in the aluminum matrix of MG3-1 is $4.4x10^{-4}$ wt.%. The calculations also show (Table 5.3) that in MG3-1 there is a small amount of dissolution of the dispersoids as the alloy is raised to the creep temperature with an accompanying increase in the Mn solute content of the aluminum matrix.

The rate governing process in the creep deformation of the alloy is likely the low diffusivity of Mn that slowed down sub-grain migration. To validate this concept, the relationship between the minimum creep rate, $\dot{\varepsilon}_{ss}$ and the sub-grain size, $d_s$, [18] was used (equation A.1) to calculate the effective diffusion coefficient, $D_{eff}$, which is the sum of the diffusion processes (pipe diffusion, self-diffusion or solute diffusion) that take place in sub-grain formation/migration [13,14,19]. Using the creep rate of MG3-1 alloy at 300 °C and 28 MPa, which was experimentally determined as $2x10^{-6}$ $s^{-1}$ and taking the burgers vector of 0.2857 nm, applied stress of 28 MPa, and the shear modulus of 26 GPa, $D_{eff}$ was calculated as $2x10^{-21}$ $m^2$ $s^{-1}$ that approximates well the diffusion coefficient of Mn of $3.9x10^{-22}$ $m^2$ $s^{-1}$ in aluminum [25,32].

It can be concluded that the inhibition of sub-grain formation and boundary migration and consequently recrystallization is due to the Mn solute in the alloy. Mn diffusion has also been found to govern the activation energy for hot deformation of Al alloys in previous studies [26,33]. Shakiba et al. [26] studied the hot compression (400–550 °C) of dilute Al-Fe-Si alloys with 0.1-0.2 wt.% Mn and 0.05-0.31 wt.% Cu. The alloy with 0.2 wt.% Mn exhibited only dynamic recovery and an activation energy of 193 kJ $mol^{-1}$ attributed to the slow diffusion of Mn. Addition of Mn and Cu was found to retard dynamic recovery and decreased the subgrain size and misorientation

compared to the alloy with only 0.1 wt.% Mn. Wang et al. [33] studied Mn/Cr containing Al-Si-Cu alloys in hot compression and determined that the alloy exhibited an activation energy of 208 kJ $mol^{-1}$ and a non-recrystallized structure attributed to the inhibition of recrystallization by the α-Al(Mn,Cr)Si dispersoids.

It is noted that the $R^2$ is lower for MG3-1 than for MG4-1 (Fig. 5.6). There can be changes in the rate governing creep mechanism in the temperature ranges selected for creep testing, but, in this case, the reason is related to the standard deviation on data points, which seem to increase with decreasing temperature (300 °C and 325 °C). The overriding contribution to the creep rate is still the same over the full range of 325 °C – 350 °C due to the rather high $R^2$ of 0.88. The high standard deviations may be due to the varying Mn levels as the $\alpha_{MG3\text{-}1}$ dispersoids dissolve at the creep temperatures of 325 °C and 350 °C releasing varying amounts Mn solute for creating dislocation atmospheres at existing and newly formed dislocations.

### 5.4.2 Creep Behavior of MG4-1

TEM analysis indicated that sub-grain formation and sub-grain pinning by $\alpha_{MG4\text{-}1}$-Al(Fe,Mo,Mn)Si dispersoids (Fig. 5.13f) have occurred in MG4-1 alloy and that the rate governing process for the creep deformation of MG4-1 at 300 °C and 28 MPa is also sub-grain boundary migration, although with a higher experimentally activation energy (249 kJ $mol^{-1}$) than the apparent creep activation energy of MG3-1 (203 kJ $mol^{-1}$). The possible contributions of atom diffusion and dispersoids were calculated to estimate the apparent activation energy experimentally obtained for MG4-1.

***Sub-grain boundary pinning by $\alpha_{MG4\text{-}1}$-Al(Fe,Mo,Mn)Si dispersoids*:** Submicron coherent dispersoids in the 6 nm size range observed in the MG4-1 alloy (Fig. 5.13) are too small to be

sheared by dislocations. They would act as non-coherent precipitates providing Zener pinning, $P_z$, of subgrain boundaries (Fig. 5.13e). $P_z$ was calculated using eq. A.4 and taking $\gamma =$ surface energy of the subgrain boundary $= 75$ mJ m$^{-2}$ for aluminum [43]; $v = 0.158$; $r = 3$ nm; $d_s = 1.2$ μm. Using the density of aluminum of 2710 kg m$^{-3}$ and the atomic weight of 0.027 kg mol$^{-1}$, the maximum possible contribution from Zener pinning of sub-grain boundaries would be 15 kJ mol$^{-1}$. Post-creep quenched samples gave slightly larger subgrain diameter. TEM analysis showed twice the size, so the contribution from sub-grain boundary pinning can be higher depending on the vol fraction of the dispersoids.

***Solute Diffusion*:** The effective diffusion coefficient, $D_{eff}$, for sub-grain boundary migration of MG4-1 at 300 °C and 28 MPa was calculated using eq. A.1 with the minimum creep rate experimentally determined as $\dot{\varepsilon_{ss}} = 5.8\text{x}10^{-7}$ s$^{-1}$ and average sub-grain size, $d_s$, of 1.2 μm. $D_{eff}$ was calculated to be $6.5\text{x}10^{-19}$ m$^2$ s$^{-1}$ which unlike the MG3-1 alloy does not fit the diffusion coefficient of Mn in Al that is ~$10^{-22}$ – $10^{-21}$ m$^2$ s$^{-1}$. The effective diffusion coefficient indicates that diffusion rates were faster than Mn diffusion, contributing to the creep rate in MG4-1 alloy. Faster diffusion rates in MG4-1 can be associated with Al self-diffusion, Cu-solute diffusion, Si-solute diffusion in aluminum, or pipe diffusion [28,34–36].

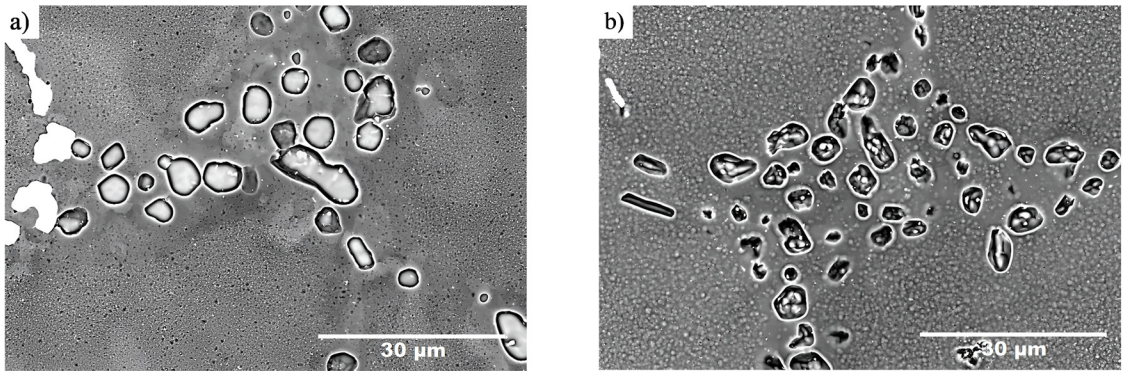


*Figure 5.16. ECC image showing spheroidized Si in creep tested at 300 °C and 28 MPa samples of (a) MG3-1 and (b) MG4-1.*

In sub-grain formation of the alloys of this study, Si particles play a significant role in strain accumulation leading to the generation of sub-grains. Sub-grains are found in close association with Si particles in the alloy (Fig. 5.11) which have a key role in strain accumulation and enhancing recovery. As seen in Fig. 5.16, spheroidized Si particles in MG4-1 are finer than those in MG3-1. This is attributed to the lack of additional Si solute available for coarsening as described above. The coarsening of Si in the temperature ranges of 200–300 °C is only due to Si surface diffusion. It is, hence, suggested that Si diffusion has a rate-governing contribution to creep in MG4-1.

Investigating other possible contributions to the rate sub-grain migration in MG4-1, we can note that due to the thermal stability of the dispersoids at 200–300 °C, there is no additional Mn solute to continue to exert drag force on dislocations that are generated during creep. The other solutes, Cu and Mg, do not have discerned roles in the sub-grain formation of MG4-1 and Al self diffusion with higher activation energy, so they must compete for vacancies with the other solutes Si, Cu and Mg that have lower activation energies. Since in a network, dislocation links may provide the short circuit path for the vacancies from one point to any other, it is likely that pipe diffusion becomes dominant over lattice diffusion especially at moderate temperatures. Al in MG4-1, in view of competition of other solutes for vacancies, would resort to pipe diffusion for boundary migration [37] at 300 °C (~0.4 $T_m$) that is 100 kJ $mol^{-1}$ for aluminum [23].

***The activation energy for the creep deformation:*** The activation energy for the creep deformation of MG4-1 can be calculated as the combined activation energies of Si solute diffusion ($q_{si}$), sub-grain boundary migration through pipe diffusion, $q_{p,}$ and the Zener pinning, $P_z$, of sub-grain boundaries by coherent non-shearable $\alpha_{MG4\text{-}1}$-Al(Fe,Mo,Mn)Si dispersoids. The total activation energy ($Q_a$) for the MG4-1 alloy during creep is then $Q_a = q_{Si} + q_P + q_{PZ} = (136 + 100 + 15)$

kJ $mol^{-1}$ = 251 kJ $mol^{-1}$, which agrees very well with the experimentally determined activation energy of 249 kJ $mol^{-1}$.

The activation energy for creep, wherein sub-grain boundary migration is the rate-governing process, has been found to depend on diffusion of solutes in various aluminum alloys. Measurements of recovery in Al–Mg alloys found that the activation energy depended on the magnesium content of the alloy and ranged from 277 kJ $mol^{-1}$ for Al–1% Mg to 231 kJ $mol^{-1}$ for Al–5% Mg [28]. In all cases, it was found to be much larger than that for self-diffusion for aluminium of 142 kJ $mol^{-1}$.

**Overview of the Effect of Mn on the Creep Behavior of Al-6Si-0.5Cu-0.3Mg-0.35Mo Alloy**

Both alloys of this study have similar Al-Si-Mg-Cu-(Mo) compositions with the main difference being the Mn content. MG4-1 has higher Mn (0.5 wt.% Mn) than MG3-1 (0.17 wt.% Mn). The study revealed that Mn alters various features in the Al-Si-Mg-Cu-(Mo) alloy as summarized in Table 5.6.

The increased level of Mn in MG4-1 led to an increased amount of α-Al(Fe,Mo,Mn)Si dispersoids in the alloy (1.7% versus 0.5%). There were also differences in size distribution and coherency of the dispersoids in the two alloys. MG3-1 alloy with the lower Mn level has shearable coherent α-Al(Fe,Mo,Mn)Si dispersoids with average size up to ~214 nm that were cut by dislocations and migrating sub-grain boundaries offering low amount of resistance to dislocation movement and sub-grain boundary migration. Some of the α-Al(Fe,Mo,Mn)Si dispersoids in MG4-1 were semi-coherent with an average size of 149 nm but there were also 6 nm fully coherent non-shearable α-Al(Fe,Mo,Mn)Si dispersoids that pined the sub-grain boundaries and restricting sub-grain boundary migration (Fig. 5.13f) providing the key role in creep resistance.

*Table 5.6. Effects of Mn on the Al-6Si-0.5Cu-0.3Mg-0.35Mo alloy (in wt.%).*

| | **MG3-1 (0.17 wt.% Mn)** | **MG4-1 (0.50 wt.% Mn)** |
|---|---|---|
| ***Effect of Mn on α-Al(Fe,Mo,Mn)Si dispersoids*** | | |
| Composition (wt.%) | 17Fe-5Mo-19Mn-6Si-53Al | 18Fe-5Mo-23Mn-7Si-47Al |
| Amount (wt.%) at 200 ˚C and 300 ˚C | 0.52 and 0.51 | 1.7 and 1.7 |
| Size/inter-particle spacing | 50-215 nm / 263 nm | 6-290 nm (~149 nm) / 213 nm |
| Volume % (at 300 ˚C) | 11 vol.% | 16 vol.% |
| Thermal Stability<br>*Precipitation temperature*<br>*Dissolution between 200 ˚C & 300 ˚C* | <br>576 ˚C<br>2% dissolution | <br>590 ˚C<br>No dissolution |
| Coherency (at 300 ˚C) | Semi coherent; coherent face with 4.2% mismatch strain | 28 - 290 nm incoherent or semi-coherent; 6 nm coherent |
| Role in creep resistance | minor | Zener pinning of subgrain boundaries by 6 nm coherent |
| ***Effect of Mn on the Eutectic Si Phase*** | | |
| Size (as cast) | ~0.47 μm | ~0.62 μm |
| Coarsening (T7) | ~9.2 μm | ~5.9 μm |
| ***Effect of Mn on As-Cast Grain Size*** | | |
| | 270 μm | 102 μm |
| ***Effect of Mn on the Ageing precipitates*** | | |
| Size (as cast) | Q:12.6 μm; θ: 10.1 μm | Q: 4.9 μm; θ: 6.7 μm |
| ***Subgrains (creep tested at 300 ˚C & 28 MPa)*** | | |
| Size | 15 μm | 1.2 μm |
| Sub-grain boundaries | Cut coherent shearable dispersoids | Pinned by coherent non-shearable dispersoids |
| ***Activation energy (kJ mol$^{-1}$)*** | | |
| Experimentally determined | 203 kJ mol$^{-1}$ | 249 kJ mol$^{-1}$ |
| Calculated | $Q_a = q_{Mn}$ = 203-208 kJ mol$^{-1}$ | $Q_a = q_{Si} + q_P + q_{PZ}$ = 251 kJ mol$^{-1}$ |

The differences in the size and coherency of the α-Al(Fe,Mo,Mn)Si are attributed to the difference in the thermal stability of the dispersoids. Yuan et al [38] studied the evolution of α-Al(Mn,Fe)Si dispersoids during homogenization at 600 °C and reported that the process can be divided into four stages: nucleation, growth, dissolution, and coarsening with differing coarsening kinetics. At the solutionizing temperature of 540 °C (Table 5.3), the dispersoids in both alloys would precipitate from the supersaturated matrix as coherent dispersoids and grow. The small coherent

dispersoids are closely associated with the larger precipitates, but it is unlikely that they are nucleated by the larger dispersoids since the coherent dispersoids would readily form in the α-Al matrix. This is followed by dissolution of some of the dispersoids to achieve equilibrium, accompanied by coarsening through the dissolution of small particles and the growth of larger ones that also lose coherency as they grow.

The MG4-1 has thermally stable intermetallics of higher Fe, Mn, and Si content that would exhibit lower coarsening rates. The MG4-1, therefore, retains its smaller coherent dispersoids of 6 nm range. Some of the 10–15 nm dispersoids that are non-coherent are also seen in MG4-1, but the incoherency is notably because of interaction with dislocations (Fig. 5.13c, Fig. 5.15) during creep. The MG3-1, on the other hand, loses its fine dispersoids during solutionizing due to the higher coarsening rate of its dispersoids, exhibiting a larger average dispersoid size than the MG4-1; its dispersoids are also semi coherent or incoherent due to growth and coarsening due to the interactions with dislocations and sub-grain boundaries (Fig. 5.10b, c) [39].

## 5.5 Conclusions

The influence of Mn on the microstructure and creep properties has been investigated in an Al-7Si-0.3Mg-0.5Cu-0.3Mo alloy. The following conclusions can be drawn:

1. Thermodynamic calculations show the influence of Mn on the solidification temperature and the amount phase in each alloy. SEM observations confirmed this behavior from microstructural analysis, indicating a higher concentration of $\alpha_{MG4\text{-}1}$-Al(Fe,Mo,Mn)Si phase with Mn addition. The $\alpha_{MG3\text{-}1}$-Al(Fe,Mo,Mn)Si dispersoids in MG3-1 were coherent and shearable with average size ~135 nm. The $\alpha_{MG4\text{-}1}$-Al(Fe,Mo,Mn)Si dispersoids in the MG4-

1 were semi-coherent with average size of 149 nm, but the alloy also had fully coherent 6 nm dispersoids.

2. TEM investigation showed that the $\alpha_{MG4-1}$-Al(Fe,Mo,Mn)Si dispersoids in MG4-1 alloy, with the higher Mn content, had higher concentrations of Fe, Mn and Si and hence higher thermal stability compared to the $\alpha_{MG3-1}$-Al(Fe,Mo,Mn)Si in MG3-1 alloy.

3. Creep resistance was higher in the Al-7Si-0.3Mg-0.5Cu-0.3Mo-0.5Mn (MG4-1) alloy than in the Al-7Si-0.3Mg-0.5Cu-0.15Mn-0.3Mo (MG3-1) alloy at 300 °C, 325 °C and 350 °C. Both alloys showed grain boundary formation, and in both alloys, solute diffusion and the dispersoids had roles in the creep rate and creep activation energies.

4. Eutectic Si spheroidized during solutionizing treatment at 540 °C in both alloys. Further coarsening of the spheroidized Si occurred in MG3-1 due to the availability of additional Si solute from the dissolution of $\alpha_{MG3-1}$-Al(Fe,Mo,Mn)Si dispersoids at the creep test temperature of 300 °C. In the MG4-1 alloy, the thermally stable $\alpha_{MG4-1}$-Al(Fe,Mo,Mn)Si did not dissolve during creep testing, limiting the further coarsening of the spheroidized Si. The coarser spheroidized Si in MG3-1 initiated sub-grain formation by locally accumulating strain while the finer Si particles in MG4-1 were less effective in initiating sub-grain formation.

5. The slow diffusion of Mn restrained dislocation motion and subgrain formation in the MG3-1 alloy, and governed its creep activation energy experimentally determined at 300−350 °C and 28 MPa as 203 kJ $mol^{-1}$. The $\alpha_{Mg3-1}$ dispersoids were not very effective in inhibiting grain boundary migration; the main resistance was provided by Mn solute. The effective

diffusion coefficient subgrain boundary migration at 300 °C was calculated to be $2x10^{-21}$ $m^2$ $s^{-1}$ that was aligned with the diffusion coefficient of Mn in aluminum at 300 °C.

6. The calculated activation energy for creep for the MG4-1 alloy, based on TEM analysis of creep tested samples and thermodynamic simulations, was of 251 kJ $mol^{-1}$. It had contributions from activation energy of Si diffusion (136 kJ $mol^{-1}$) governed by Si particle coarsening, activation energy for subgrain boundary migration governed by pipe diffusion in aluminum (100 kJ $mol^{-1}$) and activation energy for subgrain boundary pinning by coherent non-shearable $\alpha_{MG4\text{-}1}$-Al(Fe,Mo,Mn)Si dispersoids (15 kJ $mol^{-1}$). The combined activation energy of 251 kJ $mol^{-1}$ agreed well with experimentally determined apparent activation energy of 249 kJ $mol^{-1}$.

7. In MG4-1 alloy, Mn addition at 0.5 wt.% level was effective in improving the creep resistance of the Al-7Si-0.3Mg-0.5Cu-0.3Mo alloy by limiting sub-grain formation or sub-grain boundary migration in two ways. (i) Mn combined with Si to form thermally stable dispersoids at 300 °C; this limited the Si available for coarsening the Si particles and lowered their effectiveness in initiating sub-grain formation during creep, (ii) Mn formed fine coherent non-sherable $\alpha_{MG4\text{-}1}$-dispersoids that impede sub-grain migration.

# APPENDIX A. Sub-grain Formation and Sub-grain Boundary Migration during Creep and the Activation Energies

Recovery and recrystallization take place during creep, leading to the formation of sub-grains and grains. Even though these contribute to creep strain, they can also lead to creep strengthening. The focus in this section is on sub-grain formation and sub-grain boundary migration during creep.

Recovery substructures that form during creep have been studied well in single phase materials [11]. A well-developed sub-grain structure of 0.3-3° misorientation was observed during steady-state creep (Stage II) [12]. It has been discussed [13] that sub-grain formation may be difficult in solid solution or dispersion strengthened alloys, however, the effects of temperature and dislocation density facilitate sub-grain formation, so, in Al, with high stacking fault energy, the climb is easy and sub-grain formation is expected. Sub-grains have been well observed in cold and warm worked aluminum alloys [40], single crystal Al, and annealed polycrystalline Al [41].

Migrating sub-grain boundaries lead the growth of the sub-grain and to the formation of recrystallization nuclei [42]. The mechanism of sub-grain migration has been claimed to be due to atom diffusion with activation energies of self-or solute-diffusion [12] or pipe diffusion, especially below 0.6 $T_m$ [14–19]. The reason for different activation energies is due to the fact that dislocation recovery is a series of events going from cell formation [37] to dislocation annihilation inside the cells, sub-grain formation, and sub-grain growth. During this process, the sub-grain size changes and the misorientation transforms from 1° towards 15°.

In polycrystalline metals, sub-grain size has been related to creep strengthening because the dislocations are found inside the grain, so the boundaries are taken as hard zones. The minimum creep rate, $\dot{\varepsilon}_c$, is reported to depend on the cube of the sub-grain size, $d_s$, [19] given as

$$5.6\ \dot{\varepsilon}_{ss} = S\left(\frac{D_{eff}}{b^2}\right)\left(\frac{d_s}{b}\right)^P\left(\frac{\sigma}{E}\right)^N \qquad \text{[eq. A.1]}$$

where, $S = 1.5\text{x}10^9$ for alloys of high stacking fault energy, $D_{eff}$ = effective diffusion coefficient; $b$ = magnitude of the Burgers vector; $\sigma$ = applied stress; $E$ = modulus of elasticity; $P = 3$ and $N = 8$. $D_{eff}$ is the total diffusion processes (pipe diffusion, self-diffusion or solute diffusion) that

takes place in sub-grain formation/migration. While self diffusion is observed at the whole temperature range [37], pipe diffusion and solute diffusion can occur below ~0.6 $T_m$ [13].

*In dispersoids strengthened alloys,* dispersoids exert a force or pressure (Zener drag) on sub-grain boundaries and may influence recovery processes. The nature of the particle/boundary interface, and the shape, size, spacing and volume fraction, $F_v$, of the particles can modify Zener drag [43–47].

*Zener drag of incoherent particles:* The Zener pinning pressure, $P_z$, exerted by incoherent spherical particles is given as $P_z = 3v\gamma/(2r)$ [eq. A.2], where $v =$ volume fraction of randomly distributed spherical incoherent particles of radius, $r$, and $\gamma =$ boundary specific energy.

*Zener drag from coherent particles:* During the passage of grain boundary across a coherent particle, the coherent interface transforms to incoherent because it requires energy from the moving boundary. Here, the energy of the incoherent interface is greater than that of the original coherent interface. Therefore, coherent particles will be more effective in pinning boundaries than incoherent particles. Nes et al. [48] have shown that the maximum drag force from a coherent particle is twice the maximum drag force from incoherent particle, so the Zener drag is given as $P_z = 3v\gamma/(r)$ [eq. A.3].

*Zener drag from particles on a sub-grain boundary:* Considering that the Zener drag is proportional to grain boundary energy, $\gamma$, it is expected that the Zener drag on sub-grain boundaries of low energy be lower than the Zener drag on high energy grain boundaries. In Cu, it has been shown that the Zener drag on sub-grains is only 10% lower than the drag force on grain boundaries [49]. Zener drag has been analyzed by [46]; the Zener drag, $P_{z,}$ was given as $P_z = (3\gamma v d_s)/(\pi r^2)$ [eq. A.4], where $d_s =$ average sub-grain diameter.

# APPENDIX B

Appendix B contains creep data in the form of plots of creep rate versus time that show the minimum creep rates (Fig. B1), and variation in data for activation energies (Tables B1 and B2, and Figs. B2 and B3).

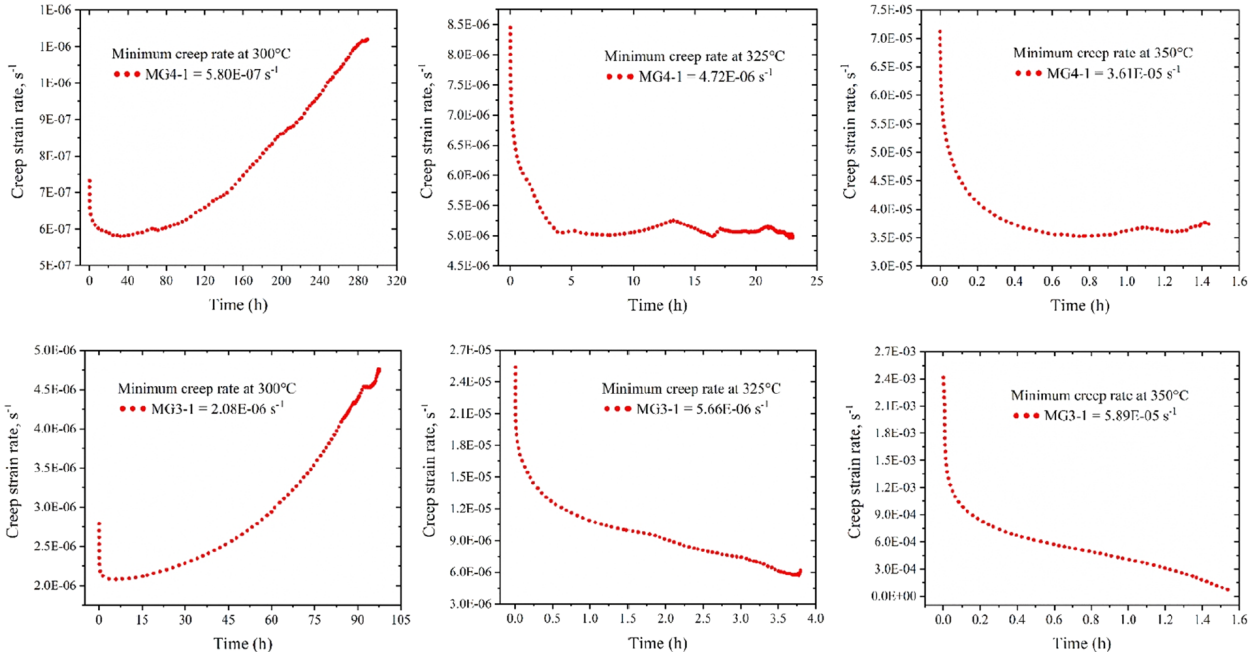


*Figure B1. Creep rate vs time under creep stress of 28 MPa at 300 °C, 325 °C and 350 °C for MG3-1 and MG4-1 alloys.*

*Table B1. Variation in the activation energy from three different creep tests for MG3-1 alloy.*

| **1000/T (K)** | **Test 1 In $\dot{\varepsilon}$** | **Test 2 In $\dot{\varepsilon}$** | **Test 3 In $\dot{\varepsilon}$** | **Stand. Error from In $\dot{\varepsilon}$** | **Activation Energy (kJ/mol)** |
|---|---|---|---|---|---|
| 1.74474 | -13.11928 | -13.20711 | -13.31016 | 0.095541078 | 203.676372 |
| 1.67182 | -9.99658 | -10.103549 | -10.28354 | 0.14502021 | 199.886812 |
| 1.60475 | -9.72754 | -9.89154 | -9.82754 | 0.082655913 | 208.839366 |
| | | | | | Avg. = **203.90085** |

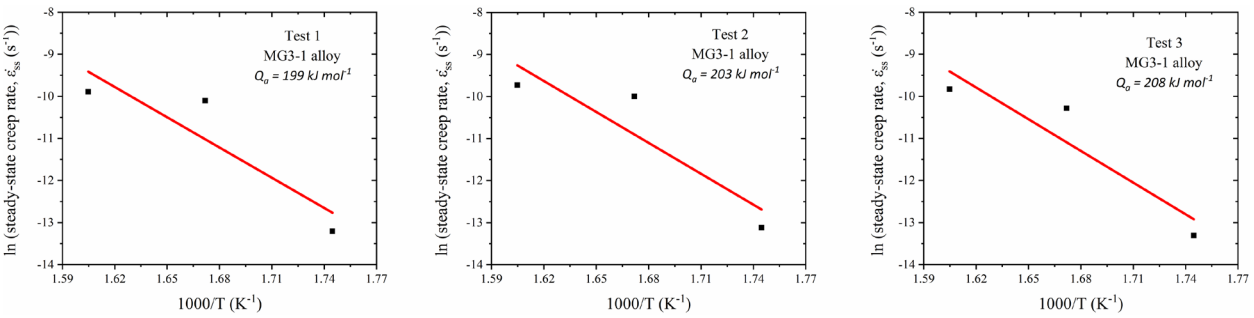


*Figure B2. Arrhenius plot of log of steady-state creep rate vs the reciprocal of temperature at 28 MPa indicating the variation in the activation energy at three different creep tests for MG3-1 alloy.*

*Table B2. Variation in the activation energy from three different tests for MG4-1 alloy.*

| 1000/T (K) | Test 1 In $\dot{\varepsilon}$ | Test 2 In $\dot{\varepsilon}$ | Test 3 In $\dot{\varepsilon}$ | Stand. Error from In $\dot{\varepsilon}$ | Activation Energy (kJ/mol) |
|---|---|---|---|---|---|
| 1.74474 | -14.29979 | -14.15339 | -14.199051 | 0.0432475 | 248.929474 |
| 1.67182 | -12.00253 | -11.79172 | -11.86154 | 0.062000837 | 240.783378 |
| 1.60475 | -10.1116 | -10.11813 | -10.12643 | 0.004291204 | 242.228390 |
| | | | | | Avg. = **243.7470807** |

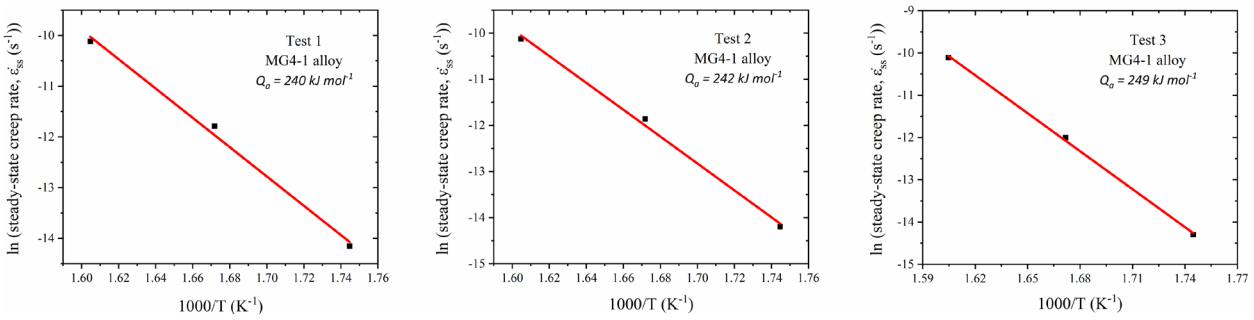


*Figure B3. Arrhenius plot of log of steady-state creep rate vs the reciprocal of temperature at 28 MPa indicating the variation in the activation energy at three different creep tests for MG3-1 alloy.*

## 5.6 Acknowledgment

This research was supported by the Natural Sciences and Engineering Research Council of Canada (NSERC). The authors thank to Konstantinos Korgiopoulos for his assistance in experimental work. Raul Irving Arriaga Benitez would like to gratefully acknowledge the financial support of Gerald Hatch Fellowship (Grant No. 256938), Fonds Québécois de la Recherche sur la Nature et les Technologies – Programme de Bourses d'Excellence pour Étudiants Étrangers (FRQNT – PBEEE) (Grant No. 451069) and Consejo Nacional de Humanidades, Ciencias y Tecnologias– Secretaria de Energia (CONAHCyT–SENER) (Grant No. 451069).

## 5.7 References

[1] M. Pekguleryuz, E. Ozbakir, A.R. Farkoosh, Diesel engine: applications of aluminum alloys, in: G.E. Totten, M. Tiryakioglu, O. Kessler (Eds.), Encyclopedia of Aluminum and Its Alloys, CRC Press, Boca Raton, 2018: pp. 743–762.

[2] A.R. Farkoosh, X. Grant Chen, M. Pekguleryuz, Dispersoid strengthening of a high temperature Al-Si-Cu-Mg alloy via Mo addition, Mater. Sci. Eng. A. 620 (2015) 181–189. https://doi.org/10.1016/j.msea.2014.10.004.

[3] R.I. Arriaga-Benitez, M. Pekguleryuz, Recent progress in creep-resistant aluminum alloys for diesel engine applications: a review, Materials 17 (2024) 3076. https://doi.org/10.3390/ma17133076.

[4] H.Y. Kim, T.Y. Park, S.W. Han, H.M. Lee, Effects of Mn on the crystal structure of α-Al(Mn,Fe)Si particles in A356 alloys, J. Cryst. Growth 291 (2006) 207–211. https://doi.org/10.1016/j.jcrysgro.2006.02.006.

[5] A.R. Farkoosh, X. Grant Chen, M. Pekguleryuz, Interaction between molybdenum and manganese to form effective dispersoids in an Al-Si-Cu-Mg alloy and their influence on creep resistance, Mater. Sci. Eng. A. 627 (2015) 127–138. https://doi.org/10.1016/j.msea.2014.12.115.

[6] R.I. Arriaga-Benitez, M. Pekguleryuz, The synergistic effects of nano-sized α-Al(Mn,Cr,Fe)Si and Al–Si–Zr dispersoids on the creep behavior Al–Si–Mg–Cu (Mn, Cr, Zr) diesel engine alloy, Mater. Sci. Eng. A. 872 (2023) 144949. https://doi.org/10.1016/j.msea.2023.144949.

[7] X. Zhang, D. Wang, X. Li, H. Zhang, H. Nagaumi, Understanding crystal structure and morphology evolution of Fe, Mn, Cr-containing phases in Al-Si cast alloy, Intermetallics

131 (2021) 107103. https://doi.org/10.1016/j.intermet.2021.107103.

[8] A.N. Gots, V.S. Klevtsov, Method for calculating the heat-stressed state of the cylinder head of a liquid-cooled diesel engine, CHT (MHT) (2020) 26–32. https://doi.org/10.17513/snt.38027.

[9] E. Ogris, A. Wahlen, H. Lüchinger, P.J. Uggowitzer, On the silicon spheroidization in Al–Si alloys, J. Light Met. 2 (2002) 263–269. https://doi.org/10.1016/S1471-5317(03)00010-5.

[10] M. Ibrahim, M. Abdelaziz, A. Samuel, H. Doty, F. Samuel, Spheroidization and coarsening of eutectic Si particles in Al-Si-based alloys, Adv. Mater. Sci. Eng. 2021 (2021) 1–16. https://doi.org/10.1155/2021/6678280.

[11] S.V. Raj, I.S. Iskovitz, A.D. Freed, Modeling the role of dislocation substructure during class M and exponential creep, in: A.S. Krausz, K. Krausz (Eds.), Unified Constitutive Laws of Plastic Deformation, Academic Press, Ontario, 1996: pp. 343–439.

[12] M.M. Myshlyaev, O.N. Senkov, V.A. Likhachev, Strength of Metals and Alloys (ICSMA 7), third ed., Elsevier, Montreal, 1986.

[13] O.D. Sherby, P.M. Burke, Mechanical behavior of crystalline solids at elevated temperature, Prog. Mater. Sci. 13 (1968) 323–390. https://doi.org/10.1016/0079-6425(68)90024-8.

[14] F.J. Humphreys, M. Hatherly, Recrystallization of single-phase alloys, in: F.J. Humphreys, M. Hatherly (Eds.), Recrystallization and Related Annealing Phenomena, Elsevier, Oxford, 1995: p. 183.

[15] O.D. Sherby, J. Weertman, Diffusion-controlled dislocation creep: a defense, Acta Metall. 27 (1979) 387–400. https://doi.org/10.1016/0001-6160(79)90031-2.

[16] H. Luthy, A.K. Miller, O.D. Sherby, The stress and temperature dependence of steady-state flow at intermediate temperatures for pure polycrystalline aluminum, Acta Metall. 28 (1980) 169–178. https://doi.org/10.1016/0001-6160(80)90066-8.

[17] M.E. Kassner, Five-power-law creep, in: M.E. Kassner (Ed.), Fundamentals of Creep in Metals and Alloys, Elsevier, Massachusetts, 2015: p. 16.

[18] H.E. Evans, G. Knowles, A model of creep in pure materials, Acta Metall. 25 (1977) 963–975. https://doi.org/10.1016/0001-6160(77)90185-7.

[19] O.D. Sherby, R.H. Klundt, A.K. Miller, Flow stress, subgrain size, and subgrain stability at elevated temperature, Metall. Trans. A. 8 (1977) 843–850. https://doi.org/10.1007/BF02661565.

[20] T. Gladman, Precipitation hardening in metals, Mater. Sci. Technol. 15 (1999) 30–36. https://doi.org/10.1179/026708399773002782.

[21] F.J. Humphreys, M. Hatherly, The mobility and migration of boundaries, in: F.J. Humphreys, M. Hatherly (Eds.), Recrystallization and Related Annealing Phenomena, Elsevier, Oxford, 2004: pp. 121–167.

[22] C.L. Liu, Q. Du, N.C. Parson, W.J. Poole, The interaction between Mn and Fe on the precipitation of Mn/Fe dispersoids in Al-Mg-Si-Mn-Fe alloys, Scr. Mater. 152 (2018) 59–63. https://doi.org/10.1016/j.scriptamat.2018.04.012.

[23] R.C. Picu, D. Zhang, Atomistic study of pipe diffusion in Al–Mg alloys, Acta Mater. 52

(2004) 161–171. https://doi.org/10.1016/j.actamat.2003.09.002.

[24] H. Mehrer, N. Stolica, N. A. Stolwijk, Diffusion in Solid Metals and Alloys, Springer, Berlin, 1990.

[25] S.-I. Fujikawa, Y. Nishida, Analysis of interdiffusion experiments in Al/Mn artificial multilayered films and impurity diffusion of manganese in aluminum, DDF 95–98 (1993) 617–622. https://doi.org/10.4028/www.scientific.net/DDF.95-98.617.

[26] M. Shakiba, N. Parson, X.-G. Chen, Hot deformation behavior and rate-controlling mechanism in dilute Al–Fe–Si alloys with minor additions of Mn and Cu, Mater. Sci. Eng. A. 636 (2015) 572–581. https://doi.org/10.1016/j.msea.2015.04.029.

[27] K.E. Knipling, D.C. Dunand, D.N. Seidman, Criteria for developing castable, creep-resistant aluminum-based alloys - A review, IJMR. 97 (2006) 246–265. https://doi.org/10.1515/ijmr-2006-0042.

[28] C. Barioz, Y. Brechet, J.M. Legresy, M.C. Cheynet, Recovery of aluminum-magnesium alloys, in: L. Arnberg, O. Lohne, E. Nes, N. Ryum (Eds.), The 3rd International Conference on ALUMINIUM ALLOYS, Norwegean Institute of Technology, Trondheim, 1992: pp. 347–354.

[29] T.E. Volin, R.W. Balluffi, Annealing kinetics of voids and the self-diffusion coefficient in aluminum, Phys. Status Solidi B. 25 (1968) 163–173. https://doi.org/10.1002/pssb.19680250116.

[30] S. Fujikawa, K. Hirano, Diffusion of gold and copper in aluminum, Trans. Jpn. Inst. Met. 12 (1971) 434–441. https://doi.org/10.2320/matertrans1960.12.434.

[31] S.J. Rothman, N.L. Peterson, L.J. Nowicki, L.C. Robinson, Tracer diffusion of magnesium in aluminum single crystals, in: De Gruyter (Ed.), Physica Status Solidi / B, Berlin, 1974: pp. 461–466.

[32] S. Fujikawa, K.-I. Hirano, Impurity diffusion of manganese in aluminum, MSF 13–14 (1987) 539–546. https://doi.org/10.4028/www.scientific.net/MSF.13-14.539.

[33] J. Wang, P.D. Lee, R.W. Hamilton, M. Li, J. Allison, The kinetics of Fe-rich intermetallic formation in aluminium alloys: In situ observation, Scr. Mater. 60 (2009) 516–519. https://doi.org/10.1016/j.scriptamat.2008.11.048.

[34] M. Bishop, K.E. Fletcher, Diffusion in aluminium, Int. Met. Rev. 17 (1972) 203–225. https://doi.org/10.1179/imtlr.1972.17.1.203.

[35] S. Fujikawa, K. Hirano, Y. Fukushima, Diffusion of silicon in aluminum, Metall. Trans. A. 9 (1978) 1811–1815. https://doi.org/10.1007/BF02663412.

[36] F.J. Humphreys, M. Hatherly, The Structure and energy of grain boundaries, in: F.J. Humphreys, M. Hatherly (Eds.), Recrystallization and Related Annealing Phenomena, Elsevier, Oxford, 2004: p. 104.

[37] F.J. Humphreys, M. Hatherly, Recovery after deformation, in: F.J. Humphreys, M. Hatherly (Eds.), Recrystallization and Related Annealing Phenomena, Elsevier, Oxford, 1995: pp. 127–171.

[38] Z. Yuan, Y. Tu, T. Yuan, Y. Huang, Y. Zhang, Effect of the interaction between Fe and Si

on the precipitation behavior of dispersoids in Al–Mn alloys during homogenization, Vacuum 184 (2021) 109915. https://doi.org/10.1016/j.vacuum.2020.109915.

[39] F.J. Humphreys, M. Hatherly, The structure and energy of grain boundaries, in: F.J. Humphreys, M. Hatherly (Eds.), Recrystallization and Related Annealing Phenomena, Elsevier, Oxford, 2004: p. 112.

[40] P.B. Prangnell, Jacob R. Bowen, A. Gholinia, The formation of submicron and nanocrystalline grain structures by severe deformation, in: A.R. Dinesen, M. Eldrup, D. Juul Jensen, S. Linderoth, T.B. Pedersen, N.H. Pryds, A. Schrøder Pedersen, J.A. Wert (Eds.), Science of Metastable and Nanocrystalline Alloys. Structure, Properties and Modelling. Proceedings, Risø National Laboratory, Roskilde, 2001: pp. 105–126.

[41] M.M. Myshlaev, S.S. Olevskii, S.K. Maksimov, V.A. Likhachev, G.V. Vladimirova, Effect of interstitial loop formation on creep resistance of aluminium, Phys. Stat. Sol. (a) 7 (1971) 325–333. https://doi.org/10.1002/pssa.2210070203.

[42] S.F. Exell, D.H. Warrington, Sub-grain boundary migration in aluminium, Phil. Mag. 26 (1972) 1121–1136. https://doi.org/10.1080/14786437208227368.

[43] F.J. Humphreys, M. Hatherly, The structure and energy of grain boundaries, in: F.J. Humphreys, M. Hatherly (Eds.), Recrystallization and Related Annealing Phenomena, Elsevier, Oxford, 2004: pp. 91–119.

[44] M.E. Kassner, Creep behavior of particle-strengthened alloys, in: M.E. Kassner (Ed.), Fundamentals of Creep in Metals and Alloys, Elsevier, Massachusetts, 2015: pp. 161–180.

[45] C.J. Tweed, B. Ralph, N. Hansen, The pinning by particles of low and high angle grain boundaries during grain growth, Acta Metall. 32 (1984) 1407–1414. https://doi.org/10.1016/0001-6160(84)90086-5.

[46] S.S. Hansen, J.B.V. Sande, M. Cohen, Niobium carbonitride precipitation and austenite recrystallization in hot-rolled microalloyed steels, Metall. Trans. A. 11 (1980) 387–402. https://doi.org/10.1007/BF02654563.

[47] M. Gómez, S.F. Medina, P. Valles, Determination of driving and pinning forces for static recrystallization during hot rolling of a niobium microalloyed steel, ISIJ Int. 45 (2005) 1711–1720. https://doi.org/10.2355/isijinternational.45.1711.

[48] E. Nes, N. Ryum, O. Hunderi, On the zener drag, Acta Metall. 33 (1985) 11–22. https://doi.org/10.1016/0001-6160(85)90214-7.

[49] F.J. Humphreys, M.G. Ardakani, Grain boundary migration and zener pinning in particle-containing copper crystals, Acta Mater. 44 (1996) 2717–2727. https://doi.org/10.1016/1359-6454(95)00421-1.

# CHAPTER 6: GENERAL DISCUSSION ON THE CONCLUSIONS, FUTURE WORK AND CONTRIBUTION TO ORIGINAL KNOWLEDGE

## 6.1 General Discussion on the Conclusions

### 6.1.1 Overall Conclusions

This study concluded that creep-resistant Al-Si-Mg-Cu cast alloys strengthened with nano-sized dispersoids for diesel engine applications are affected by creep micro-mechanisms that lead to creep deformation at the diesel engine operating conditions. These creep mechanisms for the four alloys studied in this PhD research are summarized in Table 6.1. It was noted that all three alloys that contain peritectic element additions exhibit local sub-grain formation during creep induced by strain accumulation at Si phase particles or coarse dispersoids. Elimination local strain accumulation at phase particle interfaces or designing resistance to sub-grain migration then becomes the key factors in creep resistance:

**Chromium, Zirconium and Manganese in Al-Si-Mg-Cu alloy**

1. It was demonstrated that Q'-precipitates of ageing have the main role to serve as nucleating sites for non-coherent α-dispersoids in the base alloy. However, in the Cr, Zr, Mn added alloy MG2-1, Q precipitates nucleate the coherent fine α-dispersoids. The optimization of the heat treatment to obtain fine nano-dispersoids is an important factor in improving creep resistance through Zener pinning.

2. Cr, Mo, Mn modified Al-Si-Cu alloy exhibits sub-grain formation but the migration of the boundaries exhibit Zener pinning from 5 nm dispersoids.

**Molybdenum and Manganese in Al-Si-Mg-Cu alloy**

1. The creep deformation mechanism was associated with dynamic recovery in alloys modified with Mo and Mn wherein solute diffusion and α-dispersoids influenced in the creep resistance.

2. At low level of Mn (0.15 wt.%), the dispersoids that form are coherent but shearable and are not very effective in pinning sub-grain boundaries. High level of Mn addition (0.5 wt.%) is effective in improving the creep resistance of the Al-7Si-0.3Mg-0.5Cu-0.3Mo alloy by limiting sub-grain formation or sub-grain boundary migration in two ways. (i) It locks Si in the dispersoids and makes Si less available for coarsening the Si particles thus lowering their effectiveness in initiating sub-grain formation during creep. (ii) Mn combines with Si to form highly thermally stable dispersoids at 300 °C; it forms fine coherent non-sherable $\alpha_{MG4\text{-}1}$-dispersoids that impede sub-grain migration.

3. It was demonstrated that an increase in the Mn level provide pinning effect in the grain boundary migration, dislocation motion and coarsening of Si particles due to the formation of

high volume fractions of thermally stable, coherent and non-shearable α-dispersoids in the 6 nm size range.

*Table 6.1. Creep parameters at 300 °C 28 MPa of aluminum alloys studied in this PhD research.*

| Alloy (Compositions (wt. %) | Min. Creep Rate ($s^{-1}$) | Activation Energy (kJ $mol^{-1}$) | | Creep Micro-mechanism | Creep Resistance Enhancers |
|---|---|---|---|---|---|
| | | Apparent | Calculated | | |
| (MG1) A356 + 0.5Cu | $4.5 \times 10^{-6}$ | 184 | 192 | Local climb over 50 nm non-coherent α-Al(Mn,Fe)Si | Q' precipitates that nucleate α-Al(Mn,Fe)Si |
| (MG2-1) A356 + 0.5Cu + 0.2Mn + 0.2Cr + 0.2Zr | $1.4 \times 10^{-6}$ | 234 | 230 | Sub-grain formation initiated locally at coarse (~500nm) α-Al(Mn,Fe)Si and sub-grain boundary migration | Zener pinning by 5 nm coherent α-Al(Mn,Cr,Fe)Si that are nucleated by the Q phase |
| (MG3-1) Al-7Si-0.3Mg-0.5Cu-0.15Mn-0.3Mo | $2.1 \times 10^{-6}$ | 202-203 | 203-208 | Sub-grain formation and boundary migration at Si phase particles | Slow diffusing Mn solute |
| (MG4-1) Al-7Si-0.3Mg-0.5Cu-0.3Mo-0.5Mn | $5.8 \times 10^{-7}$ | 249 | 251 | Sub-grain formation and boundary migration at Si phase particles (sub-grains finer than in MG3-1) | Limited Si phase coarsening --> reduced sub-grain formation, Zener pinning by 6 nm coherent α- $\alpha_{MG4\text{-}1}$-Al(Fe,Mo,Mn)Si |

## 6.1.2 Detailed Conclusions

1. 0.5%Mn and Mo additions to the Al-Mg-Si-Cu alloy (MG4-1) obtained the highest activation energy of 249 kJ $mol^{-1}$, and therefore the highest creep resistance, followed by MG2-1 alloy (Cr, Mn and Zr additions) with 234 kJ mol-1, MG3-1 alloy (0.15%Mn and Mo additions) with 203 kJ $mol^{-1}$ and MG1 (based alloy) with 184 kJ $mol^{-1}$.

2. The creep mechanism in MG4-1 and MG3-1 alloys were associated with dynamic recovery, but MG4-1 experienced limited silicon diffusion due to the stability of α-Al(Fe,Mn,Mo)Si

dispersoids and to the formation of coherent non-shearable nano-dispersoids pinning and limiting sub-grain migration. On the other hand, MG2-1 and MG1 alloys showed creep mechanisms related to recovery and Zener pinning of boundary migration and local climb over dispersoids, respectively.

3. Q-$Al_5Cu_2Mg_8Si_6$ phase served as precipitation center for the formation of nano-sized α-Al(Mn,Cr,Fe)Si and α-Al(Fe,Mo,Mn)Si dispersoids.

4. Particle size affected the coherency between particles and Al matrix, indicating that dispersoids with less than 6 nm were full coherency and low lattice strain.

5. Thermodynamic calculations demonstrated that creep resistance is mainly influenced by the amount and the thermal stability of the phases present after overaging process.

## 6.2 Future Work

Review of literature and research on the development of creep-resistant aluminum alloys intended for diesel engine applications shows that Diesel engines will continue to be employed in heavy vehicles in the long term due to the limitations of battery technology and charging infrastructure in the electric vehicles. Dispersion strengthening claims to be the most promising way to control creep deformation by the addition of transition metals due to the formation of thermally stable second phases uniformly distributed and in large volume fractions.

While this study contributes valuable insights into the effects of transition metals (Mn, Mo, Cr and Zr) on the creep resistance, future work concerns deeper analysis of particular mechanisms, new proposals, or simply curiosity. One avenue for future research is to investigate the role of heat

treatment to better understand the influence of Q' phase, Q phase and intermetallics on the amount of α-dispersoids. This would allow for a more comprehensive understanding of how the fully reached T7 condition may influence in the nucleation and precipitation of nano-sized dispersoids.

Similarity, study the effect of Mn, Cr, Zr and Mo on castability of the alloys in terms of melting temperature, alloying recovery rate, slag formation, melt temperature, etc. would help to improve and understand the manufacturing process.

Moreover, studying the behavior of dispersoids and solute atoms at the early, middle and final stages of the steady state creep rate by electron microscopy analysis could provide guidance on the evolution of the creep deformation mechanisms. Similarity, the investigation of the Al alloys at 325 °C and 350 °C by TEM microstructural observation would help to identify if the creep mechanisms at 300 °C are constant or change at higher temperatures.

Additionally, investigating the thermal stability of α-dispersoids from the reduction in their interfacial energy, and acting as diffusion barrier for atoms, caused by Mn solute segregation at α-Al(Fe,Mn,Mo)Si/Al matrix interface could help in the design of second-phase strengthening and ageing heat treatment.

Finally, the development of aluminum alloys using dataset, such as processing conditions, concentrations of alloying elements and internal-structural-features (type, volume fraction, shape and size), for machine learning-based algorithms could help to accelerate the designing of aluminum alloys satisfying the performance requirements (creep resistance at engine heat-up (300 °C and 22-30 MPa) and ensure an acceptable creep resistance.

## 6.3 Contribution to Original Knowledge

The contributions of this PhD thesis are three-fold:

1) The use of a new methodology based on theoretically calculated activation energy of creep mechanisms determined and revealed via in depth electron microscopy analyses that are compared to experimentally determined empirical apparent activation energy.

The apparent activation energy obtained experimentally has been associated with a direct method of estimating activation energies for creep based on the background on creep mechanisms and electron microscopy analyses.

In order to further develop and design creep resistant aluminum alloys, creep micro-mechanisms of these alloys need to be determined. For dispersoid strengthened alloys, recent work has adopted the concept of threshold stress that is experimentally determined; however, electron microscopy studies of the alloys have not discovered real features that can explain the empirical threshold stress. These studies cannot tell us the exact role of the microstructural features, nor can they identify which precipitates or dispersoids are interacting with dislocations or boundaries. Different models give different threshold stresses. A scientific method involving the correlation between the theoretical and the experimental activation energies via thermodynamic calculations, electron microscopy analysis and creep equations was used as strategy for determining creep mechanisms.

The new methodology developed and successfully employed in this PhD study relies on in-depth analysis of post creep samples with electron microscopy and then theoretically calculating the activation energies of creep mechanisms revealed by these analyses. The comparison of the

calculated activation energies with experimentally determined apparent activation energy for creep provides the final validation.

2) Determining the rate governing creep micro-mechanisms in Al-Si-Mg-Cu alloys modified by peritectic elements Cr, Zr, Mn and Mo so that new alloy design strategies can be formulated. It is noteworthy that the alloys that are modified with peritectic elements are prone to local recovery for which the alloys need to be strengthened with nano size (5-6 nm) dispersoids.

3) The understanding of the roles of peritectic elements Cr, Zr, Mn and Mo on the creep behavior of Al-Si-Mg-Cu alloys. Specifically the effectiveness of Cr and Zr even at low levels of Mn to prevent sub-grain boundary migration and the role of Mn at 0.5wt.% of creating highly thermally stable dispersoids for notable Zener pinning can be used for future alloy design.

# REFERENCES


[1] Statista Research Department, Transportation emissions worldwide - statistics & facts, (2024). https://www.statista.com/topics/7476/transportation-emissions-worldwide/.

[2] F. Feikus, Optimisation of Al-Si cast alloys for cylinder head applications, AFS Transactions 106 (1998) 1–21.

[3] M. Garat, G. Laslaz, Improved aluminium alloys for common rail diesel cylinder heads, AFS Transactions 115 (2007) 1–8.

[4] L. Heysler, F. Feikus, M. Otte, Alloy and casting process optimization for engine block application, AFS Transactions 050 (2001) 1–9.

[5] M. Pekguleryuz, E. Ozbakir, A.R. Farkoosh, Diesel engine: applications of aluminum alloys, in: G.E. Totten, M. Tiryakioglu, O. Kessler (Eds.), Encyclopedia of Aluminum and Its Alloys, CRC Press, Boca Raton, 2018: pp. 743–762.

[6] D. Li, K. Liu, X.-G. Chen, Evolution of microstructure and elevated-temperature properties during thermal exposure with transition elements (V, Zr and Mo) in Al–Si 356 type cast alloys, Mater. Trans. 64 (2023) 406–413. https://doi.org/10.2320/matertrans.MT-LA2022003.

[7] W. Qian, X. Kai, R. Tao, X. Gao, L. Huang, Y. Zhao, The corelation between creep resistance and microstructure in AA6111 alloy strengthened by synergistic Er, Zr addition, Mater. Sci. Eng. A. 870 (2023) 144867. https://doi.org/10.1016/j.msea.2023.144867.

[8] R.I. Arriaga-Benitez, M. Pekguleryuz, The synergistic effects of nano-sized α-Al(Mn,Cr,Fe)Si and Al–Si–Zr dispersoids on the creep behavior Al–Si–Mg–Cu (Mn, Cr, Zr) diesel engine alloy, Mater. Sci. Eng. A. 872 (2023) 144949. https://doi.org/10.1016/j.msea.2023.144949.

[9] R.I. Arriaga-Benitez, M. Pekguleryuz, Recent progress in creep-resistant aluminum alloys for diesel engine applications: a review, Materials 17 (2024) 3076. https://doi.org/10.3390/ma17133076.

[10] S.B. Heidelberg, Handbook of Diesel Engines, 2010. https://doi.org/10.1007/978-3-540-89083-6.

[11] M. Iguchi, Divergence and Convergence of Automobile Fuel Economy Regulations: A Comparative Analysis of EU, Japan and the US, Springer International Publishing, Cham, 2015. https://doi.org/10.1007/978-3-319-17500-3.

[12] A. König, L. Nicoletti, D. Schröder, S. Wolff, A. Waclaw, M. Lienkamp, An overview of parameter and cost for battery electric vehicles, World Electr. Veh. J. 12 (2021) 1–29. https://doi.org/10.3390/wevj12010021.

[13] K. Salonitis, M. Jolly, E. Pagone, M. Papanikolaou, Life-Cycle and Energy assessment of automotive component manufacturing: the dilemma between aluminum and cast iron, Energies 12 (2019) 2557. https://doi.org/10.3390/en12132557.

[14] M. Millikin, Opel to introduce new Euro 6 1.6 CDTI diesel in Geneva; 57 mpg US in the Zafira Tourer, Green Car Congress (2013).

https://www.greencarcongress.com/2013/02/opel-20130214.html.

[15] M. Millikin, GM introduces two new 1.7-Liter diesels for Opel, Green Car Congress (2007). https://www.greencarcongress.com/2007/04/gm_introduces_t_1.html#:~:text=GM%20is%20applying%20two%20new,fuel%20economy%20and%20low%20emissions.

[16] Wikipedia, Opel Rekord Series D, Wikipedia (2023). https://en.wikipedia.org/wiki/Opel_Rekord_Series_D.

[17] M. Phagare, Global aluminum cylinder head market report 2024, 2023.

[18] Verified market reports, Global Diesel Engine Block Market Research Report 2023-2030, 2023.

[19] Q. Xin, Durability and reliability in diesel engine system design, in: Q. Xin (Ed.), Diesel Engine System Design, 1st ed., Woodhead Publishing Limited, Cambridge, UK, 2011: pp. 143–145. https://doi.org/10.1533/9780857090836.

[20] F. Czerwinski, Thermal stability of aluminum alloys, Materials 13 (2020) 1–49. https://doi.org/10.3390/ma13153441.

[21] M.E. Kassner, Fundamentals of Creep in Metals and Alloys, Elsevier, Los Angeles, 2008.

[22] A.M. Brown, M.F. Ashby, On the power-law creep equation, Scripta Metallurgica 14 (1980) 1297–1302. https://doi.org/10.1016/0036-9748(80)90182-9.

[23] M.O. Pekguleryuz, A.A. Kaya, Creep resistant magnesium alloys for powertrain applications, Advanced Engineering Materials 5 (2003) 866–878. https://doi.org/10.1002/adem.200300403.

[24] R.E. Reed-Hill, Creep, D. Van Nostrand Company, New York, 1973.

[25] M. Celikin, The creep behavior of magnesium-manganese based alloys. PhD Thesis, McGill University, 2012.

[26] J.H. Gittus, Theoretical equation for steady-state dislocation creep effects of jog-drag and cell-formation, Philosophical Magazine 34 (1976) 401–411. https://doi.org/10.1080/14786437608222032.

[27] F.J. Humphreys, M.G. Ardakani, Grain boundary migration and zener pinning in particle-containing copper crystals, Acta Mater. 44 (1996) 2717–2727. https://doi.org/10.1016/1359-6454(95)00421-1.

[28] J. Lin, O.D. Sherby, Creep of oxide d strengthened materials (with special reference to T-D nichrome)., Res Mechanica: International Journal of Structural Mechanics and Materials Science 2 (1981) 251–293.

[29] K.R. Williams, B. Wilshire, On the stress- and temperature-dependenceof creep of nimonic 80a, Metal Science Journal 7 (1973) 176–179. https://doi.org/10.1179/030634573790445695.

[30] J.D. Parker, B. Wilshire, The effect of a dispersion of cobalt particles on high-temperature creep of copper, Metal Science 9 (1975) 248–252. https://doi.org/10.1179/030634575790445053.

[31] R.W. Lund, W.D. Nix, High temperature creep of Ni-20Cr-2ThO2 single crystals, Acta

Metallurgica 24 (1976) 469–481. https://doi.org/10.1016/0001-6160(76)90068-7.

[32] M.E. Kassner, Creep behavior of particle-strengthened alloys, in: M.E. Kassner (Ed.), Fundamentals of Creep in Metals and Alloys, Elsevier, Massachusetts, 2015: pp. 161–180.

[33] F. Carreño, G. González-Doncel, O.A. Ruano, High temperature deformation behavior of an Al-Fe-V-Si alloy, Materials Science and Engineering: A 164 (1993) 216–219. https://doi.org/10.1016/0921-5093(93)90665-2.

[34] S.P. Deshmukh, R.S. Mishra, K.L. Kendig, Creep behavior and threshold stress of an extruded Al-6Mg-2Sc-1Zr alloy, Materials Science and Engineering A 381 (2004) 381–385. https://doi.org/10.1016/j.msea.2004.05.025.

[35] K.E. Knipling, D.C. Dunand, D.N. Seidman, Criteria for developing castable, creep-resistant aluminum-based alloys - A review, IJMR. 97 (2006) 246–265. https://doi.org/10.1515/ijmr-2006-0042.

[36] G.E. Totten, ed., Heat Treating of Aluminum and Its Alloys, in: Heat Treating of Nonferrous Alloys, ASM International, 2016. https://doi.org/10.31399/asm.hb.v04e.9781627081696.

[37] R.N. Lumley, Heat Treatment of Aluminum Alloys, in: R.B. Hetnarski (Ed.), Encyclopedia of Thermal Stresses, Springer Netherlands, Dordrecht, 2014: pp. 2190–2203. https://doi.org/10.1007/978-94-007-2739-7_431.

[38] D.S. MacKenzie, Metallurgy of Heat Treatable Aluminum Alloys, in: K. Anderson, J. Weritz, J.G. Kaufman (Eds.), Aluminum Science and Technology, ASM International, 2018: pp. 411–437. https://doi.org/10.31399/asm.hb.v02a.a0006509.

[39] B. Milkereit, M.J. Starink, P.A. Rometsch, C. Schick, O. Kessler, Review of the Quench Sensitivity of Aluminium Alloys: Analysis of the Kinetics and Nature of Quench-Induced Precipitation, Materials 12 (2019) 4083. https://doi.org/10.3390/ma12244083.

[40] H. Clemens, S. Mayer, C. Scheu, Microstructure and Properties of Engineering Materials, in: P. Staron, A. Schreyer, H. Clemens, S. Mayer (Eds.), Neutrons and Synchrotron Radiation in Engineering Materials Science, 1st ed., Wiley, 2017: pp. 1–20. https://doi.org/10.1002/9783527684489.ch1.

[41] T. Gladman, On the theory of the effect of precipitate particles on grain growth in metals, Proc. R. Soc. Lond. A 294 (1966) 298–309. https://doi.org/10.1098/rspa.1966.0208.

[42] V.I. Razumovskiy, Yu.Kh. Vekilov, I.M. Razumovskii, A.V. Ruban, V.N. Butrim, V.N. Mironenko, Effect of alloying elements and impurities on interface properties in aluminum alloys, Phys. Solid State 53 (2011) 2189–2193. https://doi.org/10.1134/S1063783411110266.

[43] Q. Lu, J. Wang, H. Li, S. Jin, G. Sha, J. Lu, L. Wang, B. Jin, X. Lan, L. Li, K. Li, Y. Du, Synergy of multiple precipitate/matrix interface structures for a heat resistant high-strength Al alloy, Nat Commun 14 (2023) 2959. https://doi.org/10.1038/s41467-023-38730-z.

[44] G.P.M. Leyson, L.G. Hector, W.A. Curtin, Solute strengthening from first principles and application to aluminum alloys, Acta Materialia 60 (2012) 3873–3884. https://doi.org/10.1016/j.actamat.2012.03.037.